

PHOTOIONIZATION MODELS  
OF THE DIFFUSE IONIZED GAS  
IN GALACTIC HALOS



DISSERTATION

zur

Erlangung des Grades

“Doktor der Naturwissenschaften”

der Fakultät für Physik und Astronomie

an der Ruhr-Universität Bochum

von

Torsten August Wilhelm Heinrich Elwert

Bochum, im September 2003

Erster Gutachter: Prof. Dr. Ralf-Jürgen Dettmar (Institut für Astronomie, AIRUB)  
Zweiter Gutachter: HD Dr. Susanne Hüttemeister (Institut für Astronomie, AIRUB)

Die Magier kamen, doch keiner verstand,  
Zu deuten die Flammenschrift an der Wand.  
*Heinrich Heine*



# Contents

<b>1</b>	<b>Introduction</b>	<b>1</b>
1.1	The Interstellar Medium . . . . .	1
1.1.1	Constituents of the multiphase ISM . . . . .	3
1.1.2	Star–gas–cycle . . . . .	4
1.2	Models of the ISM . . . . .	5
<b>2</b>	<b>Diffuse Ionized Gas</b>	<b>9</b>
2.1	Basic characteristics . . . . .	9
2.2	Power requirement . . . . .	10
2.3	Optical spectral features . . . . .	14
2.4	Database . . . . .	16
2.4.1	Scale height $h = 0.6$ kpc . . . . .	16
2.4.2	Scale height $h = 1$ kpc . . . . .	18
2.4.3	Scale height $h = 2.5$ kpc . . . . .	20
<b>3</b>	<b>CLOUDY</b>	<b>23</b>
3.1	Introduction to CLOUDY . . . . .	23
3.2	Photoionization models with CLOUDY . . . . .	24
3.3	Heating–cooling balance . . . . .	25
3.4	Parameters . . . . .	29
<b>4</b>	<b>Applications of CLOUDY</b>	<b>35</b>
4.1	General remarks . . . . .	35
4.2	Handling data and models . . . . .	36
4.3	Models and data . . . . .	37
4.3.1	Trends in the data . . . . .	37
4.3.2	Trends in the model predictions . . . . .	37
4.3.3	Spectral energy distribution of the input spectra . . . . .	37
4.4	Stellar input spectra . . . . .	40
4.4.1	$h = 0.6$ kpc: NGC 4302, UGC 10288 . . . . .	40
4.4.2	$h = 1$ kpc: NGC 1963, NGC 3044, NGC 4634, NGC 4631, NGC 3079 . . . . .	42
4.4.3	$h = 1$ kpc: Perseus Arm . . . . .	42
4.4.4	$h = 2.5$ kpc: NGC 891 . . . . .	45

4.5	Stellar temperatures . . . . .	45
4.6	Stellar remnant sources . . . . .	49
4.7	Extra heating source . . . . .	51
4.8	Metallicity indicator? . . . . .	54
4.9	Column densities . . . . .	60
<b>5</b>	<b>Results and discussion</b>	<b>63</b>
5.1	Accuracy of the models . . . . .	63
5.1.1	Geometry . . . . .	63
5.1.2	Radiative transfer . . . . .	63
5.1.3	Atomic database . . . . .	64
5.2	Previous models . . . . .	66
5.3	Conclusions . . . . .	70
5.3.1	Summary . . . . .	70
5.3.2	Ionizing photon flux . . . . .	74
5.3.3	Heating–cooling balance . . . . .	75
5.3.4	Emission lines and SED . . . . .	77
5.3.5	Column densities . . . . .	78
5.3.6	Quality of the models . . . . .	79
5.4	Outlook . . . . .	79
5.4.1	General statements . . . . .	79
5.4.2	Considering the multiphase nature of the ISM . . . . .	83
	<b>Bibliography</b>	<b>85</b>
	<b>List of Figures</b>	<b>91</b>
	<b>List of Tables</b>	<b>93</b>

# Chapter 1

## Introduction

### 1.1 The Interstellar Medium

A very vital topic that is discussed in astronomy (Galactic and extragalactic) is the Interstellar Medium (ISM) as was e.g. recently demonstrated during the conference “How does the Galaxy work?” (23. – 27. June 2003, Granada, Spain). At first sight this seems a little astonishing as the ISM contributes only  $\sim 5-20\%$  to the dynamical mass of a galaxy (Dettmar 1992). However this relatively small fraction is playing a very essential role concerning the history and evolution of the galaxies as viewed as an ecosystem. The ISM in the halo can even be regarded as a galactic atmosphere.

The best approach is to first disentangle the various constituents of the ISM: photons, particles, and fields (see Figure 1.1). The next step is the investigation of the influence and interplay of the different ingredients among each other and the formation of certain phases with distinct physical characteristics which leads to a global picture of a multiphase ISM. This multiphase ISM is fundamental to understand the star–gas–cycle (see Figure 1.2) which links the stars with the gas out of which they are born and with which they interact in numerous ways. The stars in turn determine the further development of the galaxies with time. This leads the way to the evolution of models trying to understand what is going on in and with the ISM and which have to be tested against observations.

The present thesis is dealing with one specific phase of the ISM, the Diffuse Ionized Gas (DIG) and the questions concerning its appearance and physical parameters. Before proceeding with this phase in detail in chapter 2, the global picture together with the according models (see section 1.2) will be introduced.

The systems examined are the late–type (i.e. gas–rich) [grand–design] spiral galaxies, which consist of  $\sim 10^{11}$  stars with gas between them (see e.g. Tayler 1993). The stellar component of a spiral galaxy is build out of three fundamental blocks: galactic disk, bulge, and stellar halo, also called ‘baryon halo’ or ‘spherical stellar component’ (see Figure 1.3). The galactic disk is characterized by a thickness of about  $200 \text{ pc}^1$ , occupied by stars, gas,

---

<sup>1</sup>1 pc =  $3.086 \times 10^{16}$  m

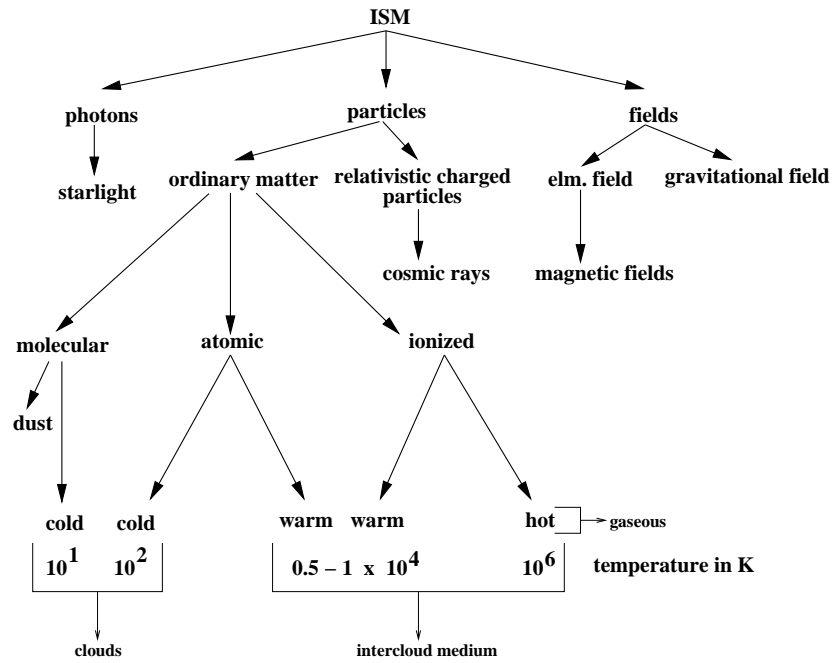


Figure 1.1: *ISM constituents*

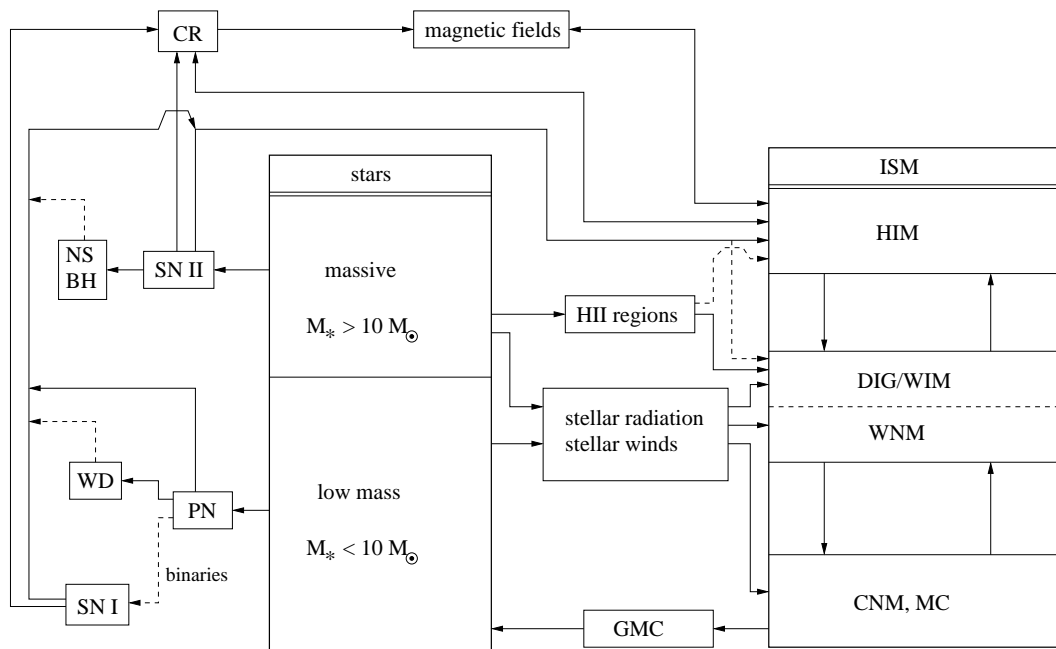


Figure 1.2: *Star-gas-cycle, the abbreviations are explained in the text (subsection 1.1.2)*



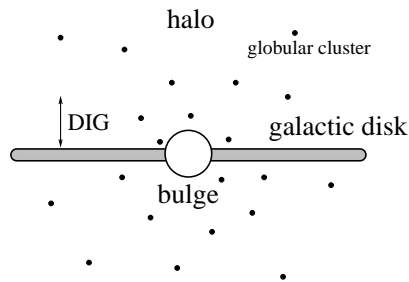


Figure 1.3: *Sketch of the edge-on view of a spiral galaxy, the halo is indicated*

and dust, and a diameter of 30 kpc. The bulge is a sphere of stars situated in the middle of the galaxies, its diameter reaches values in the order of 1.5 kpc. The center of the bulge and the spherical stellar halo coincide. The halo is traced particularly by globular clusters<sup>2</sup> which are detected at distances up to almost 40 kpc (Sakamoto et al. 2003) from the disk. The DIG under consideration is situated above the disk, being a part of the halo (see section 2.1).

Beside measurements in our own Galaxy only systems of edge-on galaxies will be considered, because only in these all components are clearly separated. The angle between the line of sight and the normal vector of the galactic disk is  $90^\circ$  in the case of edge-on galaxies. The spiral arm pattern is not visible but all fundamental galactic components are clearly separated allowing to study the ISM above the disk in detail; this is the reason for the choice of the edge-on systems. In contrast, the face-on view with an observation angle of  $0^\circ$  allows a direct view on the spiral arms. The radiation of the different ISM phases is superimposed in the observed spectra and it is impossible to disentangle it completely.

### 1.1.1 Constituents of the multiphase ISM

The ISM is located throughout all components of a galaxy. It consists of photons, particles, and fields as schematically sketched in Figure 1.1. The particles are influenced on large scales by the gravitation, rotation of the galaxy, and magnetic fields. They can be subdivided into 'ordinary matter' and relativistic charged particles, the Cosmic Rays (CR). The atomic/chemical state of the ordinary matter (molecular, atomic, and ionized) is triggering a further division. It is noteworthy that the diverse gas components, CR, magnetic fields, and starlight all have very roughly the same energy density of about  $1 \text{ eV cm}^{-3}$ . By number of nuclei, about 90% of the interstellar matter is hydrogen (75% by mass), 10% helium, all elements heavier than helium contribute 0.1% of the interstellar nuclei (or  $\sim 2\%$  by mass). Roughly half of the heavier elements are in the gas phase the rest of them (especially Si, Ca, Fe) are depleted from it and locked up in small dust grains (tiny solid particles) mixed in with the gas.

The constituents are forming different phases with characteristic physical properties regarding e.g. the ionization structure, temperature, and pressure. There are two main phases of

<sup>2</sup>spherical systems with  $\sim 10^5 - 10^6$  stars

Table 1.1: *ISM phases and their properties*

ISM phase	filling factor $f$	midplane density in $\text{cm}^{-3}$	scale height in pc	temperature in K	pressure in $\text{cm}^{-3} \text{K}$
MC	0.003	100	60	20	20
CNM	0.02	20	135	150	5000
WNM	0.3	0.5	300	5000	200
DIG	0.2	0.2	1000	$10^4$	3400
HIM	0.5	0.006	3000	$10^6$	$2 \times 10^4$

the gas: clouds and the intercloud medium. The intercloud medium is further subdivided into more phases, Table 1.1 (see e.g. Heiles 2001, Dettmar 1992) gives an overview of the knowledge of the ISM phases up to date and their principal characteristics. The phases are ordered with decreasing density<sup>3</sup>, starting with the Molecular Clouds (MC), continuing the Cold Neutral Medium (CNM), the Warm Neutral Medium (WNM), the DIG and ending with the Hot Ionized Medium (HIM). This sequence has to be reversed if one is considering temperatures. All density distributions are exponential with the indicated values for the scale heights. The specific pressures  $(\frac{P}{k})^4$  do not show the clear sequence as given by the density or temperature. In order to sustain such a variety of components there must exist a global equilibrium between them, so that each of them can maintain its temperature, pressure, and ionization structure. The MC and the CNM are forming the clouds, which account for about half the mass and 2% of the interstellar volume. The clouds consist of about half of the neutral atomic hydrogen, all of the molecular hydrogen, and all other molecules. The WNM, DIG, and HIM are forming the gaseous intercloud medium. This arrangement is also indicated in Figure 1.1. The approximate (volume) filling factor is also given in Table 1.1, it is a concept to take into account the clumpiness of the ISM in an effective way. The fraction stated for each phase means that only this part of the volume is filled with the specific phase. A good and recent review over the “Diffuse Universe”, i.e. physical processes relevant for the ISM and the observational picture, is given by Dopita & Sutherland (2003).

### 1.1.2 Star–gas–cycle

After the nature of the multiphase ISM is revealed the discussion of the star–gas–cycle (see Figure 1.2) is next in order to understand the importance of the ISM (the “blood”) of the galaxies. As the stellar density is highest in the midplane of a galaxy the star–gas–cycle will be most efficient in these regions with additional processes occurring e.g. in the halo. The stars form out of Giant Molecular Clouds (GMC) with masses high enough so that

<sup>3</sup>for this and all other densities specified: the density is a number density with unit: particles  $\text{cm}^{-3}$

<sup>4</sup> $k$  is the Boltzmann constant

self-gravitation can set in. GMC have most likely formed out of colliding MC and CNM. The resulting stars are categorized into two groups: high and low mass stars with the dividing limit of 10 solar masses ( $M_{\odot}$ ).

High mass stars provide a much more active feedback to the ISM through a much harder stellar radiation and stellar winds than the low mass stars. As a consequence the CNM is heated and transformed into WNM and with increasing UV-photon flux into DIG, also called Warm Ionized Medium (WIM). Most stars can be attributed to seven main classes of the Harvard classification scheme. The hottest stars of these, which are of significance for this thesis, are the O and early B stars. They are high mass stars with effective temperatures ranging from  $\sim 30,000$  K to more than 50,000 K. Depending on the stellar type more than half of the hot stars are embedded into HII regions, that are gas clouds surrounding the stars. These clouds get ionized through the hydrogen ionizing photon flux of the central star where the extension of the HII region is mainly dependent on the effective stellar temperature and the density of the ambient medium. The boundary of the HII region is well defined and called the Strömgren Sphere. Apart from the classical ionization bounded case where all photons are absorbed in the cloud and the matter bounded case where the edge of the Strömgren Sphere is the boundary of the gas cloud, there is an intermediate state where some photons 'leak' out of the corresponding HII region.

The explosive events accompanying the 'death' of stars like Planetary Nebulae (PN), Supernovae (SN) and the successors (White Dwarfs (WD), Neutron Stars (NS), and Black Holes (BH)), can heat up further the medium to become the HIM. CR are accelerated in the SN Remnants (SNR). For nearly all processes magnetic fields provide another energy source and also an ordering effect as they are able to structure the components of the ISM on large scales especially CR. The difference between a SN type I and SN type II is mainly in the freed processed material. During the life and death of a massive star all elements up to iron are produced by fusion and the SN II events (core collapse of a massive star) itself produces elements heavier than iron. The low mass stars which produce PN, WD, and if they are in a binary system and the conditions are right also SN I (where a WD is disrupted), do not enrich the ambient medium as much as high mass stars and SN II.

## 1.2 Models of the ISM

The 'picture' we have from the ISM is mainly influenced and altered by the observations. Different models are helping in investigation and learning more about this very vital phase and building block in galactic evolution. The advance in observations is very closely linked with the evolution of the models as with time more phases were discovered and more detailed information became available.

The interstellar matter in form of gas (atoms, molecules, ions, and electrons) and dust manifests itself primarily through obscuration, reddening, and polarization of starlight, through the formation of absorption lines in stellar spectra, and through various emission mechanisms (both over a continuum and at specific wavelengths). Based on this fact the first quasi-static theory of a multiphase ISM was developed by Field, Goldsmith, and

Habing (1969) (FGH). This model deals with the two phases known to this time, the CNM and the WNM which serves as the pervasive ambient medium for the HI clouds. The heating of the phases was believed to be provided by CR. The authors stated also the possible existence of another stable phase at a temperature of  $\sim 10^6$  K. However, it was not until observations of X-rays were available and until Cox & Smith (1974) realized the importance of SN theoretically, that this was seriously considered.

A slightly different perception is the galactic fountain model (Shapiro & Field 1976) which was the first model to include disk-halo interactions and therefore viewing the whole galaxy as an ecosystem. The material participates in a cycle from the disk into the halo and back. The HIM produced in the plane reaches distances of 1 kpc where the gas finally radiatively cools, forms clouds, and falls back to the plane if the outflow velocity is smaller than the escape velocity. The whole disk of the galaxy participates in this matter and energy flow which is therefore a global phenomenon. The galactic fountain model is thereby the first of the dynamical models which focus on a global picture and dynamics.

McKee & Ostriker (1977) introduced a thorough theoretical model of the ISM (MO). It is a three-phase model where the ISM is dominated by SN. The SN produce the HIM which was discovered due to the extended diffuse X-ray emission. The filling factor of the HIM in this model is close to unity, i.e. nearly the whole volume constitutes of this phase. The HIM fills the interior of SN remnants and powers their blast waves, which sweep up the gas (and magnetic field) inside the bubble and pile it into shells forming the outer boundaries of the remnants. Soon this shocked gas starts to cool and recombine rapidly, forming the CNM. Soft X-rays produced by immediately adjacent HIM penetrate the outside of CNM clouds, heating the gas to form the partially ionized WNM, with increasing ionization degree the WNM transforms into the WIM/DIG. In summary there are four phases (CNM, WNM, WIM/DIG, and HIM) present, however there are still only two fundamental ones: the CNM and the HIM. The WNM and WIM/DIG are only envelopes of the other two (see Figure 1.4) and act therefore merely as the interfaces between the basic phases. At the same time stable thermal pressure equilibrium between the neighboring phases is a fundamental assumption of the MO model. It has still some shortcomings, e.g. the influence of magnetic fields and CR are neglected. However magnetic pressure seems to be high enough that it plays an important role in equilibrating the pressure balance. Moreover it has significant effects on ionized plasmas and can create ordered structures over large distances, therefore linking the different galactic components and gas phases with each other. The MO model remains nevertheless an important framework for other models which alter some aspects. It is remarkable that the galactic fountain model emphasized the importance of SN and a hot medium one year before the MO model.

The chimney model (Ikeuchi 1988 and Norman & Ikeuchi 1989) builds on both the fountain model and the MO model. In this model massive OB associations<sup>5</sup> first blow cavities in the ISM, SN explosions of the associations can then later expand into these cavities and form superbubbles. As the bubbles get less resistance in expanding vertical to the disk this results in chimney like structures, see Figure 1.5. These structures are then able to create

---

<sup>5</sup>groups of some 30 O and B stars (Harwit 1998)

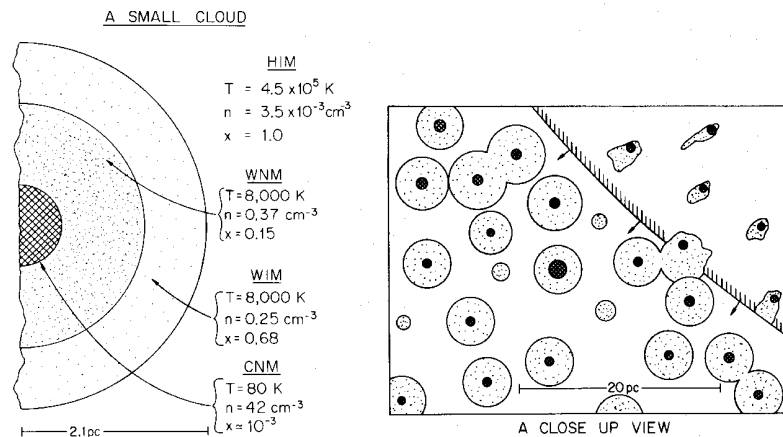


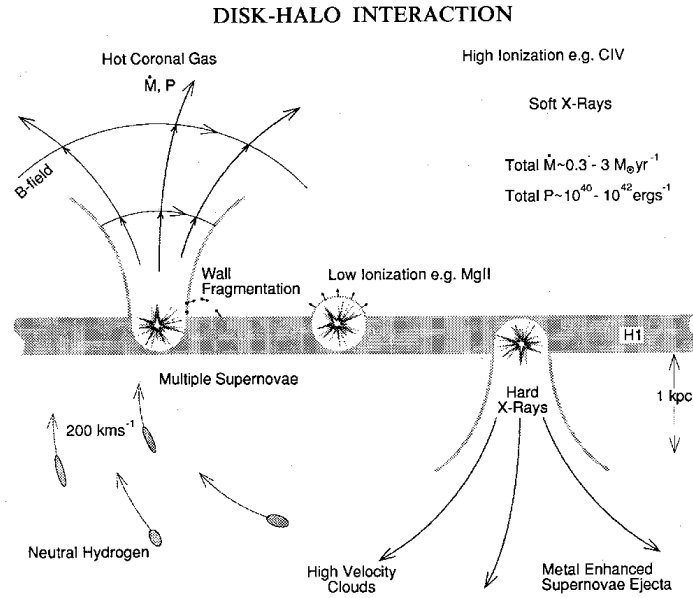
Figure 1.4: *Picture of the ISM as proposed by the MO model (McKee & Ostriker 1977), the right sketch shows the impact of a SN generated shock wave coming from the upper right corner on the small ISM clouds: they evaporate and only their cores survive*

and maintain a gaseous halo. The matter and energy flow is thereby concentrated in the chimneys. The basic difference between chimneys and fountains is that chimneys are more localized and not as pervasive as fountain outflows. The volume filling factor of the HIM is therefore smaller in the chimney model than in the fountain model and also in the MO model. The chimney model is roughly consistent with the current observational evidence although some points are still uncertain or not included. The power requirement of the DIG, the role of CR and magnetic fields are sources of controversial discussions. On an energy scale the chimney model is an intermediate level between a quiescent (two-phase) ISM and a three-phase ISM, in which the HIM dominates.

The general picture obtained from observations of the ISM is still more complex than the models up to now. There are many open questions that have to be answered. Heat conduction, magnetic fields, and CR are mostly neglected. Every model has to face the influence of these sources in order to estimate the quality of the model and give further improvements. The importance of magnetic fields is most likely to be underestimated as measurements of the magnetic fields in spiral galaxies give magnetic field strengths in the order of  $5-10 \mu\text{G}$ <sup>6</sup> (for a sample of 20 galaxies see Beck et al. 2002) which is considerably more than previously assumed. The magnetic fields furthermore link the different gas phases with each other, and also with the CR, so that the individual components cannot act independently.

Table 1.2 shows a summary of different models of the ISM concentrating on the disk-halo interaction; it is meant as an overview and is not complete. All these models can be grouped according to the energy they put into the ISM. The superwind and superbubble outbreak scenario are most energetic, followed by the galactic fountain and the chimney model. Superbubbles and supershells are created by multiple correlated SN explosions most probable occurring in OB associations.

<sup>6</sup>1 G =  $10^{-4}$  T

Figure 1.5: *Picture of ISM as proposed by the chimney model (Norman & Ikeuchi 1989)*Table 1.2: *ISM models emphasizing the disk-halo interaction*

model	references
chimneys	Norman & Ikeuchi 1989, Tenorio-Tagle & Munoz-Tunon 1998
galactic fountain	Shapiro & Field 1976, de Avillez 2000
superbubble outbreak scenario	Mac Low & McCray 1988, Mac Low & Ferrara 1999
superwinds	Heckman et al. 1990

# Chapter 2

## Diffuse Ionized Gas

### 2.1 Basic characteristics

The phase of the ISM which will be discussed further in detail is the DIG. This phase has 'developed' different notations over the time, the most common ones are WIM for our Milky Way and DIG for external galaxies. This thesis uses the last notation for consistency. This plasma is characterized by an average temperature of  $\sim 10^4$  K, an average midplane density of  $\sim 10^{-1} \text{ cm}^{-3}$ , and an exponential density distribution with scale heights ranging from 0.6 kpc to 2.5 kpc depending on the individual galaxy. The filling factor is  $\sim 10 - 20\%$ , i.e. only 1/10 to 1/5 of the volume is filled with this diffuse phase. There are hints that the filling factor is not constant but grows with increasing vertical  $|z|$  height (Mitra et al. 2003, Haffner et al. 1999, Reynolds et al. 1999, Kulkarni & Heiles 1987).

Of particular interest is the DIG in the halo, sometimes also called extra planar DIG (eDIG) which can best be observed in late-type edge-on spiral galaxies. The edge-on view has the advantage that one can observe faint emission above the midplane of galaxies clearly separated from the emission originating in the midplane. The disposition of DIG and eDIG is motivated from the observers point of view, physically there is no distinction between them and the models treat them accordingly the same.

It seems that the DIG is associated with star formation in the disk (Rossa & Dettmar 2003a, Dahlem et al. 2001, Rossa & Dettmar 2000, Dahlem 1997) as all nearby edge-on starburst galaxies exhibit this phase (Lehnert & Heckman 1995). The eDIG-layer is best observed in the hydrogen recombination line  $\text{H}\alpha$  (Balmer line, transition from principal level 3 to 2) as 30 - 50% of the  $\text{H}\alpha$  luminosity (Hoopes et al. 1996, Ferguson et al. 1996) of a galaxy originate in the DIG independently of the Hubble-type. This is clearly an indication that the basic mechanisms to power the DIG are similar for all galaxies. Photoionization is a very viable candidate for such a process. The remaining  $\text{H}\alpha$ -flux is produced in HII regions surrounding young, hot stars.

It is still not clear what fraction of the 'normal' spiral galaxies have eDIG-layers, it seems that up to 40% of such galaxies show this phase (Rossa & Dettmar 2003a, Dahlem et al. 2001). Rossa & Dettmar (2003a and 2000) show evidence that the existence of an eDIG-

layer is associated with star formation in the underlying disk of normal galaxies, too.

Figure 2.1 shows the morphology of the  $H\alpha$  luminosity in our own Galaxy as was observed by the WHAM (Wisconsin  $H\alpha$  mapper) survey. The observed intensity of the  $H\alpha$  line was integrated for this image over the velocity interval  $-80 \text{ km s}^{-1}$  to  $+80 \text{ km s}^{-1}$ . The region of the Galactic equator ( $b = 0^\circ$ ) is populated by numerous HII regions, between them and above the midplane a diffuse emission is present, sometimes visible as shell-like structures and filaments. This emission in the Milky Way is also called the 'Reynolds-layer'. There is e.g. an outstanding filament in the region between Galactic longitude  $l = 210^\circ - 240^\circ$  and Galactic latitude  $b = 15^\circ - 50^\circ$ . The influence of the projection of the three dimensional objects to a two dimensional plane is an important question, so it is a priori not clear if e.g. the shell structures are real or projections of sheet-like structures. Two very clear O star HII regions are visible around  $l = 0^\circ$  and  $b = 15^\circ - 30^\circ$ . Another HII region at higher Galactic latitude is visible as the bright spot near  $l = 300^\circ - 330^\circ$  and  $b = 45^\circ - 60^\circ$  and is produced by a B star.

In order to study how common such a DIG phase is for galaxies besides the Milky Way other edge-on galaxies have been investigated, too. Figure 2.2 shows the inner part of NGC 55 measured in  $H\alpha$  as a good and impressive example of a similar DIG morphology as observed in the Milky Way. NGC 55 is located at a distance of  $1.82 \text{ Mpc}^1$ . The midplane of this galaxy is populated by many bright HII regions with diffuse  $H\alpha$  emission between them. There are also some very prominent filaments and shell structures visible suggesting a very turbulent state of the DIG. Additionally NGC 55 shows evidence of star formation in the halo (Tüllmann et al. 2003).

The  $H\alpha + [\text{NII}]$  image of NGC 3044 (see Figure 2.3) exhibits in contrast a quiescent DIG-layer where no turbulent structures are visible, only a very smooth varying brightness envelopes the midplane. Here HII regions are represented by black dots, the eDIG-layer is thickest above the central part of NGC 3044 where the concentration of HII regions is highest, too. This fact also suggests a connection between star formation and appearance of a DIG-layer. The distance to NGC 3044 amounts to  $18.21 \text{ Mpc}$ .

## 2.2 Power requirement

Since the discovery of the DIG and its inclusion into ISM-models this phase rises the central question of how it is ionized and heated (see e.g. Collins & Rand 2001, Dahlem et al. 2001, Mathis 2000, Haffner et al. 1999, Dahlem 1997, Dettmar 1992). It is up to now a matter of discussion which source is powerful enough to sustain the DIG-layer continuously. Without such a source the gas would cool down, the ions would recombine and consequently the observed emission lines would vanish. The typical recombination time of hydrogen is under these conditions approximately  $10^6 \text{ a}$ . The DIG-layer needs thus at least every million year 'fresh' UV-photons to maintain the recombination radiation of

<sup>1</sup>with a Hubble constant of  $H_0 = 71 \text{ km s}^{-1} \text{ Mpc}^{-1}$



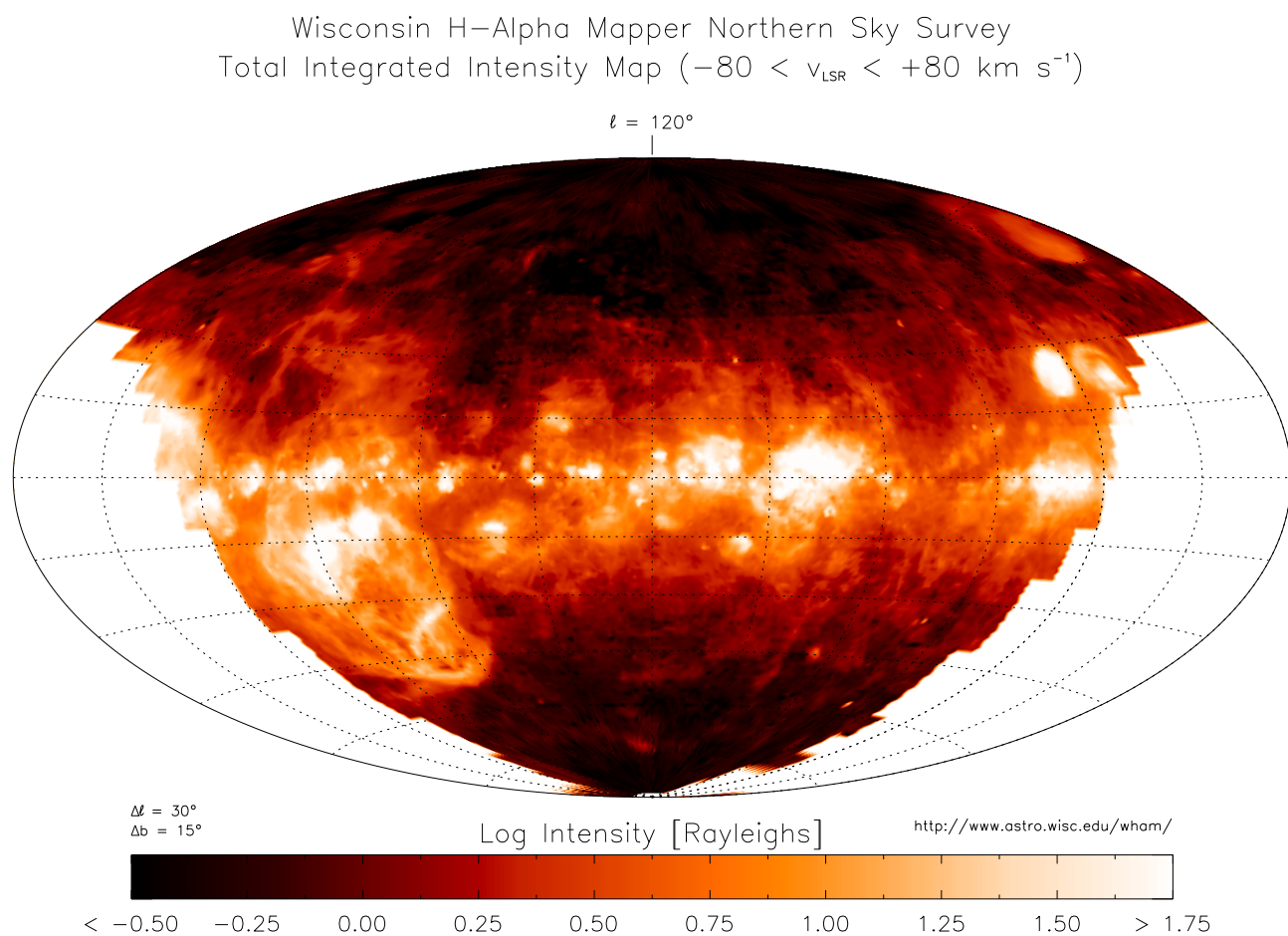


Figure 2.1: *Morphology of the DIG in the Milky Way, WHAM collaboration (e.g. Haffner et al. 2001, Haffner et al. 1999)*

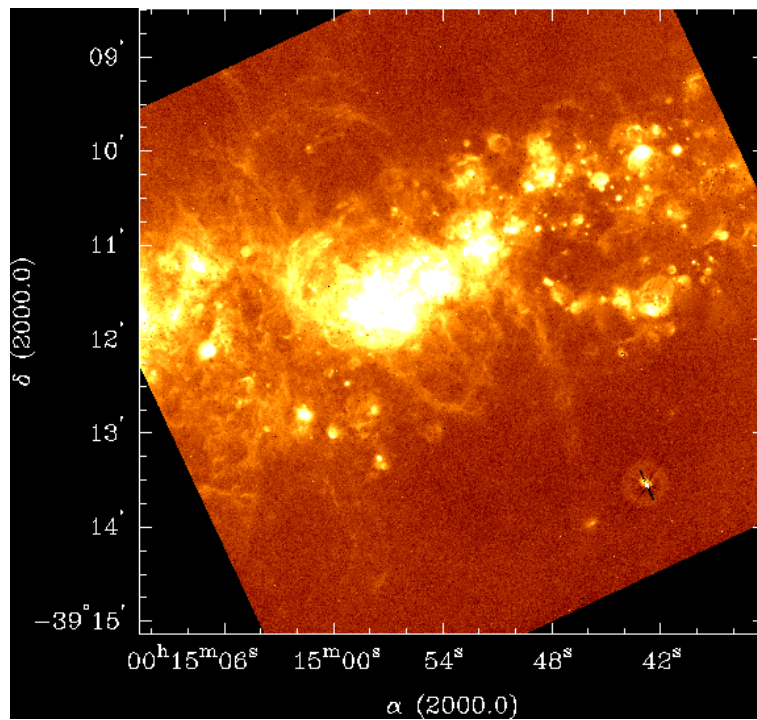


Figure 2.2: *Morphology of the DIG in the central part of NGC 55, Tüllmann et al. (2003)*

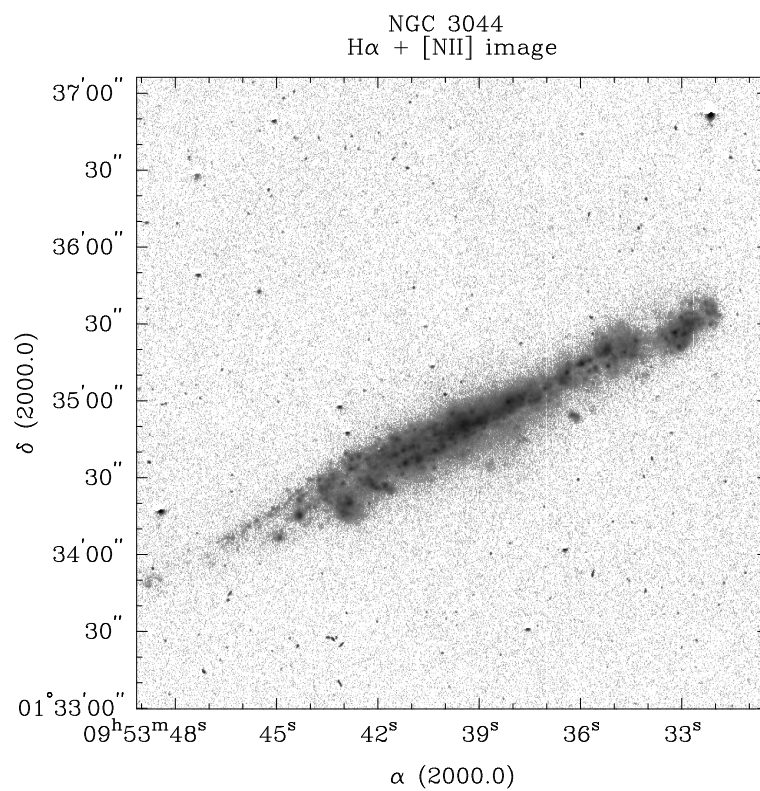


Figure 2.3: *Morphology of the DIG in NGC 3044, Rossa (2001)*

hydrogen.

Another question that has to be addressed is how the ionizing photons are able to reach the large distances from the midplane despite the neutral hydrogen layer. This so called 'Lockman-layer' with a scale height of  $\sim 500$  pc (Lockman 1984, Lockman et al. 1986) is effectively blocking the ionizing photons if it would have a uniform density. This problem will not be further discussed in this work, however imagining the morphology of the neutral ISM layer like a 'Swiss cheese' creates an impression how the ionizing photons are able to reach the halo by passing through numerous holes in this layer. The chimneys are favorable traveling passages for the ionizing photons. Likely candidates are the HI 'worms' detected by Heiles (1984), a widespread survey of HI 'worms' was made by Koo et al. (1992) and they detected approximately 100 of these structures. Another evidence for the existence of the holes is given by the observations of Welsh et al. (1999). They detected 20 extragalactic sources (AGNs<sup>2</sup>) towards higher galactic latitudes using the EUVE satellite<sup>3</sup> thereby proving that the ISM exhibits holes, as only with very low column densities of HI these sources can be detected. The number of detected chimneys seems however not enough for the ionization of the whole halo, there are only  $\sim 100$  observed, but  $\sim 1000$  are needed (Norman & Ikeuchi 1989). The exact role of the chimneys is thus still a matter of debate. There is also evidence that the Lockman-layer consists of essentially discrete clouds, whose individual motions support them against the Galactic gravitational potential (Lockman & Gehman 1991).

Reynolds (1990) estimated the power needed to maintain the DIG to be larger than  $1.0 \times 10^{-4}$  erg cm<sup>-2</sup> s<sup>-1</sup>, this equals an ionization rate of  $\Phi_{\text{DIG}} \approx 5 \times 10^6$  ionizations cm<sup>-2</sup> s<sup>-1</sup>. Considering known sources for UV-photons one needs about 16% of the radiation from all OB stars or 100% of the total energy input of all SN (Reynolds 1993, Abbott 1982). This means that the HII regions surrounding O stars and OB associations must be leaky so that  $\sim 1/6$  of the ionizing photons can escape. According to the life times of O stars with an effective stellar temperature of 40,000 K ( $3 \times 10^6$  a) the recombination time of hydrogen in the DIG is less ( $10^6$  a) and hence O stars are able to form a steady source under the condition that there is a continuous supply of these stars. Other possible sources fall short in providing enough ionizing power, these sources include white dwarfs (Panagia & Terzian 1984), X-rays (McCammon et al. 1983), and the EUV background (Vogel et al. 1995, Donahue et al. 1995). According to Bregman & Harrington (1986) the strength of all these sources amounts to  $\sim 10\%$  to that of the OB star radiation only. This means that the efficiency with which these sources can transform their energy into ionizing and heating the DIG must be nearly 100% in order to play a dominate role in powering this phase of the ISM which seems rather unlikely. However these sources may play a role as 'extra heating' sources which can be a significant part of the total heating rate for increasing distances from the midplane as will be discussed in section 4.7.

Other proposals for ionizing/heating sources include photoelectric grain heating (see e.g. Reynolds & Cox 1992), dissipation of turbulence (e.g. Minter & Spangler 1997) including

---

<sup>2</sup>AGN = Active Galactic Nuclei

<sup>3</sup>EUVE satellite = Extreme UltraViolet (EUV) Explorer satellite

shocks (e.g. Slavin et al. 2000), magnetic reconnection (e.g. Birk et al. 1998), or heating by CR e.g. through linear Landau–damping (e.g. Lerche & Schlickeiser 2001). Low energy CR<sup>4</sup> could also play a significant role. The amount of heating proposed for this sources can account for or even exceed the need for the DIG. The mechanisms and balancing processes have therefore further to be analyzed in more detail and with great care to answer the pressing question which processes are really of importance for the concerning plasma. These sources have also to answer the question how they can distribute their released energy very homogeneously throughout the halo when in the example of shocks there is only a very localized region producing the heat. Moreover it is an open question how to distinguish unambiguously between different heating sources given the available and future observations.

The hydrogen ionizing photon flux of OB stars is therefore up to now the most likely source to be responsible for the maintenance of the DIG, as was also investigated by Dove et al. (2000) or Miller & Cox (1993). The DIG is emitting a characteristic spectrum that is dependent on the ionizing source and the internal physical conditions.

In order to test whether or not hot stars are the main source in powering the DIG, this thesis uses a special photoionization code to model measured emission line ratios. The emitted spectrum namely contains all information about the physical state and the ionizing source. The influence of stellar remnants will be additionally addressed in more detail in section 4.6. It is therefore important to introduce in the next section the spectrum of the DIG and in particular the optical spectral features that are used for testing the models.

## 2.3 Optical spectral features

Of special interest in probing the DIG are the observed forbidden emission lines [NII] $\lambda$ 6583, [SII] $\lambda$ 6716, [OII] $\lambda$ 3727, [OIII] $\lambda$ 5007, [OI] $\lambda$ 6300, and the recombination line HeI $\lambda$ 5876 (all wavelengths are given in Ångström [Å]<sup>5</sup>). Not all emission lines were observed in all galaxies, Table 2.2 gives an overview. The emission line of [OII] $\lambda$ 3727 is the sum of the two transitions at  $\lambda = 3726$  Å and  $\lambda = 3729$  Å. All emission lines are compared with regard to the recombination line H $\alpha$  $\lambda$ 6563. Forbidden emission lines are electric quadrupole or magnetic dipole transitions. The ions get excited through collisions with electrons and due to the low density of the DIG collisional de–excitation is depressed so that radiative transitions dominates. The term ‘forbidden’ refers to the fact that no electric dipole transitions are possible to de–excite this metastable states.

Characteristic features of the DIG–spectrum are the constancy of the ratio [SII]/[NII], the enhanced values of [NII]/H $\alpha$  and [SII]/H $\alpha$  (reaching 1.5 and 1 respectively) in comparison to classical HII regions, and the rise of this ratios with increasing vertical height  $|z|$  from the midplane. Section 4.8 includes a more detailed discussion of the behavior of the ratio

---

<sup>4</sup>there is no unique definition of ‘low energy’, but a value of  $E_{CR} < 1$  GeV/nucleon (Ginzburg & Syrovatskii 1964) seems widely accepted

<sup>5</sup>  $1 \text{ \AA} = 10^{-10} \text{ m}$

Table 2.1: *Optical emission line ratios of the model HII regions and observed in the DIG*

line ratio	30, 000 K	40, 000 K	DIG observed
[NII]/H $\alpha$	0.348	0.100	0.20 ... 1.50
[SII]/H $\alpha$	0.076	0.074	0.15 ... 1.00
[OI]/H $\alpha$	0.002	0.004	0.02 ... 0.15
[OII]/H $\alpha$	0.603	0.865	0.50 ... 2.50
[OIII]/H $\alpha$	0.004	1.159	0.05 ... 0.80
HeI/H $\alpha$	0.005	0.052	0.03 ... 0.07

[SII]/[NII] in respect to data and modeling.

In order to compare the line ratios of the DIG with HII regions a comparison is made with calculated model HII regions using the standard CLOUDY models of the Paris and Lexington meeting on photoionization and shock calculations described in HAZY (Ferland 1997) with an effective stellar temperature of 40,000 K (30,000 K). A summary of all ratios of the model HII region is given in Table 2.1. The models give 0.100 (0.348) for [NII]/H $\alpha$  and 0.074 (0.076) for [SII]/H $\alpha$ .

The ratio [OIII]/H $\alpha$  rises in most cases with increasing distance from the galaxy midplane, reaching up to 0.8, whereas HII region models with an effective stellar temperature of 40,000 K produce more doubly ionized oxygen ions so that [OIII]/H $\alpha$  = 1.159 and models with 30,000 K less ([OIII]/H $\alpha$  = 0.004).

The [OII]/H $\alpha$  ratio reaches in the DIG on average values smaller than 2.5 and bigger than 0.5 in the first 2 kpc above the midplane in contrast to 0.865 (0.603) in HII regions. However due to individual features this ratio can be as high as 13 in the halo (NGC 3079, Otte et al. 2001). [OII] is thus the strongest optical emission and cooling line of the DIG.

The ratio [OI]/H $\alpha$ , although difficult to measure because of its weakness, shows a characteristic increase from 0.02 to 0.15 at  $|z| = 1.5$  kpc. There is no detection of this line for larger  $|z|$  heights as the [OI] line gets too weak. The HII region models give only 0.004 (0.002). This line is therefore another clear indicator for the different physical conditions between a classical HII region and the DIG.

In the case of HeI/H $\alpha$  measurements reach also only up to 1.5 kpc with values of 0.05, indicating an ionizing spectrum of a star with an effective temperature of 40,000 K as the corresponding HII region ratio is 0.052. The HeI/H $\alpha$  line ratio is fairly constant over the detected regions. Due to the weakness of the HeI line and the sensitivity of the observations no detections of it are possible for larger  $|z|$  heights.

The DIG-spectrum is hence characterized by an increase in the line ratios of neutral, singly, and doubly ionized elements challenging photoionization models. The models predict a decrease in highly ionized ions as the flux of corresponding energetic photons is weaker for increasing distance from the source due to absorption and geometrical dilution.

## 2.4 Database

The spectroscopic data of nine galaxies including the Perseus Arm of the Milky Way are used for this study. Table 2.2 summarizes the papers from which the data are taken and the measured scale heights of the corresponding galaxies. The data for the Galaxy were taken with the Wisconsin H $\alpha$  Mapper (WHAM). Various telescopes (ranging from 1.52 m to 4.2 m) and spectrometer were used by different observers to collect the information of the other eight edge-on galaxies. The galaxies represent different Hubble-types with a preference of late-types. The number of slit positions that were observed for each galaxy is indicated in subsection 2.4.1, 2.4.2, and 2.4.3.

The sample is divided into three different subgroups regarding the observed scale height  $h$  of the H $\alpha$  emission. The first subgroup has a scale height of 0.6 kpc and two members (NGC 4302 and UGC 10288), here the DIG can be described with a smooth varying H $\alpha$  brightness. The next subgroup has a scale height of 1 kpc with the Perseus Arm of the Galaxy, NGC 1963, NGC 3044, NGC 4634, NGC 4631, and NGC 3079. The appearance of the DIG of this group is partly quiescence and turbulent. The last subgroup has a scale height of 2.5 kpc, here filaments and shell structures are clearly dominating the DIG, NGC 891 is the prominent example of this group.

### 2.4.1 Scale height $h = 0.6$ kpc

The two galaxies NGC 4302 and UGC 10288 observed by Collins (2001), are grouped together, because they have very similar DIG scale heights ranging from 400 pc to 700 pc, thus smaller than the Milky Way scale height. The authors observed one slit position on NGC 4302 and two on UGC 10288. The line ratios are displayed in Figure 2.4.

The development of the ratio [NII]/H $\alpha$  is similar in both galaxies, it starts at 0.3 in the disk and reaches 1 – 1.3 at a vertical distance of  $|z| = 1.5$  kpc. Whereas the ratio [SII]/H $\alpha$  has a value of 0.25 in the midplane of both galaxies but at  $|z| = 1.5$  kpc the average in NGC 4302 is 0.7 and 1.2 in UGC 10288. The errors of both line ratios increase with distance from the midplane.

The line ratio [OIII]/H $\alpha$  was only measured in UGC 10288. It lies in the range from 0.2 to 0.7 and was only detected out to  $|z| = 1.5$  kpc. The ratio has no clear trend between the midplane and  $|z| = 1$  kpc, it lies between 0.2 and 0.5. However after 1 kpc a pronounced increase is visible up to the last measured point. The error of [OIII]/H $\alpha$  is getting bigger with larger  $|z|$ .

The ratio [OI]/H $\alpha$ , also only detected in UGC 10288, rises clearly from 0.05 in the midplane to 0.15 at  $|z| = 1.5$  kpc at one slit position, but at the other positions it could only be traced out to  $|z| = 0.5$  kpc. This line ratio could only be observed with considerable uncertainties visible in the large error bars. Nevertheless the [OI]/H $\alpha$  ratio of these two galaxies show the highest values of all subgroups.

There are unfortunately no measurements of [OII]/H $\alpha$  or HeI/H $\alpha$  for this subgroup. Thus it is a pressing task for the observers to fill the gap in providing information about the according emission lines.

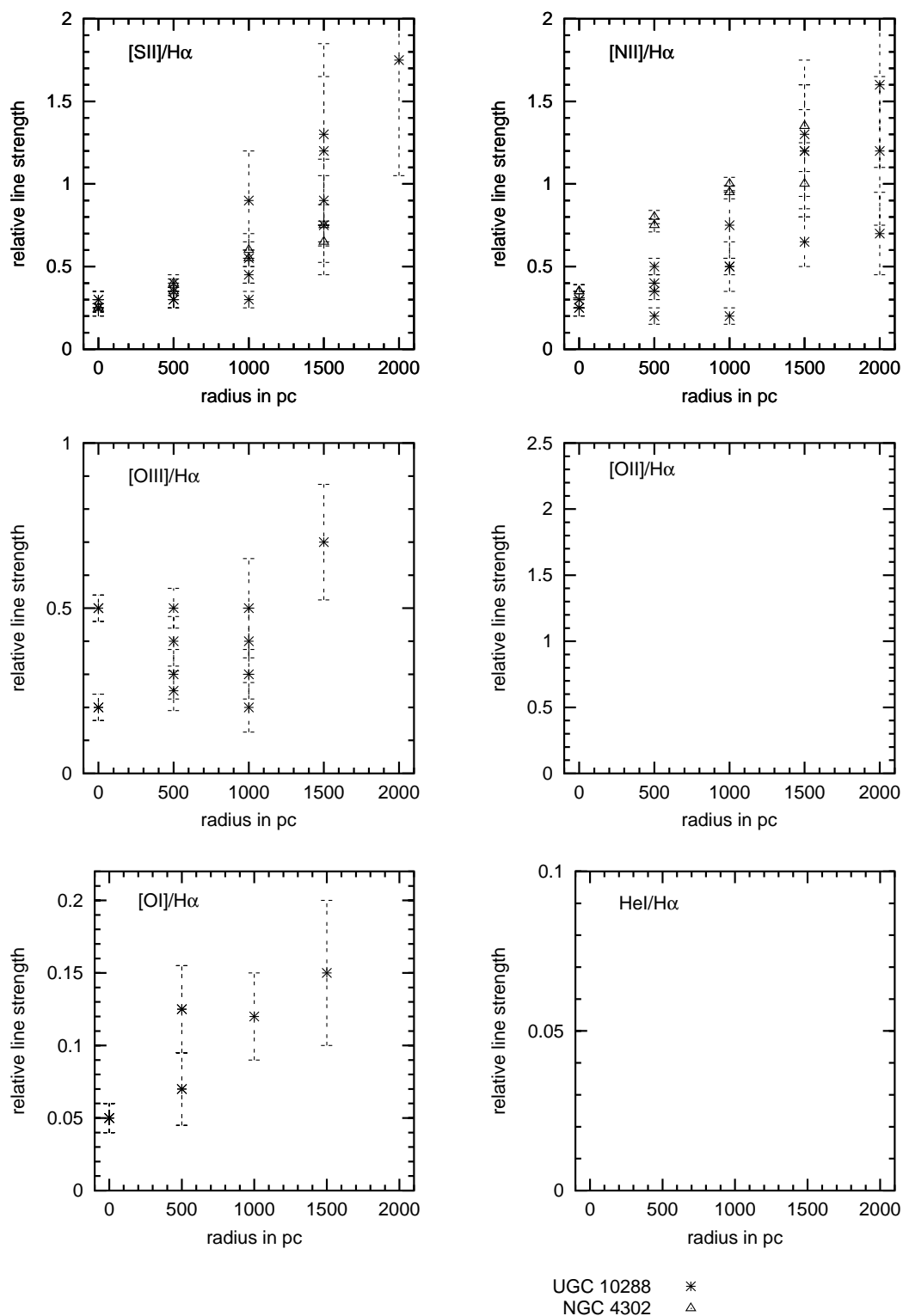


Figure 2.4: Data of scale height group  $h = 0.6$  kpc

The morphology of the DIG in this subgroup can be described with a smooth varying brightness. No strong filaments, or shell structures are observed, the DIG is hence quiescent.

### 2.4.2 Scale height $h = 1$ kpc

This subgroup is further divided into two parts. The first part contains the Perseus Arm of the Milky Way and the second is composed out of the remaining five edge-on galaxies. The used line ratios are displayed in Figure 2.5.

Haffner et al. (1999) used WHAM to measure  $[\text{NII}]/\text{H}\alpha$  and  $[\text{SII}]/\text{H}\alpha$  in the Perseus Arm of the Milky Way.  $[\text{NII}]/\text{H}\alpha$  equals 0.5 at  $|z| = 0.5$  kpc and goes up to 1.8 at  $|z| = 1.75$  kpc, for  $[\text{SII}]/\text{H}\alpha$  the values are 0.25 and 0.95 respectively. The distance to the Perseus Arm which must be used in order to convert the Galactic latitude into vertical distance  $|z|$  is assumed to be 2.5 kpc (Haffner et al. 1999). The measured values are in the upper regime of the line ratios in comparison to the other galaxies, in the case of  $[\text{NII}]/\text{H}\alpha$  it is even the highest. This is not surprising as geometry effects are resulting in an increase of the line ratios  $[\text{SII}]/\text{H}\alpha$  and  $[\text{NII}]/\text{H}\alpha$ . This is discussed in more detail in section 3.4. Therefore the DIG of the Milky Way exhibits the same behavior as the other external galaxies regarding the different observational geometry.

For NGC 4631 scale heights derived from optical emission lines range between 0.9 and 1.2 kpc (Martin & Kern 2001), an average value of 1 kpc is thus adopted. The spectroscopic data of the two observed slit positions are taken from Otte et al. (2001).

The common feature of NGC 1963, NGC 3044, NGC 4634, and NGC 3079 is the lack of information about their scale heights, so a value of 1 kpc is assumed for all of them taking into account the morphology of their DIG. The line ratios were measured by Tüllmann & Dettmar (2000a) and Otte et al. (2001). For all galaxies except NGC 3079 data from two slit positions are available.

The line ratios  $[\text{SII}]/\text{H}\alpha$  and  $[\text{NII}]/\text{H}\alpha$  are characterized by an increase with  $|z|$ . The ratio  $[\text{NII}]/\text{H}\alpha$  reaches values of up to 0.8 at  $|z| = 2$  kpc,  $[\text{SII}]/\text{H}\alpha$  follows with nearly the same trend having a value of 0.75 at  $|z| = 2$  kpc. It is very noticeable that both ratios exhibit a large spread in the data between a height of 500 pc and 1500 pc.  $[\text{NII}]/\text{H}\alpha$  is relatively small in all galaxies, only values between 0.2 and 0.8 are encountered, whereas  $[\text{NII}]/[\text{SII}]$  reaches unity.

The ratio  $[\text{OIII}]/\text{H}\alpha$  shows a very clear increase from 0.15 in the midplane to 0.5 at  $|z| = 2$  kpc. There are only three data points which show a considerable offset at 500 pc and 1000 pc. The spread of the data points increases with  $|z|$ .

The ratio  $[\text{OII}]/\text{H}\alpha$  exhibits in general a rise from about 1 in the midplane to  $\sim 2$  at  $|z| = 2$  kpc for all galaxies. However the spread in the data is relatively large.

The line ratio  $[\text{OI}]/\text{H}\alpha$  increases with  $|z|$ , too. The measurements range from 0.02 in the midplane to 0.12 at  $|z| = 1$  kpc. It could only be detected in NGC 1963 and NGC 3044. The errors are increasing simultaneously with the ratios, the overall trend is nevertheless



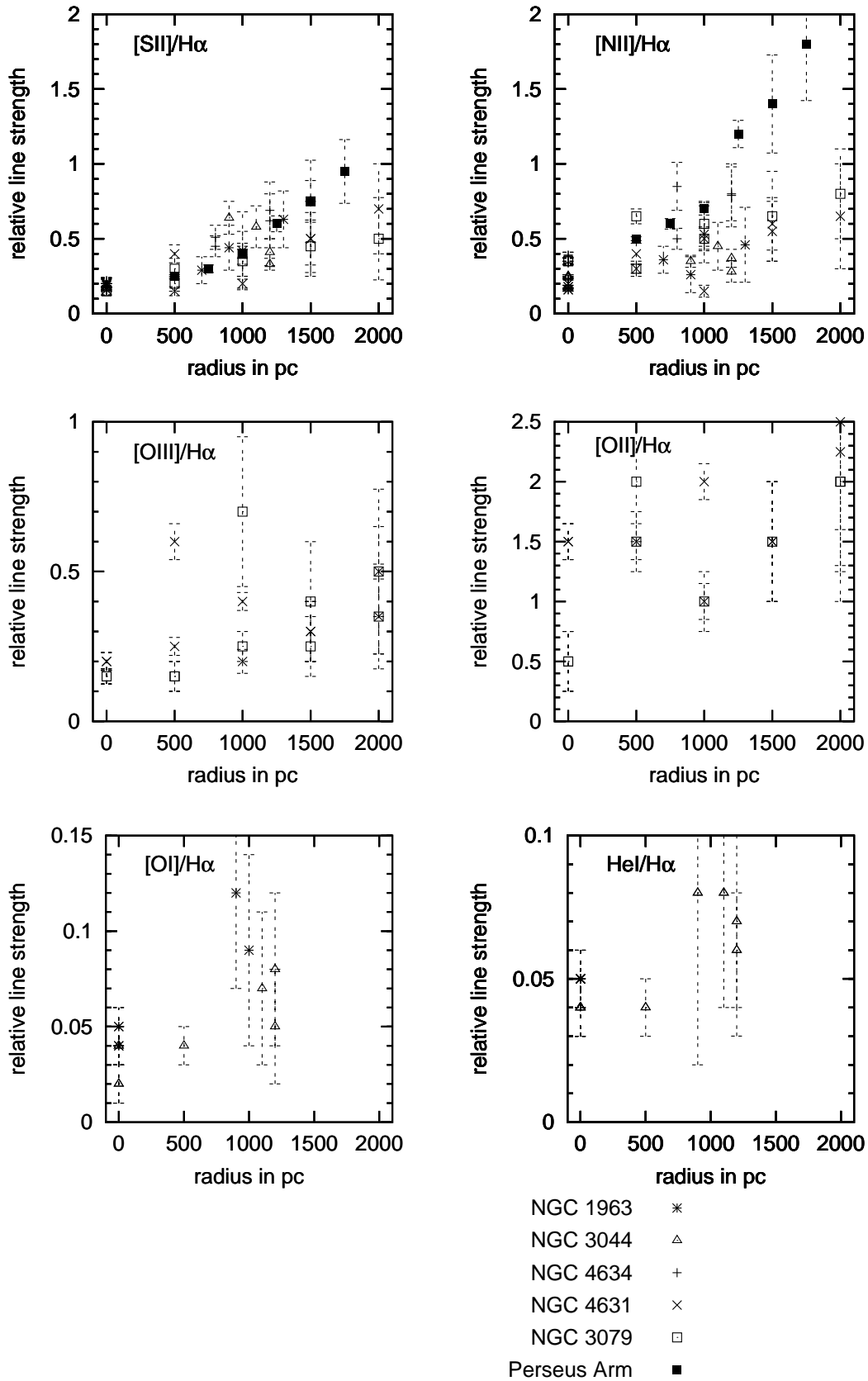


Figure 2.5: Data of scale height group  $h = 1$  kpc

clearly visible.

The HeI/H $\alpha$  ratio was also only measured in NGC 1963 and NGC 3044. It has only small variations with increasing  $|z|$  with an average value of 0.05. The errors of this line ratio are though very large for  $|z| \geq 0.5$  kpc so that there is very little certainty for the trend at higher  $|z|$  heights.

### 2.4.3 Scale height $h = 2.5$ kpc

In NGC 891, one of the best studied edge-on galaxies, the DIG is very turbulent exhibiting prominent, strong filaments and shell structures and the largest scale height in the sample with  $h = 2.5$  kpc. It was observed by several authors, the data of Rand (1998), Collins & Rand (2001), and Otte et al. (2001) which incorporate three slit positions are used. The line ratios are displayed in Figure 2.6.

The general trend for [NII]/H $\alpha$  is a monotonous rise from 0.4 in the plane to 1 – 1.4 at  $|z| = 2$  kpc. [SII]/H $\alpha$  shows also a constant rise from  $\sim 0.2$  in the plane and 0.6 – 0.9 at a height of 2 kpc. Both line ratios have relatively small errors, except for two [NII]/H $\alpha$  observations at  $|z| = 1.5$  kpc and 2 kpc, and [SII]/H $\alpha$  at 2 kpc.

[OIII]/H $\alpha$  rises one order of magnitude from 0.05 to about 0.5 in the halo. The line ratio stays nearly constant during the first 500 pc. The error in this line ratio are getting larger with higher  $|z|$  heights.

The ratio [OII]/H $\alpha$  lies in the interval 0.75 to 1.75. There is a local minimum between  $|z| = 500$  pc and 1000 pc followed by a continuous rise until 2 kpc.

[OI]/H $\alpha$  increases from 0.025 to 0.11 at 1 kpc above the midplane, showing the typical increase of this line ratio with  $|z|$  for the DIG phase. The quality of the data is however much better as indicated by the small error bars.

HeI/H $\alpha$  is relatively constant ranging between 0.023 and 0.045 between the disk and a  $|z|$  height of 1.5 kpc.

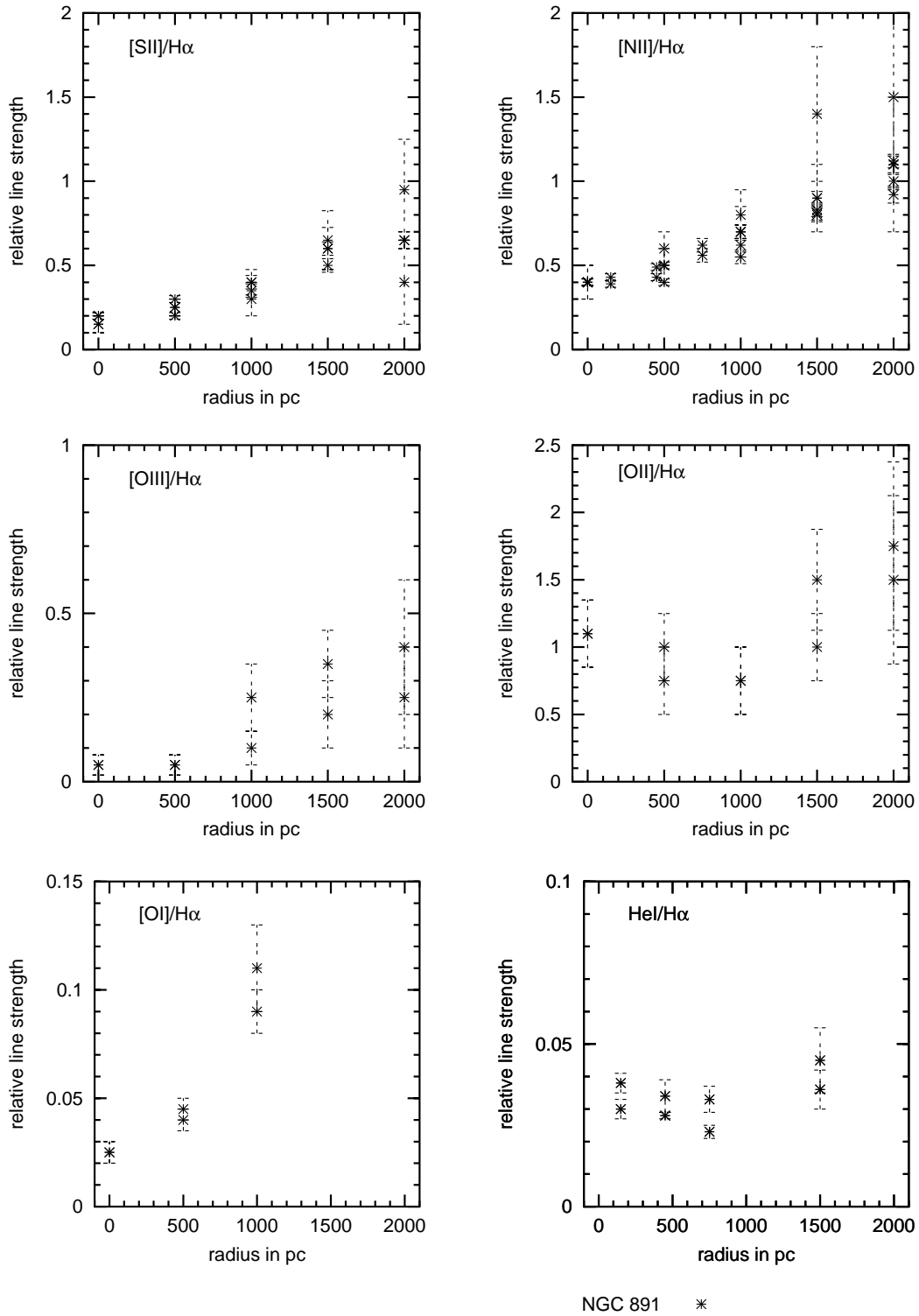


Figure 2.6: Data of scale height group  $h = 2.5$  kpc

Table 2.2: Overview of galaxies and used observed emission lines

galaxy	morphological type, NED(f)	reference	scale height [kpc]	observed emission lines
NGC 4302	Sc	a	0.6	[NII], [SII], H $\alpha$
UGC 10288	Sc	a	0.6	[NII], [SII], [OI], [OIII], H $\alpha$
Milky Way, Perseus Arm	Sbc	b	1	[NII], [SII], H $\alpha$
NGC 1963	Sc	c	1	[NII], [SII], [OI], HeI, H $\alpha$
NGC 3044	SBb	c	1	[NII], [SII], [OI], HeI, H $\alpha$
NGC 4634	SBc	c	1	[NII], [SII], H $\alpha$
NGC 4631	SB	d	1	[NII], [SII], [OII], [OIII], H $\alpha$
NGC 3079	SBc	d	1	[NII], [SII], [OII], [OIII], H $\alpha$
NGC 891	SAb	a, d, e	2.5	[NII], [SII], [OI], [OII], [OIII], HeI, H $\alpha$

<sup>a</sup> *Collins & Rand 2001, ApJ 551, 57*<sup>b</sup> *Haffner et al. 1999, ApJ 523, 223*<sup>c</sup> *Tüllmann & Dettmar 2000, A&A 362, 119*<sup>d</sup> *Otte et al. 2001, ApJ 560, 207*<sup>e</sup> *Rand 1998, ApJ 501, 137*<sup>f</sup> *NED = NASA/IPAC Extragalactic Database*

# Chapter 3

## CLOUDY

### 3.1 Introduction to CLOUDY

The main task of this thesis is the investigation of the physical state of the DIG as is motivated in chapter 2. The observed spectrum and line ratios of this plasma contain the according information and the aim is therefore approached by modeling them. As photoionization by young, hot stars seems to be most likely the dominant process for ionizing and heating the DIG, the photoionization code CLOUDY 94.00 (described by Ferland 2000, 1998, 1997) is used for this purpose. The code is publicly accessible via Internet<sup>1</sup>.

CLOUDY was developed by Gary Ferland in 1978, it got many updates and improvements over the years and is still developing. Due to its flexibility it can be applied to a broad range of physical objects ranging from AGN, PN, HII regions to ISM, and many more. The list of all publications which use CLOUDY is extensive<sup>2</sup> and proves that the code is widely accepted, applied, and even improved by the astronomical community, also by myself<sup>3</sup>. There have been a number of conferences where photoionization codes are tested and compared with each other, the last conference was held in Lexington, Kentucky (Ferland & Savin 2000) and CLOUDY was one of the standards.

CLOUDY was originally written in Fortran and was converted into C in 1999 with the transition of version 90 to 94 (Ferland 2000). The next step will be the conversion into C++. It is designed to run on different platforms. Figure 3.1 gives an impression about the number of lines which made up the code until 1996. There is a notable increase in this number after 1984 and 1992, which is partly due to the enlarged and updated atomic data section. The continuous effort to improve the code is clearly reflected in its growth.

CLOUDY is a command driven code, a list of special commands is successively read in, stored, and processed. The code is self-regulating, if something is amiss it will flag it and

---

<sup>1</sup>at the web page <http://thunder.pa.uky.edu/cloudy>

<sup>2</sup>see [http://thunder.pa.uky.edu/cloudy/papers\\_using\\_Cloudy.htm](http://thunder.pa.uky.edu/cloudy/papers_using_Cloudy.htm)

<sup>3</sup>see <http://thunder.pa.uky.edu/cloudy/acknowledgements.htm>

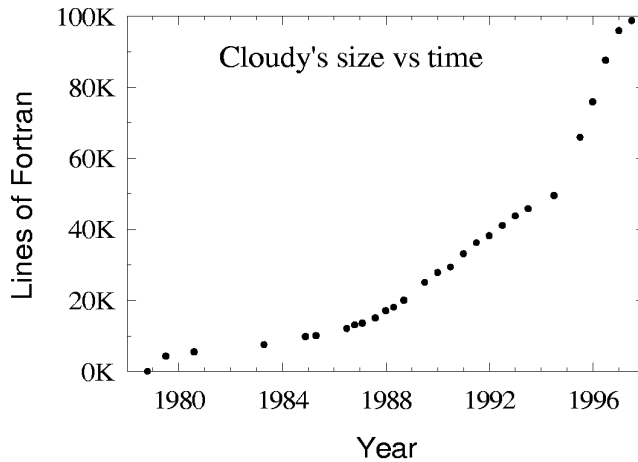


Figure 3.1: *Number of Fortran lines making CLOUDY from 1978 until 1996 (HAZY, Ferland 1997)*

stop the calculation giving clues why and where the error occurred. The output is an ASCII-file which must be treated further in order to extract the information wanted.

## 3.2 Photoionization models with CLOUDY

CLOUDY models the situation that a central object heats and ionizes a gas layer that spherically surrounds it. The response of the gas layer is calculated, the ionization and temperature structure is computed, together with the emission line spectrum. CLOUDY handles approximately 10,000 emission lines. It assumes a spherical symmetry, radiative-collisional equilibrium, and a stationary (homogeneous) medium. The corresponding general heat conduction equation of a viscous fluid (Landau & Lifschitz 1981) reads

$$\rho T \left[ \frac{\partial s}{\partial t} + v \cdot \nabla s \right] = \text{div}(\kappa \nabla T) + \sigma_{ik} \frac{\partial v_i}{\partial x_k} + \Gamma(\rho, T) - \Lambda(\rho, T) \quad (3.1)$$

with  $\frac{\partial s}{\partial t} + v \cdot \nabla s = \frac{ds}{dt}$  the total derivative of the entropy  $s$ ,  $\kappa$  the heat conductivity,  $v$  the velocity of the fluid, and  $\sigma_{ik}$  the stress tensor. The equation reduces further to the condition that the heating rate  $\Gamma(\rho, T)$  equals the cooling rate  $\Lambda(\rho, T)$

$$\Gamma(\rho, T) = \Lambda(\rho, T) \quad (3.2)$$

where all spatial and time derivatives are set to zero because of the stationary state. The terms with derivatives in equation (3.1) may play a more important role near the midplane where turbulent phenomena are likely to occur more pronounced, weakening the assumption of a stationary state. As the models concentrate on large distances from the midplane these effects should be small and are further assumed to be negligible.

Although CLOUDY can handle only spherical geometries it is possible to specify an effective plane parallel layer which is the mode that is used. Figure 3.2 illustrates the geometry of the used models. The gas layer starts at a radius  $r_0$  away from the ionizing source (illuminated side) and has a certain thickness  $\Delta r$ . If the ratio  $\Delta r/r_0$  is smaller than 0.1 the geometry is close to plane parallel, for  $0.1 < \Delta r/r_0 < 3$  cylindrical, and for  $\Delta r/r_0 \geq 3$  the geometry is spherical. The layer itself is numerically divided into different zones under the requirement that the physical conditions in each zone are nearly constant. The temperature and pressure difference within each zone must be smaller than 5%. The thickness of each zone as well as their total number is defined by CLOUDY during the calculation. The varying thickness of the zones is also indicated in the sketch. The normal line of sight CLOUDY takes into account is displayed in Figure 3.2, the line intensities are thus an integration over the whole thickness of the gas layer. The observations used for the DIG in edge-on galaxies have a line of sight perpendicular to this one, this is being taken into account as described in section 3.4.

Despite the shape of the simulated gas cloud one must specify if the geometry is 'open' or 'closed'. The models use an 'open' geometry which means that photons traveling from one side of the cloud through the center and striking the other side are neglected. The different sides are hence not connected with each other, this is consistent with observations as the optical depth is high enough to prevent photons traveling through the midplane.

The largest radius CLOUDY can handle is  $10^{30}$  cm, the largest column density  $n_{c,max} = 10^{30} \text{ cm}^{-2}$ . The number density cannot exceed  $10^{13} \text{ cm}^{-3}$  which is of no concern for the models used here. Due to a numerical limit CLOUDY should only be used with densities bigger than  $10^{-6} \text{ cm}^{-3}$  which is a conservative limitation, however there is no real physical reason for this. The energy range for the ionizing continuum one must specify in order to run a model is  $1 \cdot 10^{-5} \text{ Ryd} < E < 7 \cdot 10^6 \text{ Ryd}^4$ . The temperature range CLOUDY can handle is  $10 \text{ K} < T < 10^9 \text{ K}$ , the upper limit is caused by the inability of the code to treat relativistic effects and at that temperatures the electrons become relativistic.

### 3.3 Heating–cooling balance

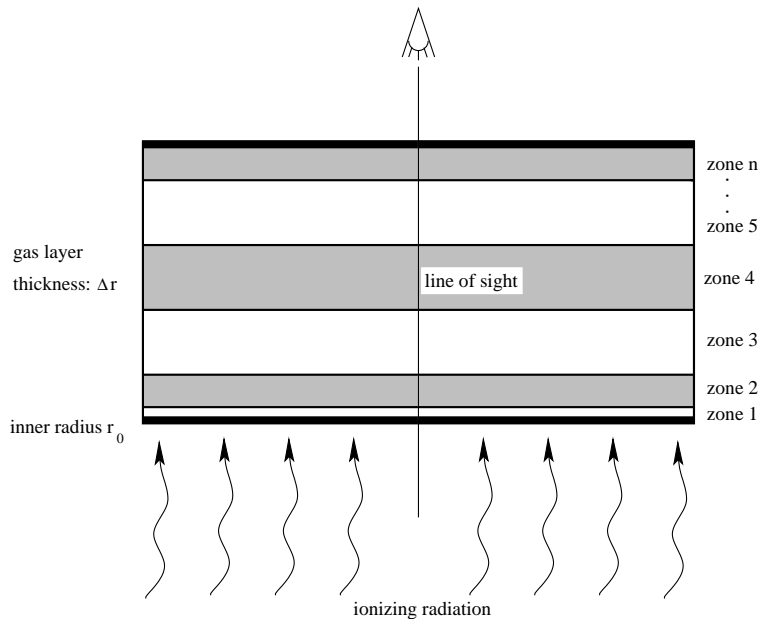
Before proceeding with the parameters for a model calculation the most important heating and cooling processes of a photoionized low density nebula will be presented.

The main heating process in the models is photoionization where a photon with an energy  $h\nu$  ionizes an atom or ion providing the resulting free electron with a kinetic energy equal to the energy of the photon less than the ionization energy  $\frac{1}{2}mv^2 = h(\nu - \nu_0)$ . The resulting free electron is rapidly thermalized. The net heating rate (in a pure hydrogen nebula) is then

$$\Gamma_P = n_e n_P \alpha_A(\text{H}^0, \text{T}) \frac{3}{2} k T_i \quad (3.3)$$

---

<sup>4</sup>1 Ryd = 13.6 eV = 911.6 Å

Figure 3.2: *Geometry of the CLOUDY models*

where  $n_e$ ,  $n_P$  are the number densities of the electrons and protons respectively,  $\alpha_A(H^0, T)$  the recombination coefficient of hydrogen summed over all levels, and  $T_i$  the initial temperature of the newly created photoelectrons. If not stated otherwise all formulae used in this section are cited from Osterbrock (1989).

Another heating mechanism is photoelectric grain heating ( $\Gamma_G$ ), here the photons liberate electrons from grains leaving a positively charged grain behind (see e.g. Weingartner & Draine 2001, Spitzer 1978, Draine 1978). The electrons thermalize, distributing the photon energy and rising the gas temperature. The models show that this process accounts for approximately 5% of the total heating rate.

The dominant cooling source is collisional excitation cooling involving forbidden emission lines. Forbidden transitions are electric quadrupole or magnetic dipole transitions sometimes with spin changes which therefore have a low transition probability  $A$ ; for the emission lines of interest:  $10^{-5} \text{ s}^{-1} \leq A \leq 10^{-2} \text{ s}^{-1}$ , Table 3.1 gives an overview. Atoms or ions are experiencing inelastic collisions with electrons, leading to transitions which de-excite via forbidden transitions. As the excitation levels lie in the same energy range (1 eV)<sup>5</sup> as the average temperature ( $T = 10,000 \text{ K}$  or  $kT \approx 1 \text{ eV}$ ), these levels get very easily excited and therefore dominate the cooling. Due to the low density of the medium collisional de-excitation is negligible in comparison to the radiative transition.

The rate of this process is described with the dimensionless collision strength  $\Omega_{ij}$  which is a slow function of temperature. The cooling rate in a 2 level approximation which is

---

<sup>5</sup>1 eV =  $1.6022 \times 10^{-19} \text{ J}$



Table 3.1: *Transition probabilities of observed emission lines*

Emission line	Wavelength in Å	Transition probability $A$ in $s^{-1}$
[NII]	λ6583	$3.0 \times 10^{-3}$
[SII]	λ6716	$4.6 \times 10^{-4}$
[OI]	λ6300	$6.9 \times 10^{-3}$
[OII]	λ3729	$4.1 \times 10^{-5}$
[OII]	λ3726	$1.3 \times 10^{-4}$
[OIII]	λ5007	$2.1 \times 10^{-2}$

appropriate for the emission lines under consideration can be represented as

$$\Lambda_C = n_e n_1 \frac{8.629 \cdot 10^{-6} \Omega_{1,2}}{T_4^{1/2}} \frac{\Omega_{1,2}}{\omega_1} \exp(-\chi/kT) h\nu \quad (3.4)$$

where the transition occurs between the two levels 1 and 2,  $\omega_1$  is the statistical weight of level 1 (ground level),  $T_4$  is the temperature in units of  $10^4$  K, and  $\chi$  is the ionization potential between the two levels.

The main cooling of the plasma under consideration comes from the emission lines [OII], [OIII], [NII], and [SII] with line ratios of  $[OII]/H\alpha > 1$ ,  $0.1 < [OIII]/H\alpha < 1$  and  $0.5 < [NII], [SII]/H\alpha < 2$ . Important contributions come also from the forbidden IR fine-structure lines of [CII]λ157μm and [SIII]λλ18.7, 33.4μm with ratios of [CII], [SIII]/ $H\alpha < 1$ . According to the models [OII] alone contributes  $\sim 15\%$  to the total cooling and 'is' therefore the main cooling line (i.e. [OII]λλ 3726, 3729 Å).

Another cooling process is recombination radiation which is dominated by hydrogen because of its abundance, the cooling rate is given by

$$\Lambda_R(H) = n_e n_P kT \beta_A \quad (3.5)$$

with  $\beta_A$  the recombination cooling coefficient. Unlike the collisionally excited emission lines the recombination lines are not strongly sensitive to the term  $kT$ , as they omit the factor  $\exp(-\chi/kT)$ . They are therefore not as sensitive for temperature changes than the forbidden emission lines. Moreover the volume emissivity for a recombination line of ion  $X^{+i}$  is proportional to  $n(X^{+i+1})$  while a collisionally excited emissivity is proportional to  $n(X^{+i})$ . Forbidden emission lines are thus a clear indicator for the most important ionization stages of the plasma under consideration. The net free-bound cooling is about 10% of the total.

A rather important process for special emission lines, which is not covered by Osterbrock (1989), is dielectronic recombination, wherein the recombining electron disposes its initial energy by raising a bound electron to an excited level, see Figure 3.3. The inverse process is called autoionization. As an example, which is important for the calculations, one starts with a doubly ionized sulphur atom in the ground state  $S^{++}$  ( $E_g^{++}$ ) and let it react with an

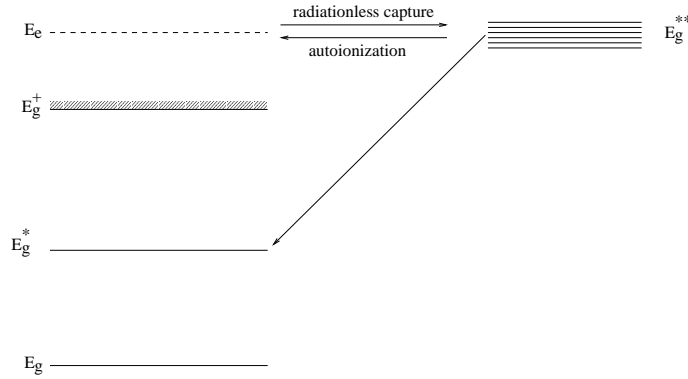
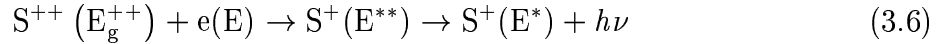


Figure 3.3: *Energy level diagram for dielectronic recombination in a low density plasma*

electron  $e(E)$  with energy  $E$ , the result is singly ionized sulphur atom in a doubly excited state  $S^+(E^{**})$  (radiationless capture). This state is highly unstable and strongly broadened due to its short life time and either decays back into  $S^{++}(E_g^{++})$  and  $e(E)$  (autoionization) or it decomposes into a singly ionized sulphur atom in a singly excited state  $S^+(E^*)$  and a photon with energy  $h\nu$  (dielectronic recombination)



Dielectronic recombination is obviously a two–step resonant process i.e. it can only take place at certain free–electron energies while e.g. radiative recombination is a one–step process involving a continuous distribution of free–electron energies. Quantum mechanically though the two processes (dielectronic recombination and radiative recombination) are indistinguishable. The amount of cooling dielectronic recombination is contributing is therefore contained in  $\Lambda_R$ . But as this process rises the amount of singly ionized elements it also increases  $\Lambda_C$  for the forbidden emission lines.

Continuum processes such as free–free (bremsstrahlung) and two photon radiative transitions give contributions of  $\sim 5\%$  to the total cooling of the plasma according to the models. Reynolds (1992) quoted 20% for the two photon continuum near 1600 Å and a negligible contribution of the free–free continuum.

Free–free emission ( $\Lambda_{ff}$ ) is strongest for IR and radio frequencies competing with the 2.73 K cosmic background, synchrotron and dust emission. Two photon radiative processes  $\Lambda_{2p}$  can give appreciable contributions to the continuum between 3500 Å and 5000 Å for densities  $n \ll 10^4 \text{ cm}^{-2}$  which is fulfilled in the DIG.

The continuum emission will not be discussed further as this thesis is concentrating on line emission with a sufficient signal to noise ratio in the data that allows to identify it unambiguously against the (stellar) background continuum.

With all the different processes the heating–cooling balance equations obtains following final form

$$\Gamma_P + \Gamma_G = \Lambda_C + \Lambda_R + \Lambda_{ff} + \Lambda_{2p} \quad (3.7)$$

It is convenient to rewrite this equation as

$$(\Gamma_P - \Lambda_R) + \Gamma_G = \Lambda_C + \Lambda_{ff} + \Lambda_{2p} \quad (3.8)$$

where  $\Gamma_P - \Lambda_R$  represents an “effective heating rate”, i.e. the net energy gained in photoionization processes with the recombination losses already subtracted.

### 3.4 Parameters

In order to run a CLOUDY model four parameters have to be specified. The necessary input parameters are: ionization parameter, chemical abundance of the gas being ionized, density distribution, and input spectrum.

In order to restrict the parameter space all but one parameter are held fixed.

The dimensionless ionization parameter is defined as the ratio of the hydrogen ionizing photon flux to the hydrogen density at the Strömgen Sphere of the cloud

$$U = \frac{\Phi_{\text{H}^0}}{n_{\text{H}} \cdot c} = \frac{Q_{\text{H}^0}}{4\pi \cdot R_s^2 \cdot n_{\text{H}} \cdot c} \quad (3.9)$$

where  $\Phi_{\text{H}^0}$  is the hydrogen ionizing photon flux,  $n_{\text{H}}$  the hydrogen density,  $Q_{\text{H}^0}$  the number of hydrogen ionizing photons emitted by the source,  $R_s$  is the Strömgen Radius, and  $c$  the speed of light<sup>6</sup>. With

$$Q_{\text{H}^0} = \frac{4\pi}{3} \cdot R_s^3 \cdot n_{\text{H}}^2 \cdot \alpha_B \quad (3.10)$$

where  $\alpha_B$  is the recombination coefficient of H to levels  $n \geq 2$ , it follows that  $U \propto R_s$  (Osterbrock 1989). The value of the ionization parameter is fixed with a certain Strömgen Radius.  $U$  is determined by the requirement that at a distance of 2 kpc, the portion of neutral hydrogen equals 20%, i.e.  $R_s \approx 2$  kpc. This condition was introduced in order to have a common basis to compare the different models among each other. Variations in chemical abundance, density, or manipulation of the heating budget influence  $U$ . The values of  $U$  for different models are summarized in Table 4.1.

A plane parallel geometry is assumed, this is by definition in CLOUDY the case if the ratio of the thickness of the gas layer to the separation between ionizing source and gas layer is smaller than 0.1. Furthermore the geometry is treated as open, i.e. only photons from one half of the sphere are considered, photons scattered from the other half are just neglected. The adopted values of the element abundances are those given for the ISM in CLOUDY. The ISM mixture is based on diffuse ISM measurements and is an average from the work of Cowie & Songaila (1986) and Savage & Sembach (1996), additionally the S/H and N/H abundances are set equal to that used in Haffner et al. (1999),  $1.86 \times 10^{-5}$  and  $7.5 \times 10^{-5}$  respectively. Graphite and silicate grains are present in the gas, although not with varying sizes (Baldwin et al. 1991).

---

<sup>6</sup>speed of light  $c \approx 2.9979 \times 10^8$  m/s

The interaction with CR is taken into account as described in Ferland et al. (1984), a constant CR density with  $n_{\text{CR}} = 2 \cdot 10^{-9} \text{ cm}^{-3}$  is used. The resulting ionization rate of neutral hydrogen ( $\sim 2 \cdot 10^{-17} \text{ s}^{-1}$ ) equals the (very uncertain) value quoted by Tielens and Hollenbach (1985). The code assumes that the gas is optically thin to CR, the simplest case is treated where CR are ionizing and heating the gas resulting from two-body Coulomb interactions only. With this implementation CR have only a minor effect on the resulting emission lines and can be neglected. However as stated in chapter 2 there has to be further investigations in order to determine their role, especially of low energy CR.

An exponential density law is considered with an electron midplane density of  $0.2 \text{ cm}^{-3}$ , reflecting the conditions in the Milky Way

$$n(|z|) = n(z=0) \cdot e^{-|z|/h} \quad (3.11)$$

a constant filling factor of 20 % is assumed, i.e. only 1/5 of the whole volume is filled with this gas phase. The scale heights for the models are chosen according to Table 2.2.

All observations give information about the line ratios at different positions orthogonal to the usual sight line of a CLOUDY calculation as given in Figure 3.2. However, the correct local line ratios are represented by the ratios of the volume emission coefficients  $\epsilon_V$

$$\begin{aligned} \frac{I_1}{I_2} &= \frac{\int dz \epsilon_{V_1}}{\int dz \epsilon_{V_2}} \\ &\approx \frac{\epsilon_{V_1}}{\epsilon_{V_2}} \end{aligned} \quad (3.12)$$

the according sight line were the necessary condition  $\epsilon_V = \text{constant}$  is fulfilled is displayed in Figure 3.4. Relation (3.12) is used for comparing the data and the models. The treatment of the Perseus Arm data is different due to our position in the Milky Way as shown in Figure 3.5. Every measured 'point' contains contributions from different  $|z|$  heights ( $\epsilon(z_1)$  to  $\epsilon(z_2)$ ), this effect is taken into account by integrating over the particular sight line. The numerical integration is performed by interpolating the results of the emission coefficients of the different zones with functions of order one. The distance to the Perseus Arm was taken to be 2.5 kpc and the thickness of the arm 1 kpc, as used in Haffner et al. (1999).

The free parameter is the input spectrum, four different stellar spectra are used, which fall into two categories. On the one hand LTE<sup>7</sup> models like the Black Body spectrum and the Atlas models of Kurucz (1991) with static atmospheres where the occupation numbers of atomic levels follow LTE. On the other hand the Non-LTE models CoStar of Schaerer et al. (1996) and WMbasic of Pauldrach et al. (2001) which incorporate expanding atmospheres and stellar winds, the occupation numbers of atomic levels are determined by equations of statistical equilibrium. The WMbasic model is applied either with a stellar dwarf spectrum (main sequence) or a stellar supergiant spectrum. The effective stellar temperature is chosen to be 40,000 K for all spectra as is suggested by the

---

<sup>7</sup>LTE = Local Thermal Equilibrium

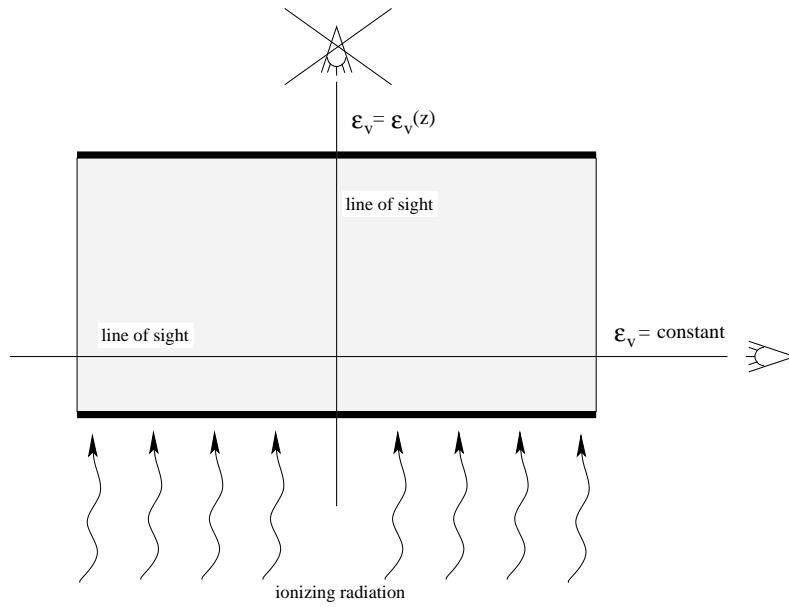


Figure 3.4: *Sight lines according to observations of edge-on galaxies*

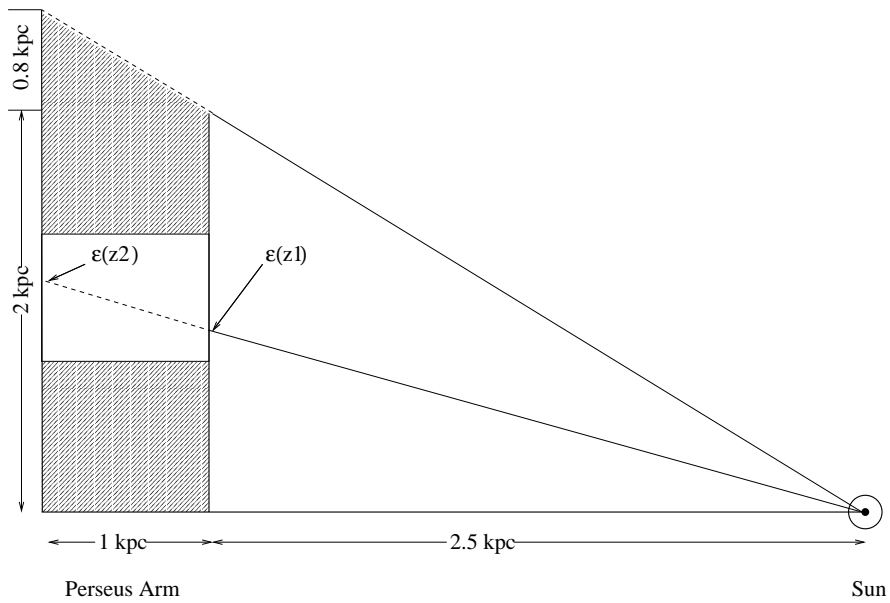


Figure 3.5: *Observations of the Perseus Arm*

HeI/H $\alpha$  line ratio (see section 2.3). Figure 3.6 shows the flux of all different spectra in the crucial wavelength range from 200 Å to 1000 Å. Both the Black Body and Atlas spectrum are merely chosen as a comparison, the Atlas model is a 'prominent' spectrum which was and still is extensively used in other investigations. It is a kind of a standard for lower stellar effective temperatures where Non-LTE effects can be neglected.

The main difference between the CoStar and WMbasic model is the inclusion of line blanketing due to metal lines, only the WMbasic models take this into account and are hence more realistic. As a result the UV-flux of the CoStar model is much higher than that of the others as is seen in Figure 3.6, the difference reaches up to two orders of magnitude (e.g. at  $\lambda = 230$  Å). The CoStar model acts therefore as a test for the effects of a much harder incident radiation. The main differences between the WMbasic supergiant and dwarf spectrum lie in the emission and absorption line characteristics, leading to the trend that the supergiant spectrum has less flux between 250 Å and 550 Å than the dwarf spectrum. As supergiant and dwarf spectra with the same effective temperature are considered, one is dealing with two spectral types (O6.5 I,  $\log g^8 = 3.6$  and O7.5 V,  $\log g = 3.75$ ). As the standard input spectrum the WMbasic supergiant spectrum is chosen. Typically more hot supergiants than dwarfs ( $T_{\text{eff}} > 35,000$  K) are observed in OB associations. Moreover dwarf stars with temperatures above  $\sim 35,000$  K are staying only a very short time on the main sequence before evolving into supergiants (Pauldrach 2002). It is therefore appropriate to declare the supergiant spectrum as the standard one.

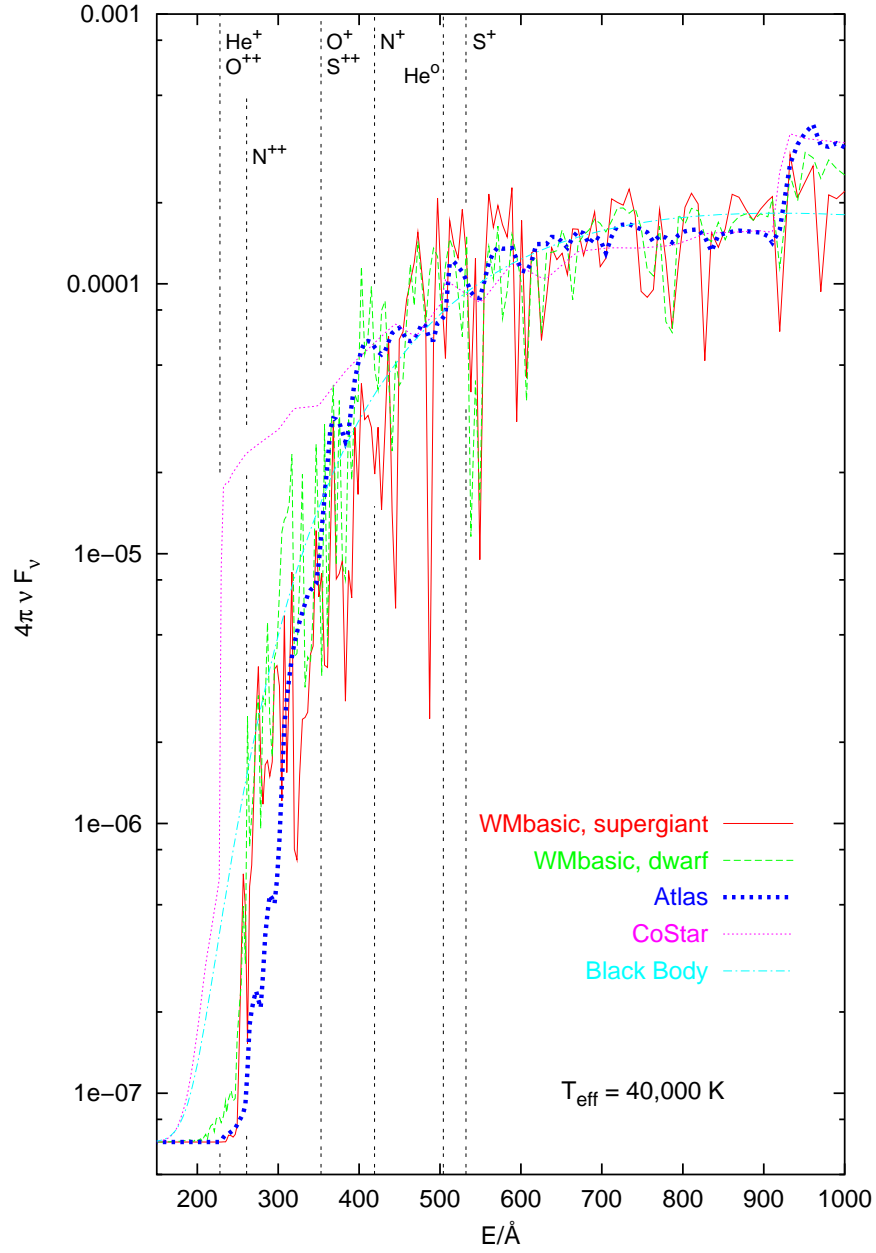
As a measure of the spectral energy distribution (SED) and hence the spectral hardness Table 3.2 displays the photon fluxes of the different input spectra in three wavelength bins normalized to the Black Body spectrum. The wavelength interval from 506 Å to 228 Å exhibits the largest deviations between the input spectra. The order of spectral hardness is (starting with the softest): Black Body, WMbasic supergiant, Atlas, WMbasic dwarf and Costar. The difference between the WMbasic supergiant and the Atlas spectra amounts to less than 10%, to the WMbasic dwarf spectrum 35%, and to the CoStar spectrum 75%. As will be shown in chapter 4 and 5 this wavelength range is the essential one regarding the behavior of the model predictions. The Costar model has furthermore a factor of  $\sim 2.5$  more flux in the interval 228 Å to 46 Å than the WMbasic and Atlas models. The last column of Table 3.2 refers to the average energy of the hydrogen ionizing continuum in Ryd weighted by photon number

$$\langle h\nu \rangle = \frac{\int_{1\text{Ryd}}^{\infty} d\nu 4\pi F_{\nu}}{\int_{1\text{Ryd}}^{\infty} d\nu 4\pi F_{\nu}/h\nu} \quad (3.13)$$

the absolute value of  $\langle h\nu \rangle$  of the Black Body spectrum is 1.377 Ryd. It is obvious that the order regarding the spectral hardness of this quantity is identical to the one of the middle wavelength interval stressing the importance of this energy range and clarifying the gap between the CoStar spectrum and the other spectra.

---

<sup>8</sup> $g$  = stellar surface gravity

Figure 3.6: *Input spectra for the photoionization models regarding the UV photon flux*Table 3.2: *SED of the different input spectra normalized to the Black Body spectrum*

Input spectrum	$\Phi(911.6 - 506 \text{ \AA})$	$\Phi(506 - 228 \text{ \AA})$	$\Phi(228 - 46 \text{ \AA})$	average $\langle h\nu \rangle$
Black Body	1	1	1	1
WMbasic, supergiant	0.97	1.02	0.56	1.01
WMbasic, dwarf	0.92	1.36	0.58	1.03
Atlas	0.93	1.11	0.56	1.02
CoStar	0.88	1.75	1.34	1.09





# Chapter 4

## Applications of CLOUDY

### 4.1 General remarks

This chapter is dealing with the application of the CLOUDY models (as described in chapter 3) to the data. Section 4.2 outlines the treatment of the data, the models, and their linking. The following section discusses some general remarks about the trend of the line ratios in regard to the scale height groups in the data and the models. The effect of different input spectra on the ionization structure and temperature gradient is addressed.

Section 4.4 contains the discussion of all scale height groups with the models having varying input spectra each with an effective stellar temperature of  $T_{\text{eff}} = 40,000$  K, a midplane density of  $n(0) = 0.2 \text{ cm}^{-3}$ , and a constant filling factor of 20%. As a standard input spectrum the WMbasic supergiant model is used (see section 3.4) in investigating other effects and approximations. This is done to restrict the parameter space. The data of the different galaxies have different symbols in all diagrams and the models are represented by different line styles as indicated by the key below the graphs. Section 4.5 is addressing different effective temperatures and section 4.6 investigates the influence of a second input spectrum added to the standard model, both sections are using the standard model with specific modifications.

Section 4.7 introduces an extra heating source and shows its consequences for the Perseus Arm and NGC 891. The need of an extra heating rate is a vital discussed topic in the literature in order to explain the observed line ratios of the DIG.

The line ratios  $[\text{NII}]/\text{H}\alpha$  and  $[\text{SII}]/\text{H}\alpha$  are discussed in particular in section 4.8. It is shown that the slope in the  $[\text{SII}]/\text{H}\alpha$ – $[\text{NII}]/\text{H}\alpha$ –diagram reveals no information about the global metallicity of a galaxy but about the evolution and star formation history.

The last section (4.9) is addressing another physical parameter, the column density, with which the observations and the model for the Perseus Arm are compared. The column densities of Al III and S III are used in particular. It is demonstrated that the discussed ions are predominantly produced in the DIG as is expected.

In the following discussion the name of the used stellar input spectrum is adopted as

a synonym for the model itself to simplify the reading. Different line styles represent the diverse input spectra, the line style encoding is the same for all diagrams. The standard model is always represented by the solid line in all figures.

## 4.2 Handling data and models

The modeling of the line ratios was done without any fitting to the data. Therefore no criteria for the detailed reproduction of the individual line ratios at certain heights  $|z|$  were introduced, only the scale heights  $h$  are chosen according to the data. There is thus no 'best-fit' to the data so the models are independent of the observational quality of the data, individual features, and small scale variations of the galaxy sample. It becomes also more reliable and reasonable to compare the models among each other and to the large scale variation of the line ratios as extracted from the inhomogeneous data sample. The only parameter discriminating between the galaxy-groups is the scale height of the density. Another important issue for all models is the restriction of 20 % neutral hydrogen at 2 kpc, that allows to compare the different models with various input spectra on a common basis. The models moreover reach with this restriction the real extension of the observed DIG-layers and match the deduced ionizing photon fluxes (see section 5.3.2). The CLOUDY models are thus positioned between ionization and matter bounded regions.

The data are treated in the way that only measurements were considered at certain vertical heights  $|z|$  ( $|z| = 0 - 2$  kpc,  $\Delta z \approx 250$  pc) for all galaxies and slit positions if possible. Observations of different sides of a galaxy are plotted in the same diagram. The limit of 2 kpc was introduced because this is the range in which most data are available, only very few measurements were made for higher heights. Moreover Rossa & Dettmar (2003b) reason that out of a sample of 30 galaxies showing DIG-layers this value is indeed a typical one. In some cases a couple of CCD rows were binned in order to increase the signal to noise ratio so that it is also not reasonable to make finer steps in  $|z|$  heights. The data show nonetheless individual features but their influence is averaged out by working with more than one galaxy and slit position.

The highly interacting galaxy NGC 5775 was not considered for this thesis, because it has very special features. The DIG was observed at very prominent filaments reaching up to 9 kpc above the disk (Tüllmann et al. 2000b), the standard model is therefore not applicable for this galaxy. As this thesis is concentrating and trying to work out the general characteristics of the DIG, this galaxy is not adequate for the investigation. However it seems to be an appropriate object where other heating mechanisms than photoionization dominate and should be the topic of another study.

Another advantage of this thesis is that the sample of used optical emission lines is enlarged in comparison to previous investigations (Mathis 2000, Bland-Hawthorn et al. 1997, Domgörgen & Mathis 1994). It is very important that different ionization stages of oxygen with the lines [OI], [OII], and [OIII] are now included into the discussion. The models are therefore not concentrating on just a few emission lines so that more extensive tests can be performed. This is presented in section 5.2 in more detail.

## 4.3 Models and data

### 4.3.1 Trends in the data

All line ratios except  $\text{HeI}/\text{H}\alpha$ , which stays nearly constant, increase with increasing distance from the midplane.  $[\text{SII}]/\text{H}\alpha$  and  $[\text{NII}]/\text{H}\alpha$  show the highest values in the group with  $h = 0.6$  kpc. Whereas the group with  $h = 2.5$  kpc has the smallest  $[\text{OIII}]/\text{H}\alpha$  and  $[\text{OII}]/\text{H}\alpha$  ratios. The absolute values of  $[\text{OII}]/\text{H}\alpha$  and  $[\text{OIII}]/\text{H}\alpha$  however are getting smaller with increasing  $h$  whereas the other line ratios show no clear trend with scale height. The ratio  $[\text{OI}]/\text{H}\alpha$  has higher values with decreasing scale height. It shows a clear rising trend with increasing distance from the midplane for all subgroups. The approximate constant  $\text{HeI}/\text{H}\alpha$  supports the hypothesis that the main excitation mechanism is nearly the same for all galaxies, i.e. young, hot O stars with an effective temperature of around 40,000 K (see section 3.4).

### 4.3.2 Trends in the model predictions

For the modeled line ratios all but  $\text{HeI}/\text{H}\alpha$  and  $[\text{OIII}]/\text{H}\alpha$  increase with increasing  $|z|$  for each scale height. All models have similar runs of  $[\text{SII}]/\text{H}\alpha$ ,  $[\text{NII}]/\text{H}\alpha$ , and  $[\text{OI}]/\text{H}\alpha$  with the exception of the CoStar model with larger deviations after  $|z| = 1$  kpc. The models show larger deviations with  $[\text{OIII}]/\text{H}\alpha$ ,  $[\text{OII}]/\text{H}\alpha$ , and  $\text{HeI}/\text{H}\alpha$ . The absolute values of the line ratios of  $[\text{OII}]/\text{H}\alpha$ ,  $[\text{SII}]/\text{H}\alpha$ , and  $[\text{NII}]/\text{H}\alpha$  are getting smaller with increasing scale height whereas  $[\text{OIII}]/\text{H}\alpha$  shows the opposite trend.  $[\text{OIII}]/\text{H}\alpha$  has for the CoStar model a clear local minimum at a radius of 200 pc for all scale heights reflecting the depression in the temperature run (see Figure 4.2). The diameter of this 'dip' is increasing with scale height, so that for  $h = 2.5$  kpc it can also be seen in the predictions of the other models.

### 4.3.3 Spectral energy distribution of the input spectra

The differences in the flux of the various input spectra is clearly reflected in the ionization structure of the models. Figure 4.1 shows the ionization structure of different elements and ionization stages for the subgroup with  $h = 2.5$  kpc. This scale height is used for this purpose in order to minimize the effect of changing density upon the emission lines resulting in a very sharp Strömgren Sphere. The neutral and ionized hydrogen show nearly no differences with respect to input spectra, this is the consequence of the stop condition (20% neutral hydrogen at a radius of 2 kpc). Comparing the fluxes in Figure 3.6 reveals that the input spectra differ mostly between the ionization potential of  $\text{O}^+$  and the ionization edge of  $\text{He}^+$ . Therefore the ionization structure in Figure 4.1 both of  $\text{S}^+$  and  $\text{S}^{++}$  are nearly the same for all models whereas strong deviations are visible for the ionization structure of  $\text{N}^+$ ,  $\text{N}^{++}$ ,  $\text{C}^+$ ,  $\text{C}^{++}$ ,  $\text{O}^+$ , and most prominent  $\text{O}^{++}$ . The CoStar models exhibit the highest amount of highly ionized species most visible in the higher amounts of  $\text{O}^{++}$  and  $\text{He}^+$  in comparison to the other models therefore having the hardest

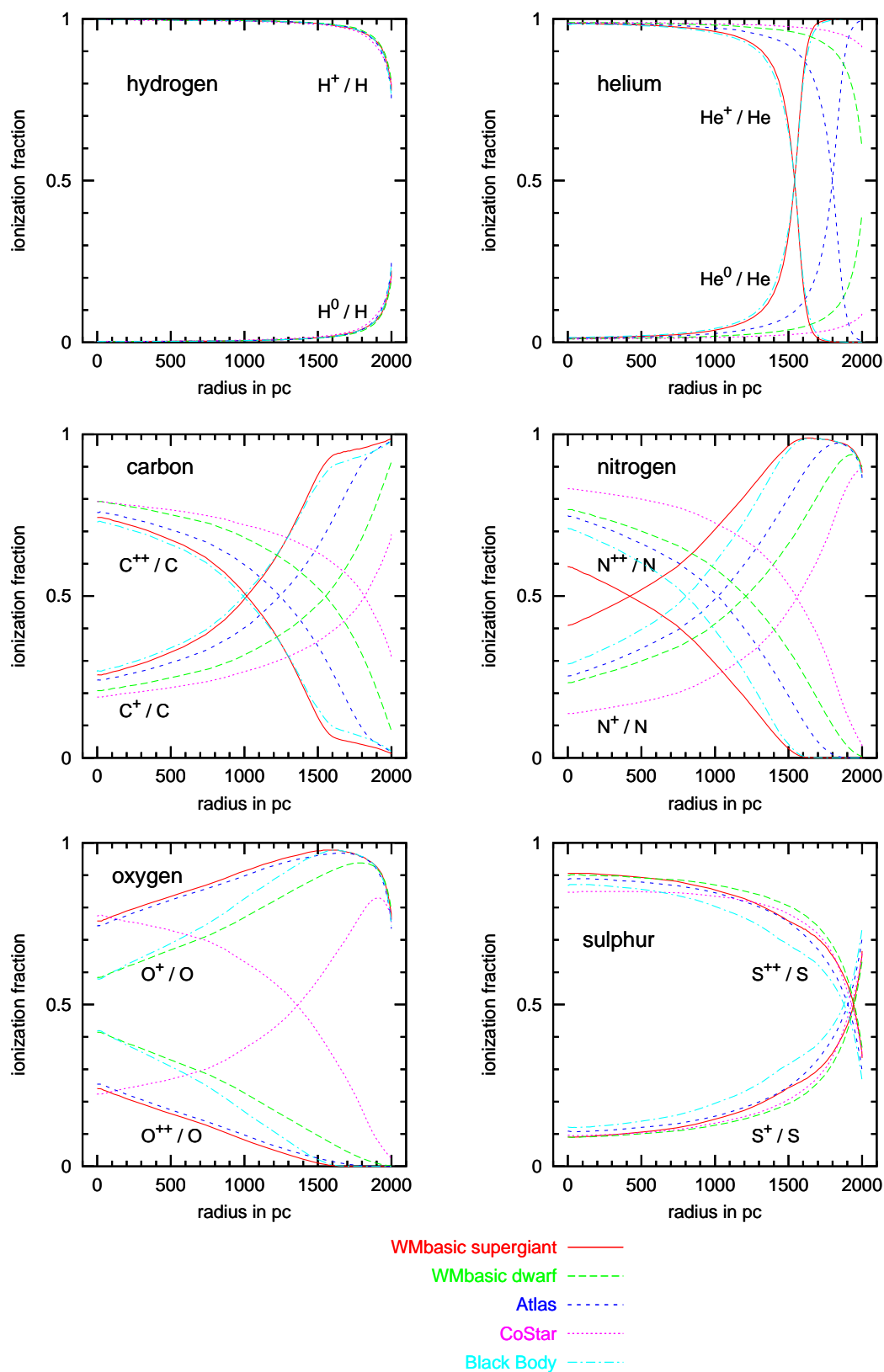


Figure 4.1: Ionization fraction for different ions, scale height  $h = 2.5$  kpc and different input spectra

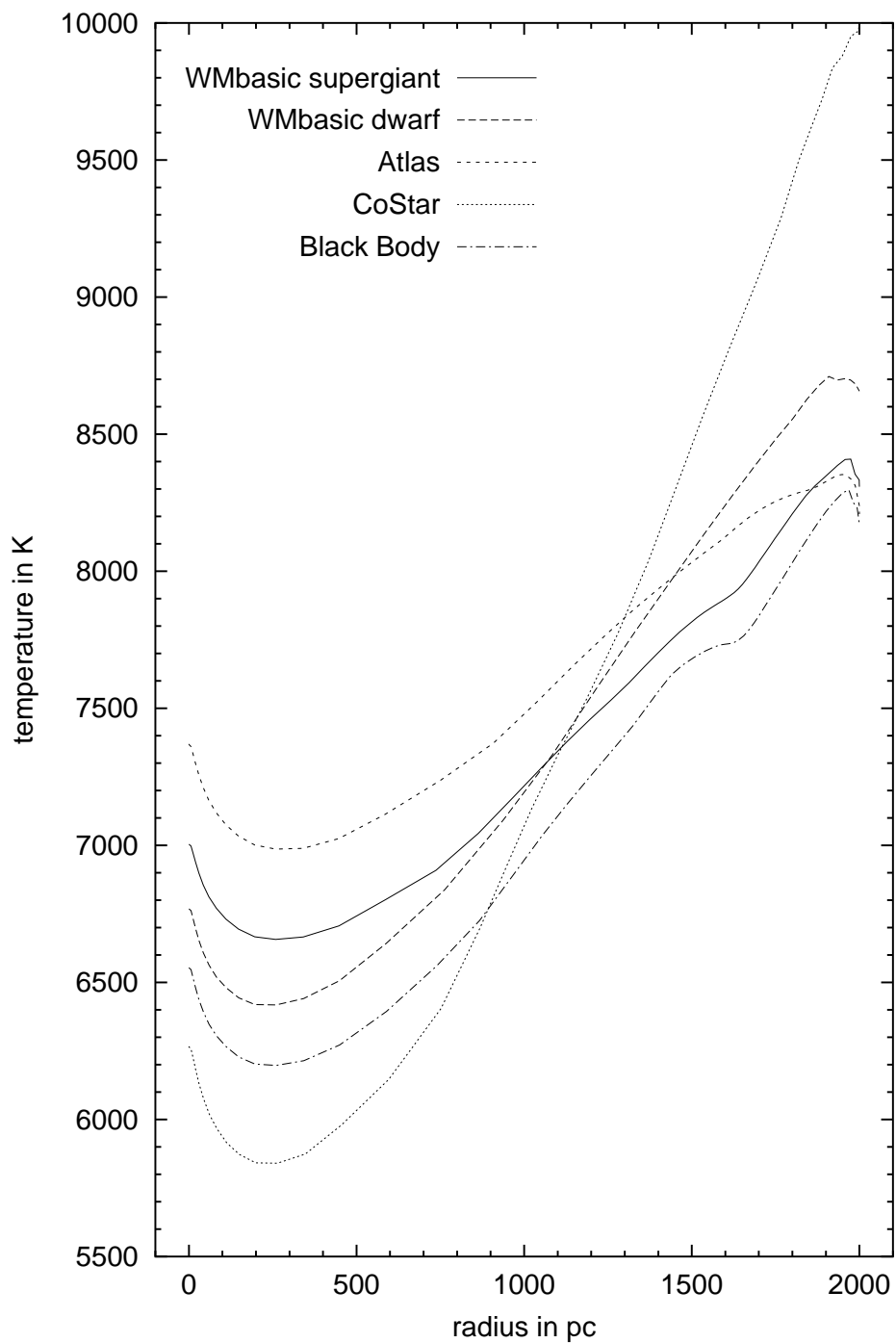


Figure 4.2: Gas temperatures for the subgroup with  $h = 2.5$  kpc and different input spectra

spectrum. The WMbasic dwarf spectrum exhibits likewise a harder spectrum than the WMbasic supergiant spectrum as is also seen in Figure 3.6 and Table 3.2. The ionization balance of oxygen is dominated by the flux between 350 Å and 220 Å. It is clear that the different stellar atmosphere models will have a significant influence on [OIII] and less on the other. Figure 4.1 shows that there are also big differences in the singly and doubly ionized carbon ions for the different input spectra, this will have an important impact on the relevant cooling line [CII] $\lambda$ 157 $\mu$ m. Unfortunately no spectroscopic observations with enough sensitivity and resolution of this IR fine-structure line exist up to now.

The gas temperature in Figure 4.2 exhibits a local minimum at around 200 pc for all models followed by a continuous increase to the maximal temperature at the edge of the simulated region. This increase is due to the hardening of the residual stellar radiation field as soft photons near the ionization thresholds are progressively absorbed. It is therefore likely that the first 200 pc act as a transition zone for the gas layer to respond to the ionizing radiation. This depression is both seen in the run of the modeled [OII]/H $\alpha$  line ratio and in the observed one, most clearly in NGC 891 (see Figure 2.6). This is of great importance as [OII] is the main cooling line of the DIG. The slope of the temperature rise is clearly another indicator for the hardness of the input spectrum as the CoStar model shows the steepest gradient.

## 4.4 Stellar input spectra

### 4.4.1 $h = 0.6$ kpc: NGC 4302, UGC 10288

Figure 4.3 shows the course of the line ratios for the subgroup with  $h = 0.6$  kpc. The Black Body, Atlas, and WMbasic (both dwarf and supergiant) can explain the line ratios of [NII]/H $\alpha$  and [SII]/H $\alpha$ , although UGC 10288 shows in some cases higher values for [SII]/H $\alpha$  after about 1 kpc, but these measurements have also larger errors. The CoStar model overestimates the ratio [NII]/H $\alpha$  after  $|z| = 500$  pc.

However only this model can explain [OIII]/H $\alpha$  within the first 1 kpc, then the observations indicate a further rise whereas CoStar shows a decline. All other models fall short as they predict far too low [OIII]/H $\alpha$  ratios.

All models have difficulties in producing high enough [OI]/H $\alpha$  ratios as are observed throughout the first 800 pc. There are not enough neutral oxygen atoms until  $|z| = 800$  pc that can be excited as nearly all oxygen atoms are singly or doubly ionized. The gradient in [OI]/H $\alpha$  of the CoStar model is too steep as this ratio is overestimated after  $|z| = 1$  kpc and has too low values before  $|z| \sim 800$  pc.

On the one hand there are no measurements of [OII]/H $\alpha$  or HeI/H $\alpha$  for these galaxies. On the other hand it is noticeable that the difference between the models for HeI/H $\alpha$  after  $|z| = 500$  pc is largest for this subgroup. It would therefore be very valuable for the distinction between the models to have observations of this emission line especially more distant from the midplane than 500 pc. The [OII]/H $\alpha$  ratio in contrast could not clearly distinguish between the WMbasic supergiant, Atlas, and Black Body model for this subgroup.

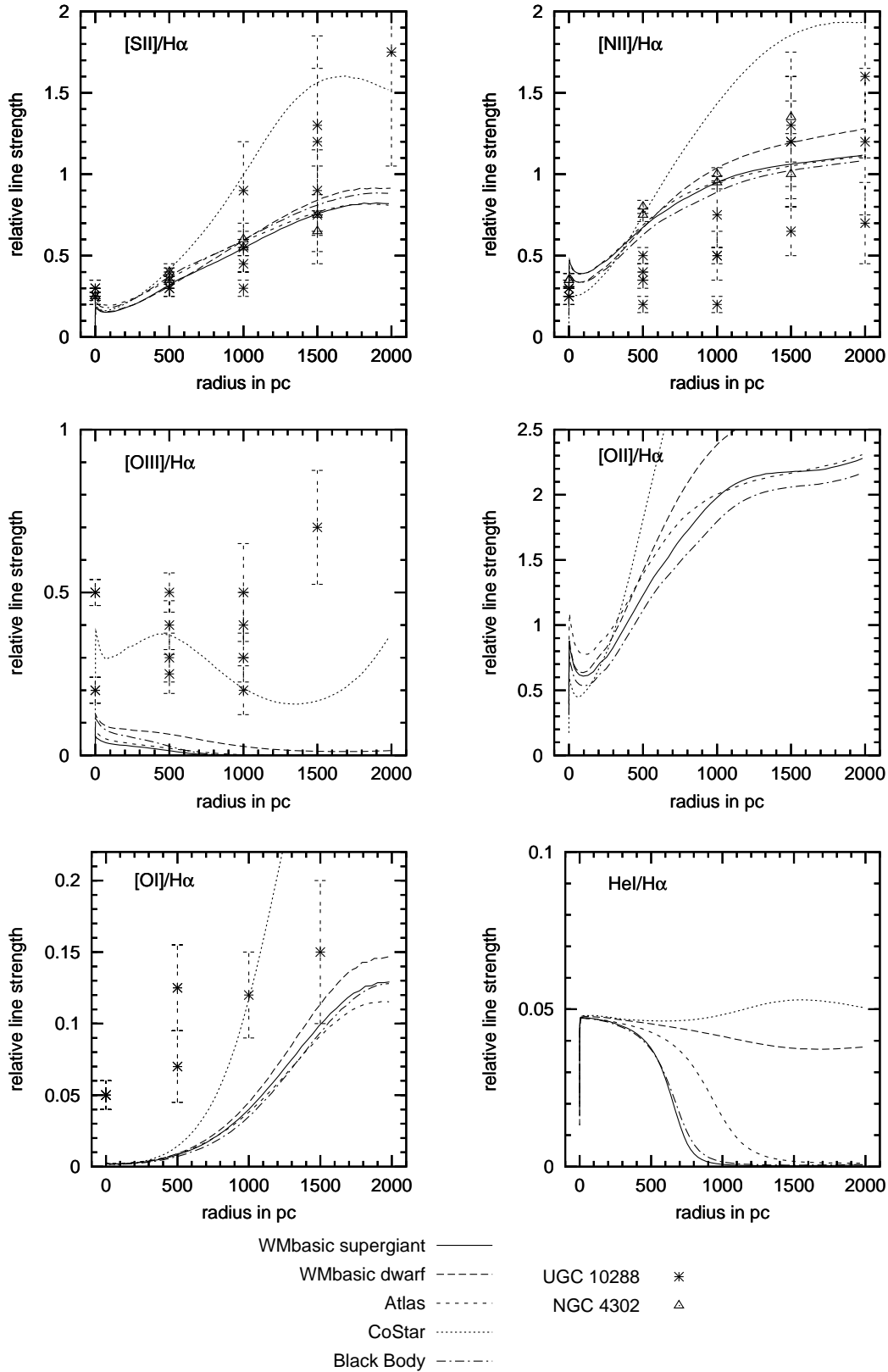


Figure 4.3: Effect of different stellar atmosphere models on the subgroup with  $h = 0.6$  kpc, effective stellar temperature 40,000 K

#### 4.4.2 $h = 1$ kpc: NGC 1963, NGC 3044, NGC 4634, NGC 4631, NGC 3079

Figure 4.4 exhibits the course of the line ratios for the subgroup with  $h = 1$  kpc. All models are able to reproduce the observed line ratios of  $[\text{NII}]/\text{H}\alpha$  and  $[\text{SII}]/\text{H}\alpha$  regarding the errors, although the CoStar model overestimates the nitrogen line after  $|z| = 1$  kpc. From  $|z| \sim 0.5$  kpc to 1.5 kpc it is remarkable that the bulk of the observed data points are above the models for  $[\text{SII}]/\text{H}\alpha$  and below for  $[\text{NII}]/\text{H}\alpha$ .

The modeled  $[\text{OIII}]/\text{H}\alpha$  again decreases with increasing  $|z|$  as in the other scale height groups, whereas the observations have the opposite trend. On the one hand the Black Body, Atlas, and both WMbasic models show the appropriate  $[\text{OIII}]/\text{H}\alpha$  ratio for the first 500 pc, then they fall short. The CoStar model on the other hand has higher values and only after 1.5 kpc it is approaching the range of the observations but with the opposite trend.

The line ratio  $[\text{OII}]/\text{H}\alpha$  is well reproduced with the WMbasic supergiant, Atlas, and Black Body model, only values higher than 1 for  $|z| < 500$  pc are not covered by the models. The CoStar and WMbasic dwarf model show a steeper gradient than observed, they underestimate this line ratio before 500 pc and overproduce it after 1 kpc.

The ratio of  $[\text{OI}]/\text{H}\alpha$  is only fairly reproduced by the CoStar model after  $|z| = 1$  kpc. The other models are not able to produce as high  $[\text{OI}]/\text{H}\alpha$  ratios as observed, they show values of this line ratio larger than 0.05 not until a height of 1.5 kpc where no data points are available.

The  $\text{HeI}/\text{H}\alpha$  ratio is well reproduced by all models, the data show after  $|z| = 1$  kpc a larger spread and the errors become very large. The Black Body and WMbasic supergiant models have a sharp decline after 1 kpc and cannot explain the high and very uncertain  $\text{HeI}/\text{H}\alpha$  ratio thereafter.

#### 4.4.3 $h = 1$ kpc: Perseus Arm

Figure 4.5 exhibits the result of the models for the Perseus Arm, only  $[\text{SII}]$ ,  $[\text{NII}]$ , and  $\text{H}\alpha$  data are available for this object. In comparison to the other galaxies in this subgroup the observed line ratios of  $[\text{SII}]/\text{H}\alpha$  and  $[\text{NII}]/\text{H}\alpha$  are higher especially for higher  $|z|$  heights. This is likely to be a geometric effect as the sight line integration (see Figure 3.5) shows that  $[\text{SII}]/\text{H}\alpha$  gets considerably enhanced if this effect is been taken into account. The impact upon  $[\text{NII}]/\text{H}\alpha$  is smaller (except CoStar) as compared with Figure 4.4 as all models except CoStar do never produce  $[\text{NII}]/\text{H}\alpha$  larger than 1. Therefore the enhancement is altogether not strong enough to elevate this ratio as required.

The CoStar model overestimates the  $[\text{SII}]/\text{H}\alpha$  line ratio after 1 kpc, all other models have smaller values that are though tolerable due to the error of the data. The high  $[\text{NII}]/\text{H}\alpha$  values after 1 kpc can only be reproduced by the CoStar model but the other models can in contrast reproduce the line ratio up to 1 kpc. This means that only a harder input spectrum is able to produce  $[\text{NII}]/\text{H}\alpha > 1$ .

The effect of the sight line integration has furthermore the most visible effect of enhancing



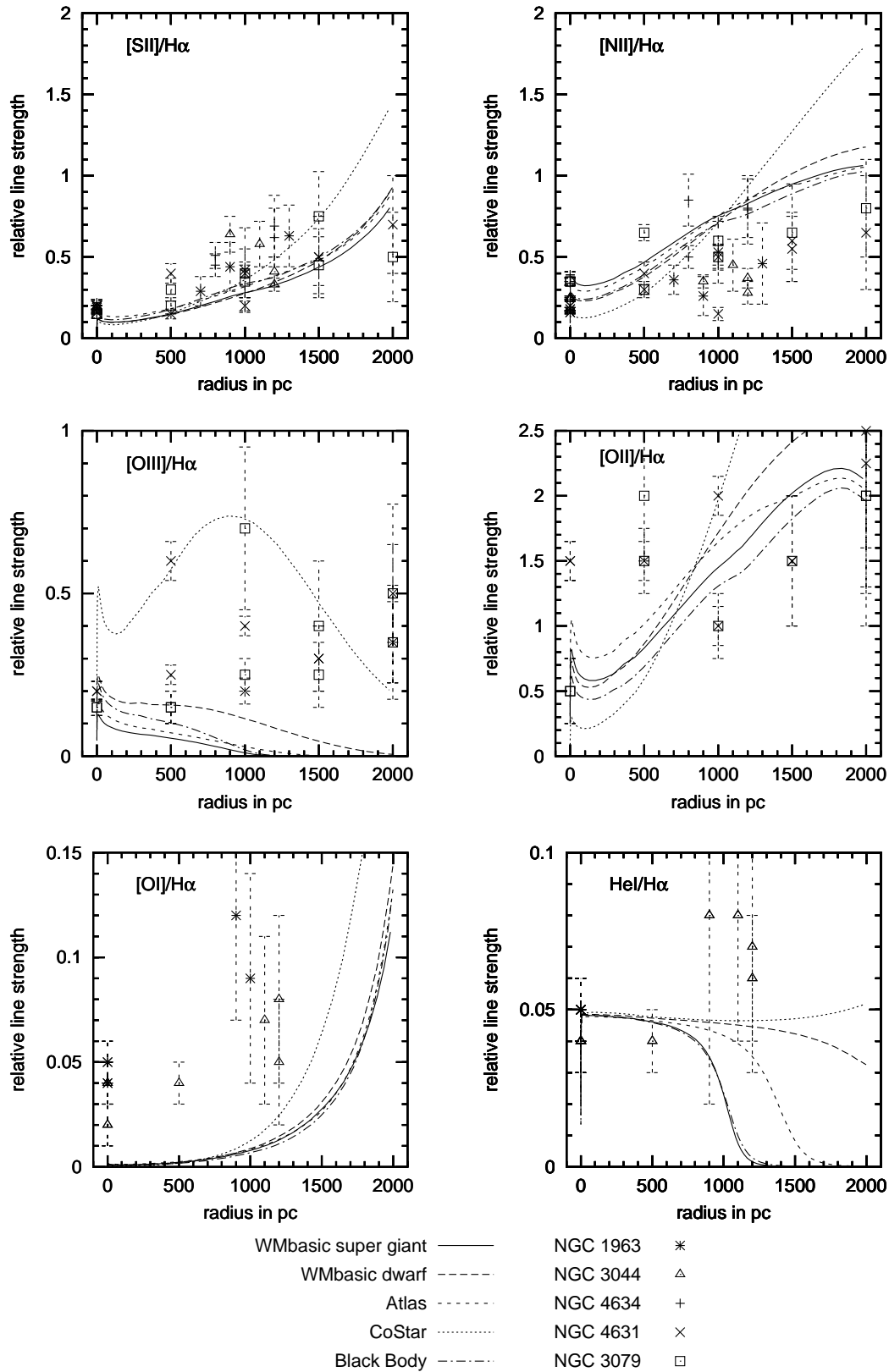


Figure 4.4: Effect of different stellar atmosphere models on the subgroup with  $h = 1$  kpc, effective stellar temperature 40,000 K

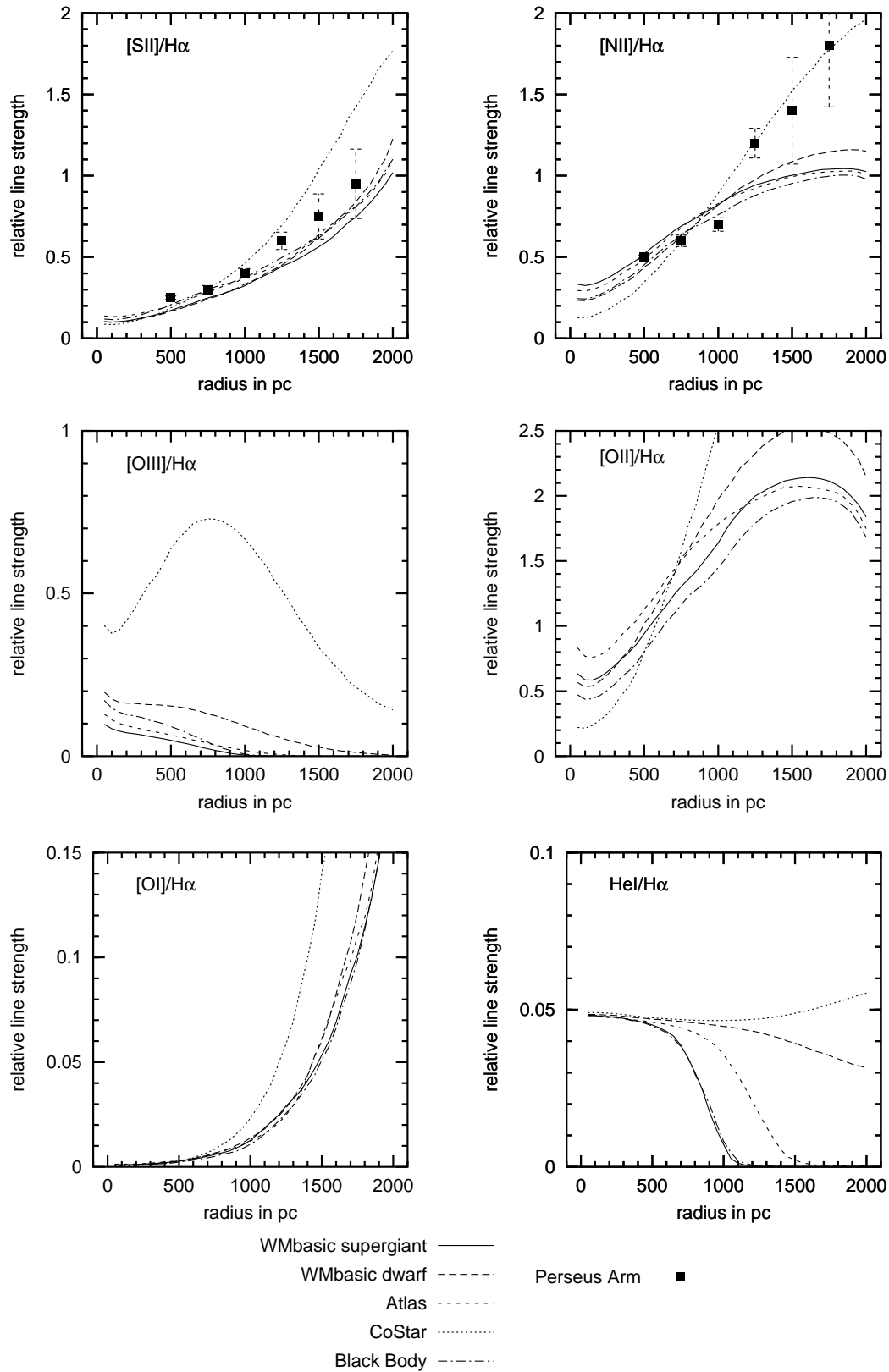


Figure 4.5: *Effect of different stellar atmosphere models on the model for the Perseus Arm, effective stellar temperature 40,000 K*

the [OI]/H $\alpha$  ratio at lower  $|z|$  heights. The [OII]/H $\alpha$  ratio clearly shows the influence of the Strömgren Sphere in decreasing values after  $|z| > 1.5$  kpc.

It is therefore most desirable to have additional observations, at least of the main cooling line [OII] but also of other ionization stages of oxygen as probed by [OI] and [OIII].

#### 4.4.4 $h = 2.5$ kpc: NGC 891

Figure 4.6 shows the variations of the line ratios for the subgroup with  $h = 2.5$  kpc. All models predict lower line ratios of [SII]/H $\alpha$  and [NII]/H $\alpha$  than observed, but after 1.5 kpc this gap gets smaller as more singly ionized sulphur and nitrogen is produced nearer the edge of the Strömgren Sphere. The models can at last reproduce the measurements reaching the end of the calculation at  $|z| = 2$  kpc.

The opposite trend in [OIII]/H $\alpha$  between the observations and the model predictions is clearly visible, for this subgroup all models overestimate [OIII] near the midplane, though for  $1 \text{ kpc} \leq |z| \leq 1.5 \text{ kpc}$  all models except CoStar reproduce [OIII]/H $\alpha$ . The CoStar models shows far too high values reaching up to one whereas only values of up to 0.4 are observed.

The ratio [OII]/H $\alpha$  is well reproduced by all models except CoStar whose gradient is too steep, it has only the appropriate value for  $|z| = 1.5$  kpc. The first two measured points at  $|z| = 0$  and 500 pc that are higher than 1 are not covered by all models. Whereas the following gradient of the data points is in very good accordance with the models except CoStar.

The steep increase of the modeled [OI]/H $\alpha$  after 1.5 kpc is due to a rising amount of neutral oxygen (see Figure 4.1 for the ionization structure). The high [OI]/H $\alpha$  ratio for all  $|z|$  heights are nevertheless not reproduced by any model as the observations show very high values even for small  $|z|$ .

The observed HeI/H $\alpha$  ratio is smaller for  $|z| < 1$  kpc than the predicted but is matched by all models for  $|z| = 1.5$  kpc. Due to the similarity of the models in this ratio the data can make no distinction between them.

## 4.5 Stellar temperatures

In order to expand the parameter space this subsection is addressing the effect of different effective stellar temperatures using only the standard model and concentrating on a scale height of 1 kpc.

The effective temperature is varied between 50,000 K and 30,000 K in steps of 5,000 K. Figure 4.7 shows that the models cover a similar region regarding the values of the emission lines as the models with varying stellar atmosphere model (see Figure 4.4) except for the lowest temperature of 30,000 K. The [SII]/H $\alpha$  and [OI]/H $\alpha$  ratios are only varying in a relative narrow range, only the hottest effective temperature has higher deviations for distances larger than 1 kpc from the midplane. [NII]/H $\alpha$  presents larger deviations although at the end of the modeled region the models have nearly all the same value ( $\sim 1$ ),

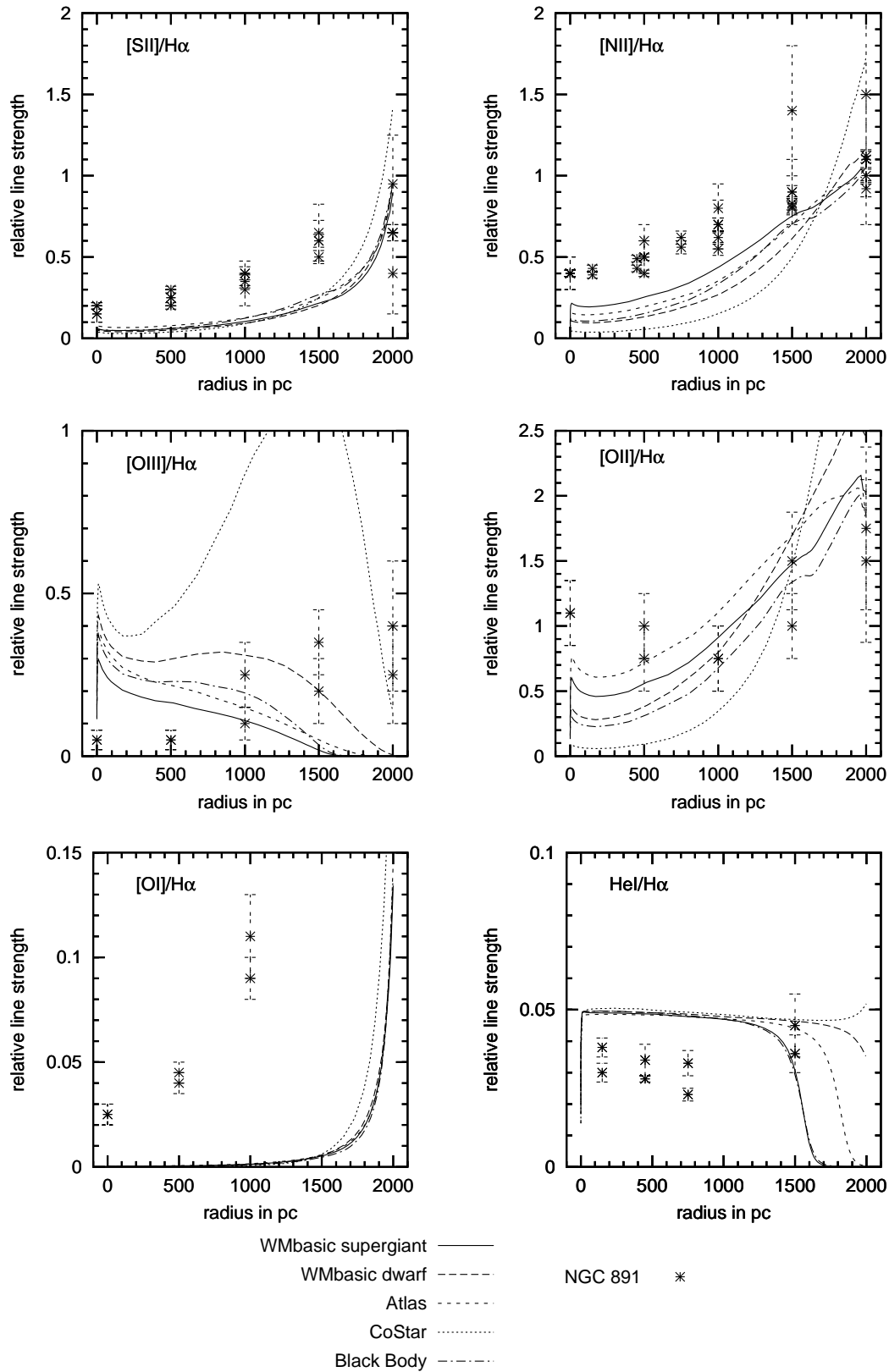


Figure 4.6: Effect of different stellar atmosphere models on the subgroup with  $h = 2.5$  kpc, effective stellar temperature 40,000 K

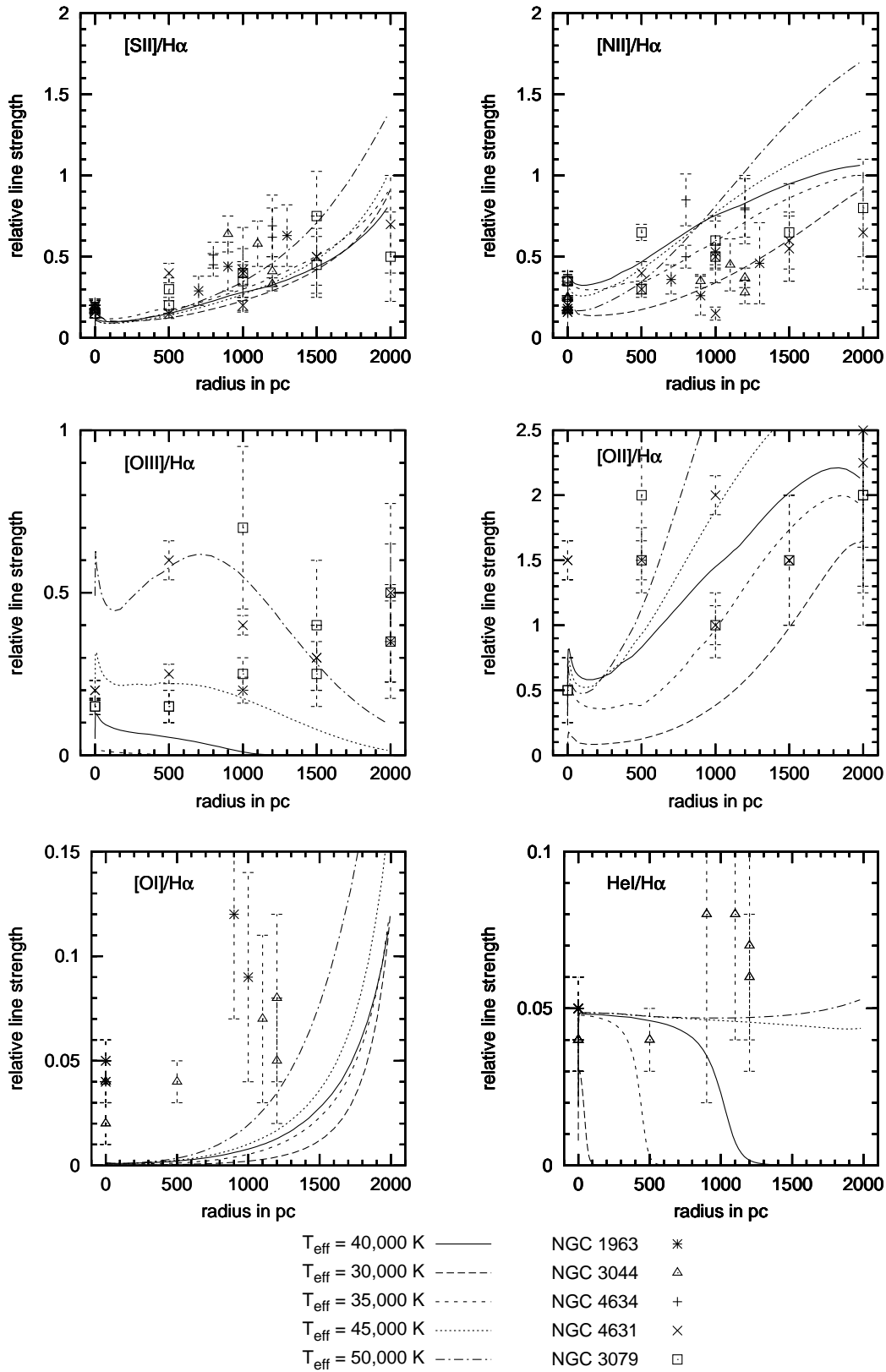


Figure 4.7: Effect of different stellar effective temperatures, on the subgroup with  $h = 1 \text{ kpc}$ , stellar model: WMbasic, supergiant

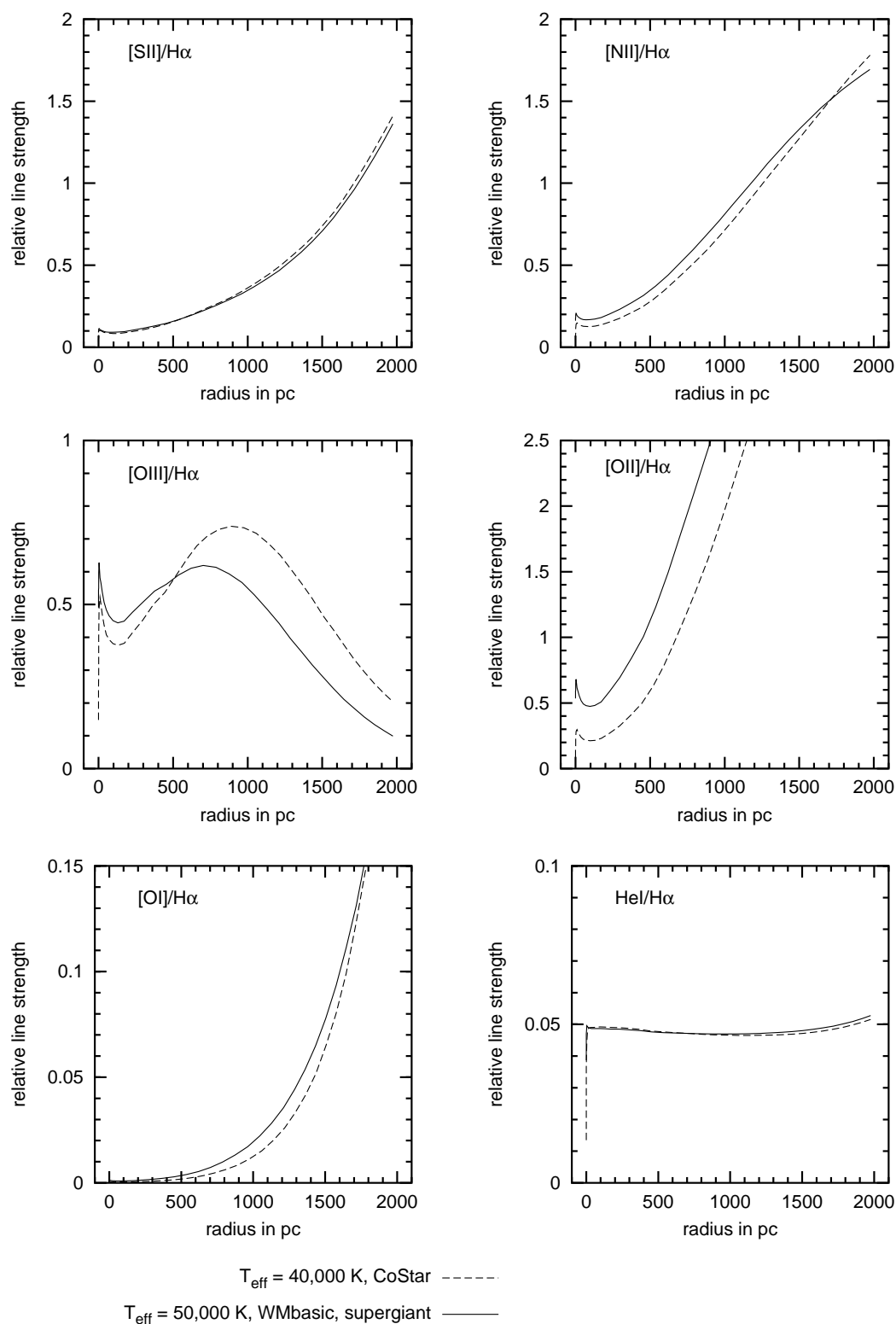


Figure 4.8: Difference between the models with WMbasic supergiant,  $T_{\text{eff}} = 50,000$  K and CoStar with  $T_{\text{eff}} = 40,000$  K

only the hardest input spectrum with the highest temperature can produce  $[\text{NII}]/\text{H}\alpha$  as high as 1.7. The low observed values of  $[\text{NII}]/\text{H}\alpha$  between  $|z| = 500$  pc and 1500 pc are reproduced by the models with effective stellar temperatures of 30,000 K and 35,000 K. However these models are neither able to produce enough  $[\text{OII}]$  and  $[\text{OIII}]$  nor HeI emission after a  $|z|$  height of 500 pc as required by the observations. The ratio  $[\text{OII}]/\text{H}\alpha$  is a good characteristic for discriminating between the models as for this ratio all models separate most clearly and they show the same tendency as the data.  $[\text{OII}]/\text{H}\alpha$  favors the standard model showing its significance.

Figure 4.8 compares the model with  $T_{\text{eff}} = 50,000$  K and the CoStar model from Figure 4.4 showing that they have nearly the same effect (for clarity the data points are not plotted). These two models predict namely nearly the same run of  $[\text{SII}]/\text{H}\alpha$ ,  $[\text{NII}]/\text{H}\alpha$ ,  $[\text{OI}]/\text{H}\alpha$ , and  $\text{HeI}/\text{H}\alpha$ . The ratios  $[\text{OII}]/\text{H}\alpha$  and  $[\text{OIII}]/\text{H}\alpha$  show little and insignificant deviations. The higher  $[\text{OIII}]/\text{H}\alpha$  and lower  $[\text{OII}]/\text{H}\alpha$  ratios indicate that the CoStar model has a harder spectral energy distribution. The recombination line HeI is not an indicator for this distinction as the models predict nearly the same line ratio run for both cases.

It is however very unlikely that stars with effective temperatures as high as 50,000 K are dominating the global heating–cooling equilibrium of the DIG because they are very rare and have a very short life time. Their dominance is additionally ruled out by the main cooling line  $[\text{OII}]$ , which they overproduce after  $|z| \approx 700$  pc.

## 4.6 Stellar remnant sources

Although OB stars provide the main part of ionizing photons stellar remnant sources such as WD or PN are present and it is important to estimate their influence. Following Bregman & Harrington (1986) the total hydrogen ionizing photon flux of these sources combined is approximately 1/100 of that of the O stars. Their spectrum can be simulated by a Black Body with an effective temperature of 70,000 K. They dominate the UV–flux in the wavelength range between 228 Å and 276 Å. Another model was run where the flux of the Black Body spectrum was 1/10 of that of the O stars in order to study the effect of a much harder input spectrum on the line ratios. The numbers given by Bregman & Harrington certainly have to be checked anew, although it is very likely that the assumed hydrogen ionizing photon flux of the remnants sources of 1/10 of the O stars (for the second case) acts as an upper limit for the Milky Way.

The influence of the stellar remnant sources is examined in Figure 4.9. The gas is illuminated by the two ionizing sources, the spectra are superimposed. The WMbasic supergiant spectrum and a Black Body spectrum with  $T_{\text{eff}} = 70,000$  K is chosen, the scale height is 1 kpc, the other parameters are the standard ones. The standard model is also shown, but no data points as primarily the comparison between the models is of concern here.

Figure 4.9 displays the run of the six line ratios of the three models. There are only small deviations between the standard model and that one where the Black Body flux has a strength of 1/100 of the other spectrum. The effect of the second ionizing source is clearly negligible. The largest deviations are seen in  $[\text{OIII}]/\text{H}\alpha$  and  $\text{HeI}/\text{H}\alpha$  but they are of no

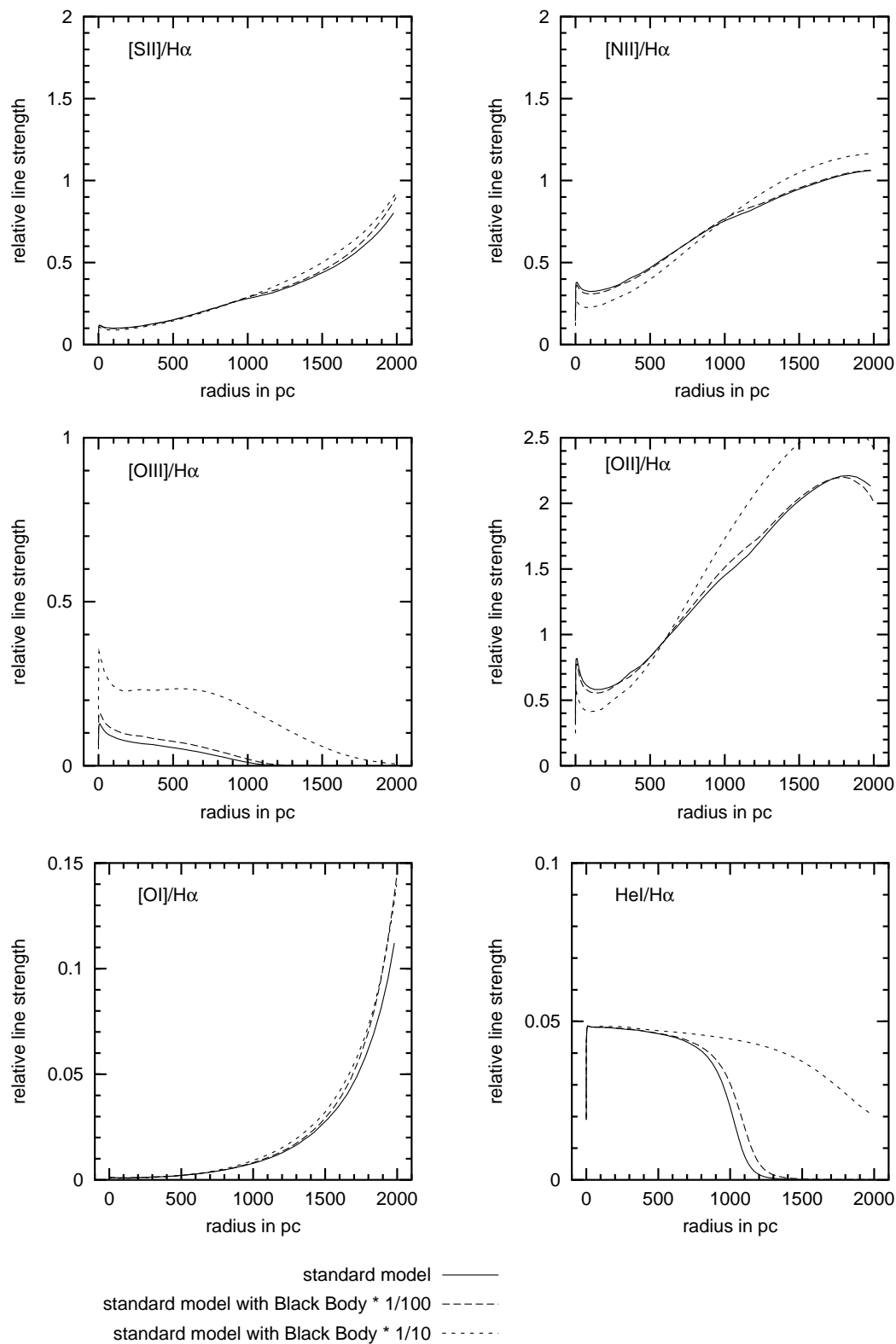


Figure 4.9: *Effect of a second ionizing source with a harder input spectrum and two different fluxes*



significance further. However these differences show that the combined model has indeed a harder input spectrum than the standard one. The comparison with the third model where the flux of the Black Body is 1/10 of the WMbasic supergiant spectrum reveals that the difference in  $[\text{SII}]/\text{H}\alpha$ ,  $[\text{NII}]/\text{H}\alpha$ , and  $[\text{OI}]/\text{H}\alpha$  is small enough to be negligible.  $[\text{OIII}]/\text{H}\alpha$  has higher values but still the trend is opposite to the observations. The increased  $\Phi_{\text{H}\alpha}$  has the clear effect of producing enhanced HeI emission at higher  $|z|$  heights.

It is therefore appropriate to neglect the stellar remnant sources in the further discussion and state that their influence is too small being of importance. They are thus also no viable candidates for extra heating sources as discussed in the next section.

## 4.7 Extra heating source

In order to explain the line ratios in the DIG several authors (e.g. Collins & Rand 2001, Otte et al. 2001, Mathis 2000, Reynolds et al. 1999, Reynolds & Cox 1992) proposed the existence of an extra heating source. The observed line ratios in the DIG, in particular  $[\text{SII}]/\text{H}\alpha$  and  $[\text{NII}]/\text{H}\alpha$ , are elevated compared to classical HII regions. The extra heating source has hence to fulfill specific requirements: the plasma has to respond to the extra heating with a higher electron temperature and at the same time the ionization structure should not change. As the main coolants of the DIG are the forbidden emission lines which are collisionally excited the increase in electron temperature rises the probability that the levels get excited. This could also be accomplished by a higher ionizing photon flux, but this would lead to a depletion of the lower ionization levels in favor for higher ionized ions which would weaken in turn the forbidden emission lines. Therefore the ionization structure must remain the same if the extra heating source is ‘turned on’.

Figure 4.10 shows the effect of a constant volume extra heating term added to the heating-cooling balance equation (3.8) on the model predictions for the specific case of the Perseus Arm. The heating rates are  $1 \times 10^{-27}$  and  $1 \times 10^{-26}$  erg cm<sup>-3</sup> s<sup>-1</sup>, the input spectrum is the WMbasic supergiant model. The heating rates have the same order of magnitude as the ones used in Reynolds et al. (1999). The authors state these rates for turbulent dissipation and magnetic field reconnection but argue that other mechanisms such as grain heating could also provide enough extra heating. In fact Reynolds & Cox (1992) state that grain heating alone could equal or even exceed photoionization heating in the DIG.

The line ratios  $[\text{SII}]/\text{H}\alpha$  and  $[\text{NII}]/\text{H}\alpha$  are elevated with increasing heating rate, the temperature is rising and the ionization structure is unchanged as demanded. With increasing heating rate it is possible to reproduce the observed line ratios of the Perseus Arm choosing a rate between  $1 \times 10^{-27}$  erg cm<sup>-3</sup> s<sup>-1</sup> and  $1 \times 10^{-26}$  erg cm<sup>-3</sup> s<sup>-1</sup>. The models are also able to reproduce the determined temperature run in the Perseus Arm by Reynolds et al. (1999). The authors deduce the temperature from the  $[\text{NII}]/\text{H}\alpha$  ratio assuming constant ionization fractions and  $\text{N}^+/\text{N} \approx \text{H}^+/\text{H}$ . This last point is only valid for  $|z| \approx 1$  kpc in the models (see Figure 4.10), for distances smaller than that  $\text{N}^+/\text{N} < \text{H}^+/\text{H}$  and thereafter  $\text{N}^+/\text{N} > \text{H}^+/\text{H}$ . The ionization fractions are moreover strongly dependent on the distance from the ionizing source, thus the deduced temperatures have to be handled with care.

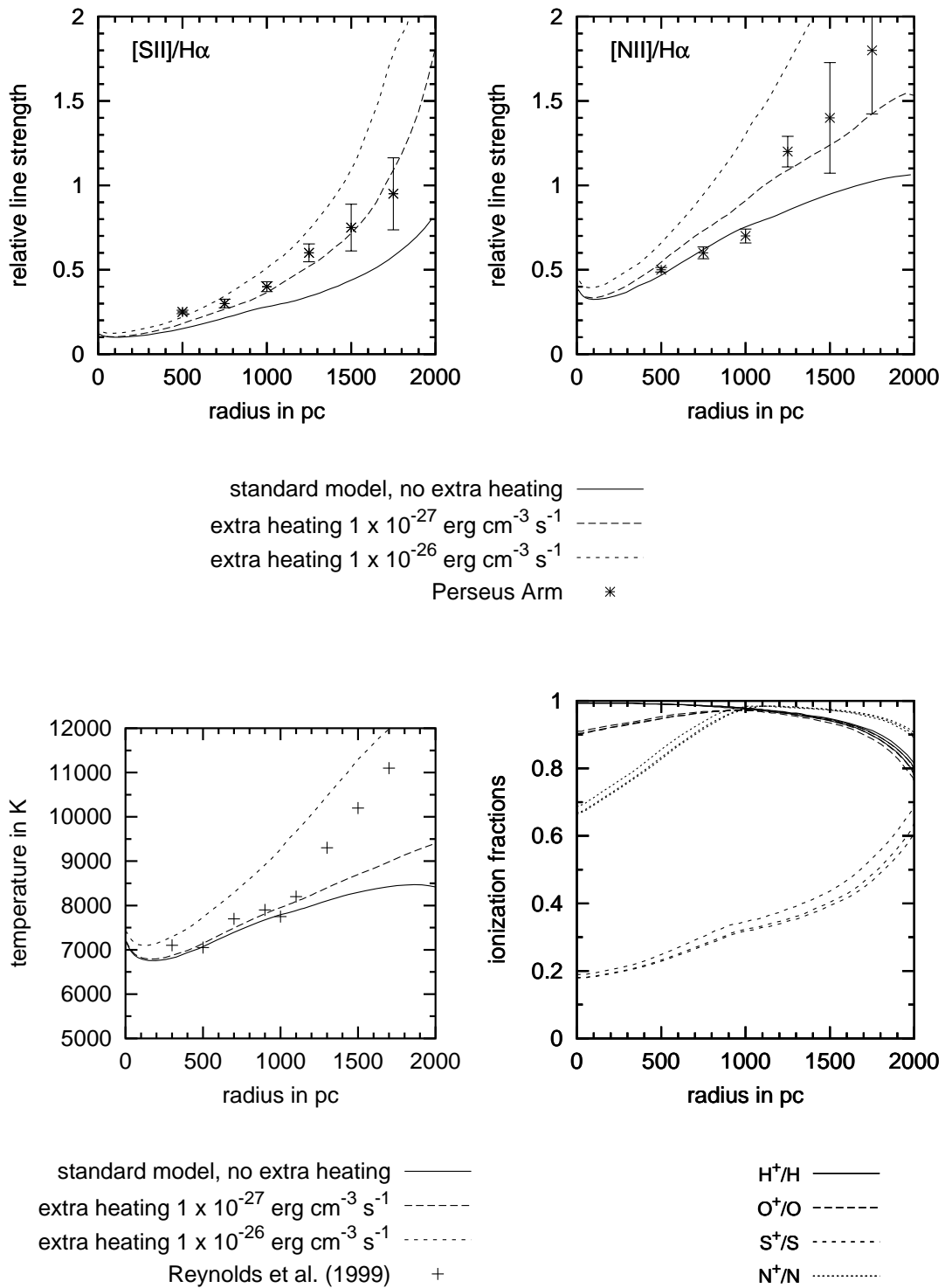


Figure 4.10: *Effect of a constant volume extra heating rate for the model predictions for the Perseus Arm*

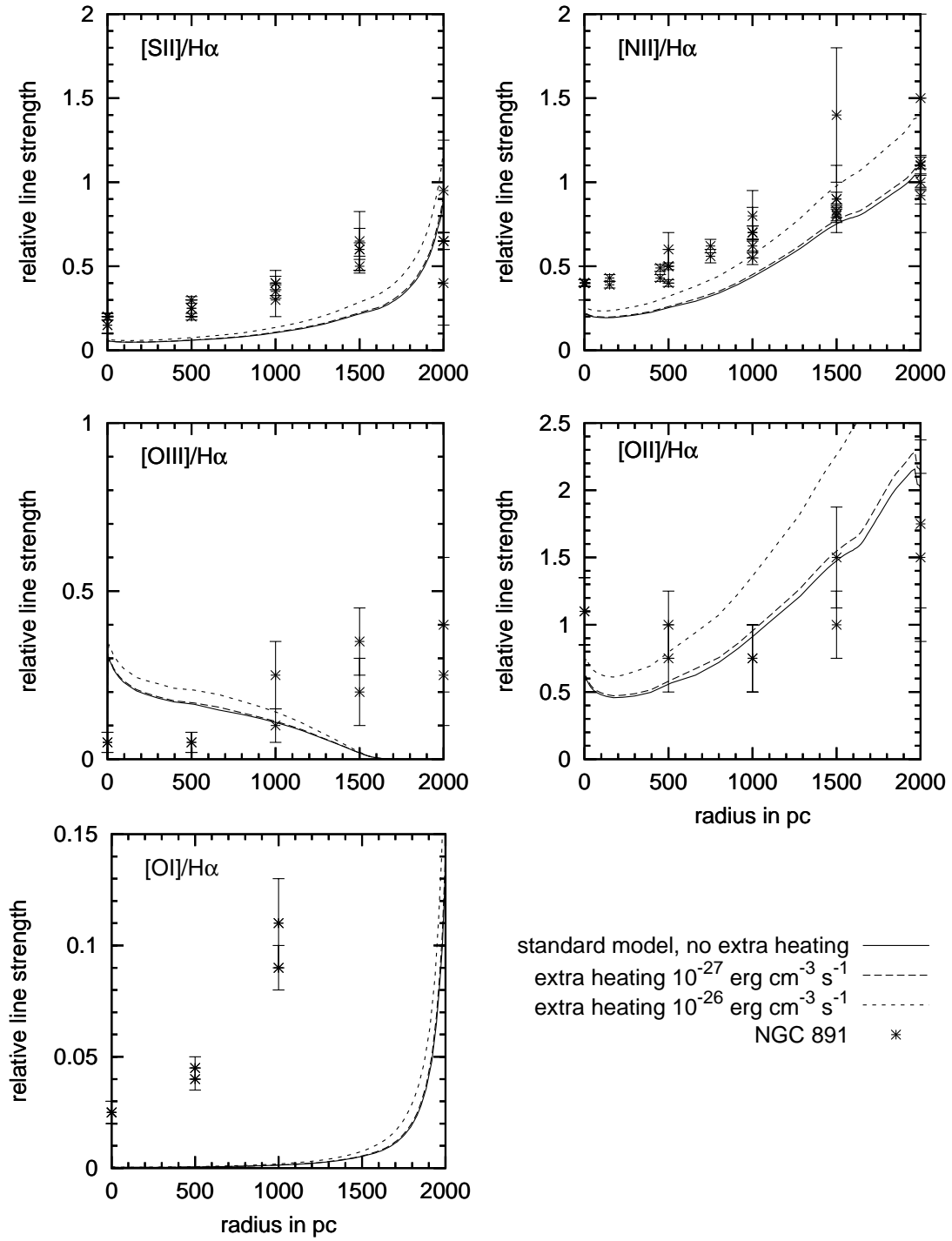


Figure 4.11: Effect of a constant volume extra heating rate for the model predictions for the subgroup with  $h = 2.5$  kpc

Figure 4.11 displays the effect on the subgroup with  $h = 2.5$  kpc, it is evident that the elevation in this case is not sufficient to explain the observed line ratios of  $[\text{SII}]/\text{H}\alpha$ ,  $[\text{OIII}]/\text{H}\alpha$ , and  $[\text{OI}]/\text{H}\alpha$ . Moreover the model with a heating rate of  $1 \times 10^{-26}$  erg cm $^{-3}$  s $^{-1}$  overestimates the line ratio  $[\text{OII}]/\text{H}\alpha$  so that this line ratio really gives an upper limit for the extra heating term, only  $[\text{NII}]/\text{H}\alpha$  is fairly reproduced. The constraint of the  $[\text{OII}]/\text{H}\alpha$  line ratio is severe as  $[\text{OII}]$  is the main cooling line. The effect of the extra heating is smaller for this subgroup than for  $h = 1$  kpc as the ionization parameter  $U_{r_0}$  (see Table 4.1) is highest for the subgroup with  $h = 2.5$  kpc which means that the UV-photon flux is highest and the influence of an extra heating therefore diminished.

So far the inclusion of an extra heating rate seems to be insufficient for the reproduction of the line ratios  $[\text{SII}]/\text{H}\alpha$  and  $[\text{NII}]/\text{H}\alpha$  for the subgroup with a scale height of 2.5 kpc.  $[\text{OIII}]/\text{H}\alpha$  and  $[\text{OI}]/\text{H}\alpha$  cannot be explained by this method because the ionization structure should be changed to produce more doubly ionized oxygen at higher distances from the midplane and neutral oxygen near it. In the actual models the  $[\text{OIII}]/\text{H}\alpha$  ratio vanishes after  $\sim 1.5$  kpc as there are almost no  $\text{O}^{++}$  ions left that can be excited.

## 4.8 Metallicity indicator?

The course of the slope of the data in the  $[\text{SII}]/\text{H}\alpha$ – $[\text{NII}]/\text{H}\alpha$ –diagram is a matter of debate as different galaxies show different slopes, as displayed in Figure 4.12. NGC 3044 has clearly a steeper gradient than NGC 4634. Higher ratios in this plot are at the same time indications for higher  $|z|$  heights, as  $[\text{SII}]/\text{H}\alpha$  and  $[\text{NII}]/\text{H}\alpha$  are both increasing with rising distance from the midplane. The assumption so far discussed (Tüllmann & Dettmar 2000a, Haffner et al. 1999) is that different global metallicities are the reason for various slopes. The term metallicity denotes the content of all metals<sup>1</sup> in the gas, the models use the ISM abundance of CLOUDY with S/H and N/H additionally set (see chapter 3.4).

The CLOUDY models show clear evidence that there must be another reason for the different slopes as the metallicity dependence of the forbidden lines create other effects than changing it. Figure 4.13 exhibits the variation in the ratio  $[\text{SII}]/[\text{NII}]$  for different metallicities, the solid line denotes the original metallicity, the two dashed lines represent models with metallicities reduced by a factor of 10 and 100. The slope  $[\text{SII}]/[\text{NII}]$  is very little effected by the huge change of two order of magnitude in metallicity.

The efficiency of cooling is proportional to the amount of heavy ions so that the temperature will increase with smaller metallicity. The line ratios will only be elevated if the depletion of the ions is more than balanced by the effect of higher temperature, otherwise the line ratios will decline. This is the case as shown in Figure 4.14 with metallicities diminished by a factor of 2 and 10. For the DIG a lower metallicity has the effect of confining the ratios to lower absolute values as the abundance of ions are getting smaller, at the same time the slope of the ratio stays the same.

---

<sup>1</sup>the notion 'metal' is used for all elements with a higher atomic number than helium

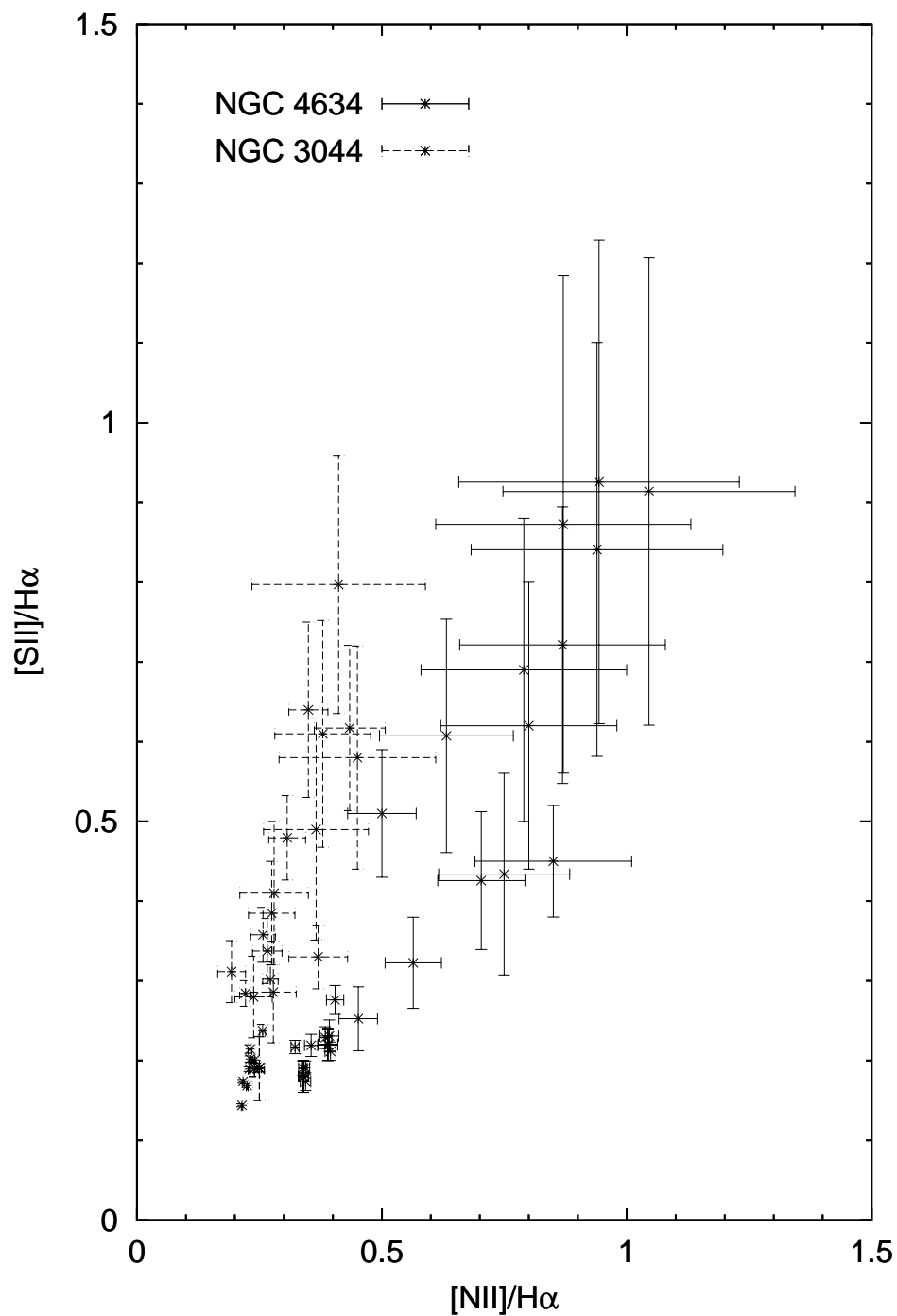


Figure 4.12: Data of the galaxies NGC 3044 and NGC 4634

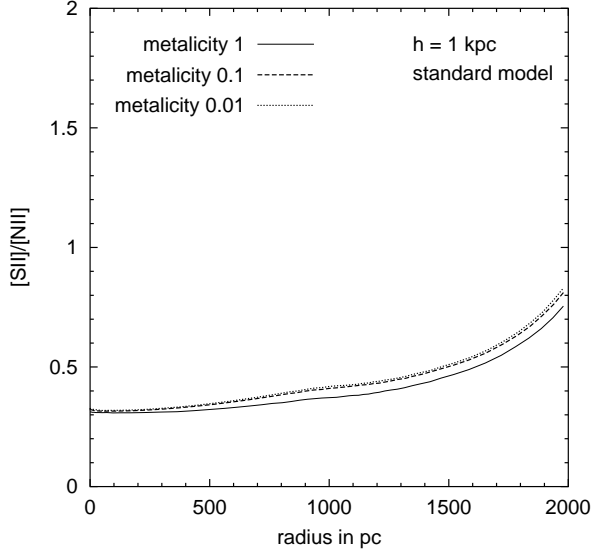


Figure 4.13: Slope in the  $[SII]$ – $[NII]$  diagram for models with different metallicities

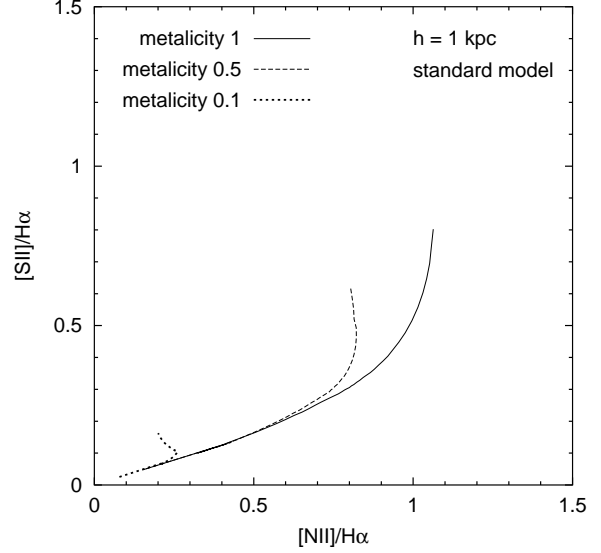


Figure 4.14: Absolute values of  $[SII]/H\alpha$  and  $[NII]/H\alpha$  for different metallicities

Figure 4.15 shows the influence of different scale heights which means physically the influence of different ionization parameters  $U_{r_0}$  at the starting radius  $r_0$  of the calculation (summarized in Table 4.1).  $U_{r_0}$  exhibits small variations for different input spectra and the same scale height ( $\sim 7\%$ ), but different scale heights give variations of up to a factor of four. Figure 4.16 exhibits the impact of the various input spectra with a scale height  $h$  of 1 kpc. Figure 4.15 and 4.16 show that lower  $[NII]/H\alpha$  and higher  $[SII]/H\alpha$  ratios are not reproducible with these parameters. As Figure 4.17 exhibits this region can better be modeled by a change in the effective temperature of the input spectrum. However not all data points can be covered, e.g.  $[NII]/H\alpha = 0.4$  and  $[SII]/H\alpha = 0.8$ . The models do not vary as much as the observations, only the CoStar model and the model with an effective temperature of 50,000 K have  $[NII]/H\alpha$  ratios higher than 1.2. All models regarding Figures 4.14 to 4.18 have a maximal  $[SII]/H\alpha$  ratio of 1.

A possible solution for the different slopes is the adoption of different depletion factors for the elements. The effect is displayed in Figure 4.18. If the nitrogen abundance is reduced by 50% and the sulphur abundance stays the same, then much higher  $[SII]/H\alpha$  ratios are achieved for smaller  $[NII]/H\alpha$  values. Line ratios of  $[NII]/H\alpha$  larger than one can be achieved by depleting sulphur and holding the abundance of nitrogen constant. The ratio  $[SII]/H\alpha$  gets smaller than 0.5 if the depletion of sulphur is 50%. With this strategy the region not reached within Figures 4.15 and 4.16 can be explained. Notably high values of  $[SII]/H\alpha$  ( $\sim 1$ ) with low  $[NII]/H\alpha$  ( $\sim 0.5$ ) are only reached by different depletion factors.

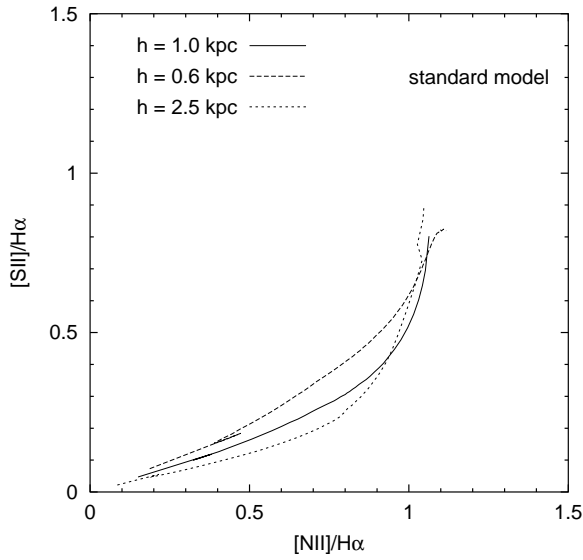


Figure 4.15: Absolute values of  $[SII]/H\alpha$  and  $[NII]/H\alpha$  for different scale heights

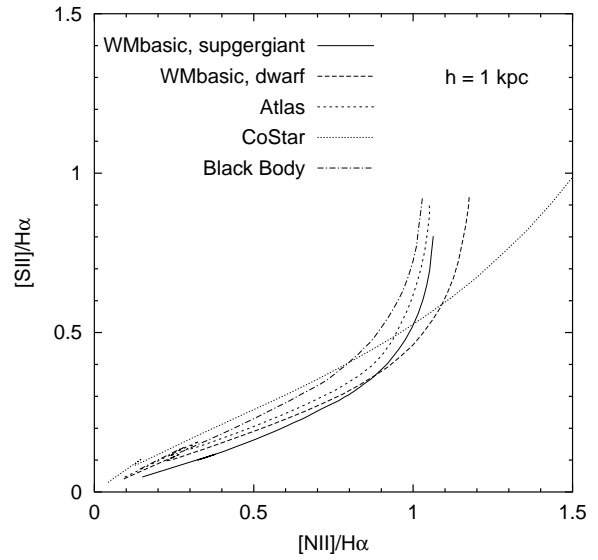


Figure 4.16: Absolute values of  $[SII]/H\alpha$  and  $[NII]/H\alpha$  for different input spectra

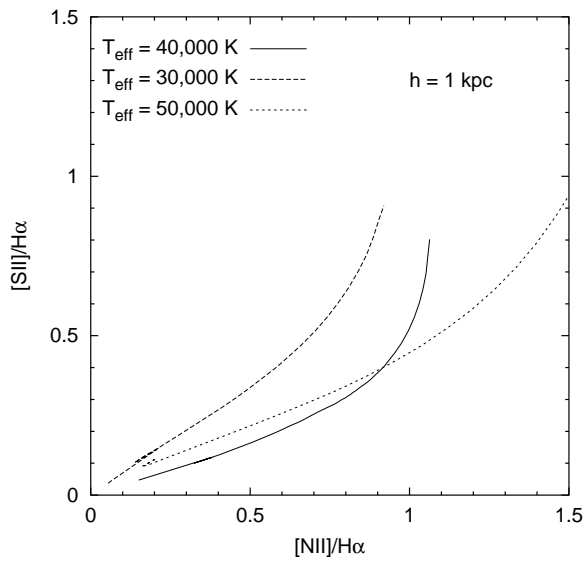


Figure 4.17: Absolute values of  $[SII]/H\alpha$  and  $[NII]/H\alpha$  for different effective temperatures  $T_{eff}$

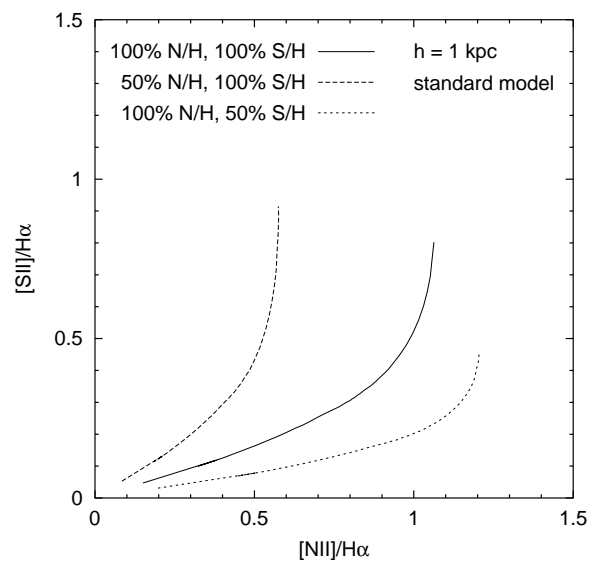


Figure 4.18: Absolute values of  $[SII]/H\alpha$  and  $[NII]/H\alpha$  for specific depletion factors of sulphur and nitrogen

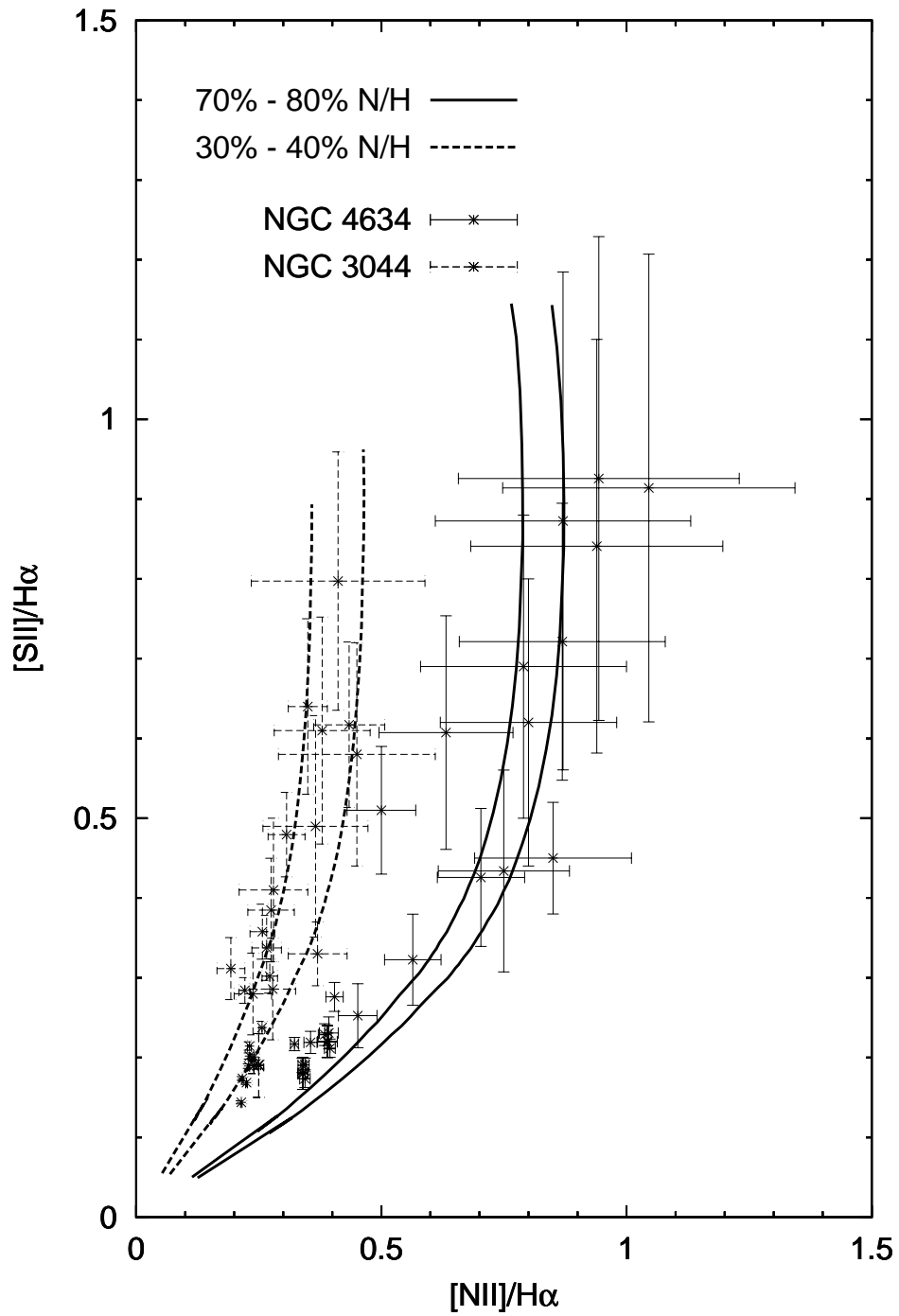


Figure 4.19: Modeling the data of NGC 3044 and NGC 4634



Table 4.1: Ionization parameters of the models

Model	scale height in kpc	ionization parameter $U_{r_0}$
WMbasic, supergiant	1	$9.14 \cdot 10^{-4}$
WMbasic, dwarf	1	$9.06 \cdot 10^{-4}$
Atlas	1	$8.88 \cdot 10^{-4}$
CoStar	1	$9.15 \cdot 10^{-4}$
Black Body	1	$9.35 \cdot 10^{-4}$
standard	0.6	$5.28 \cdot 10^{-4}$
standard	2.5	$2.04 \cdot 10^{-3}$
standard, $T_{\text{eff}} = 30,000$ K	1	$1.02 \cdot 10^{-3}$
standard, $T_{\text{eff}} = 50,000$ K	1	$8.46 \cdot 10^{-4}$

A possibility of having different depletion factors of nitrogen and sulphur is found in their different production mechanisms. Nitrogen is produced by hydrogen burning in main sequence stars and red giants and is ejected into the ambient ISM mostly by PN. Sulphur can only be produced by oxygen burning that happens in high mass stars and gets into the ISM mainly through SN II explosions (see e.g. Harwit 1998, Rubin et al. 1984). Assuming that both elements couple with the same efficiency onto grains the abundances of the elements should trace the evolution of a galaxy and its star formation history as they are produced in different stellar processes. Several investigations (e.g. Savage & Sembach 1996, Whittet 1984) come to the conclusion that nitrogen and sulphur have very similar depletion rates onto grains in the ISM in particular in cold clouds. This process seems therefore negligible in comparison to the different production environments. It is however remarkable that all observational points are 'covered' by Figures 4.15 to 4.18 in a way that there is no need to change the abundance of sulphur. The 'deficiency' of nitrogen and the resulting smaller values of  $[\text{NII}]/\text{H}\alpha$  could thus be a hint that one is observing in this cases young DIG-layers. The age of the DIG-layer could therefore be connected with e.g. a star-burst or at least a period of stronger star formation in the underlying disk giving rise to many SN II expelling rapidly sulphur in the ambient medium.

The application of this specific depletion method to the galaxies yields that NGC 3044 needs only 30 – 40 % of the nitrogen and the original sulphur abundance whereas the data of NGC 4634 are reproducible with 70 – 80 % of the nitrogen and the original sulphur abundance, this is shown in Figure 4.19. The stop condition for the models of NGC 4634 is that there is 30 % (!) neutral hydrogen at the edge, the influence of the Strömgren Sphere is therefore visible in the trend that with  $[\text{SII}]/\text{H}\alpha > 1$  the  $[\text{NII}]/\text{H}\alpha$  ratio is decreasing. This is the case as the ionization potential of nitrogen ( $\chi_{(\text{N}^+)} = 14.5$  eV) is higher than hydrogen ( $\chi_{(\text{H}^+)} = 13.6$  eV) and sulphur ( $\chi_{(\text{S}^+)} = 10.4$  eV) so that the amount of singly ionized nitrogen ions gets smaller more rapidly than the ions of  $\text{H}^+$  and  $\text{S}^+$ . Applying the argument that the  $[\text{NII}]/\text{H}\alpha$  ratio is a sign for the age of the DIG-layer one comes to the

conclusion that the DIG in NGC 4634 is older than in NGC 3044.

The  $[\text{SII}]/\text{H}\alpha$  and  $[\text{NII}]/\text{H}\alpha$  line ratios for the Perseus Arm of the Milky Way are not discussed, because the influence of the line of sight integration due to the position of the observer (see Figure 3.5) is difficult to estimate accurately. The models namely clearly show that the integration contributes indeed a significant portion to the values of the line ratios. The error due to a false interpretation of the data is likely big enough to alter the conclusions completely.

## 4.9 Column densities

Another test for the models are the observed column densities for the Reynolds-layer. Column densities can be obtained by interstellar absorption-line studies. Highly ionized gas is clearly traced by e.g. Si IV, C IV, N V, and O VI, (see e.g. Howk et al. 2003, Savage et al. 2001, Sembach & Savage 1992) and the neutral gas by e.g. H I, Ti II, Ca II, and Fe II (see e.g. Howk et al. 2003, Fitzpatrick & Spitzer Jr. 1997, Edgar & Savage 1989).

All these observations are made in our Galaxy, in this section only the models with a scale height of  $h = 1$  kpc and with the input spectra CoStar and WMasic with a supergiant spectrum are being used as the other models give no extra information and there are no observed column densities of the considered ions in other external edge-on galaxies.

The DIG can excellently be studied by the absorption-lines of S III and Al III. The ion  $\text{S}^{++}$  is 'created' at energies of 1.715 Ryd (ionization potential of  $\text{S}^+$ ) and 'destroyed' at 2.560 Ryd (ionization potential of  $\text{S}^{++}$ ),  $\text{Al}^{++}$  at 1.384 Ryd and 2.091 Ryd respectively. As the conditions of the DIG favor this energy range the observation of absorption-lines of these ions will give information about the phase under consideration.

Savage et al. (1990) determined out of a sample of 29 stars the data for the Al III column density. To obtain a larger sample for the Al III column density stars with  $|z| \geq 1$  kpc from Savage et al. (2001) were selected, resulting in altogether 14 additional stars. For the column density of S III only the data of Howk et al. (2003), Sembach et al. (2001), and Spitzer & Fitzpatrick (1993) (in total 3 stars) are available and therefore used here.

The column densities of Al III and S III, which vary with the column density of neutral hydrogen, were then fitted with a least square fit for this thesis. The results of the column densities which are compared to the models are the values for an H I column density of  $\log n_c(\text{HI}) \approx \log n_c(\text{total}) = 20.63$ . This specific HI column density represents the total hydrogen column density according to the phases of the ISM and their properties (midplane density, filling factor) as summarized in Table 1.1, with a fixed maximal  $|z|$  height of 2 kpc. It is further assumed that the  $\text{S}^{++}$  and  $\text{Al}^{++}$  ions exist mainly in the DIG and the other ISM phases give only negligible contributions.

Table 4.2 summarizes the column densities for the data and the models. The model results for Al III are smaller than the observations. The two samples of Al III column densities are consistent with each other. If the filling factor however is getting bigger with increasing  $|z|$  height as the observations suggests (Mitra et al. 2003, Haffner et al. 1999, Reynolds et al. 1999, Kulkarni & Heiles 1987) then the modeled Al III column density is only a lower

Table 4.2: Column densities in the DIG

Data/Model	$\log n_c$ at 2 kpc
Savage et al. (1990), Al III	$12.77 \pm 0.10$
Savage et al. (2001), Al III	$12.84 \pm 0.25$
standard model, Al III	12.36
CoStar, Al III	12.41
S III, data of: (a), (b), (c)	$14.71 \pm 0.50$
standard model, S III	15.19
CoStar, S III	15.18

<sup>a</sup> *Hawk, Sembach, Savage 2003, ApJ 586, 249*

<sup>b</sup> *Sembach, Hawk, Savage, Shull, Oegerle 2001, ApJ 561, 573*

<sup>c</sup> *Spitzer, Fitzpatrick 1993, ApJ 409, 299*

limit as with increasing filling factor the total column density attributed to the DIG will increase, too. Models with the WMbasic supergiant spectrum and e.g. a constant filling factor of 0.5 give a column density  $\log n_c(\text{Al III}) = 12.99$  (and  $\log n_c(\text{S III}) = 15.65$ ).

The total column density of aluminum for the DIG is  $\log n_c(\text{Al, total}) = 12.96$ . This means that the fraction of aluminum atoms that are doubly ionized must be at least 64 % in order to have a column density of  $\log n_c(\text{Al III}) = 12.77$ , however the dominant ionization stage of aluminum according to the models is Al II, with Al III having a part of  $\sim 30\%$  of the total. Thus without considering a changing filling factor one must consider other sources for the Al III column density such as a harder UV-photon flux, much harder indeed as the CoStar model produces also not enough Al III.

However due to the uncertainties and the varying filling factor the observed column density and the modeled one are consistent with the statement that a significant fraction of the Al III ions are created in the DIG.

Another problem is the abundance of aluminum which is dependent on the line of sight and the  $|z|$  height of the stars, this effect can influence the results up to a factor of 2.

Three measurements of individual stars of the S III column density give  $\log n_c(\text{S III}) = 14.71 \pm 0.5$ , the WMbasic supergiant model has 15.19 and CoStar 15.18 respectively. Although the modeled column densities are higher than the observed ones the models and the data are consistent with each other considering the errors.

The absorption line studies of Al III and S III in the Galaxy therefore show that the models are able to reproduce the observed column densities stating that these ions are predominantly produced in the DIG. However the data are not accurate enough to further constrain between the different models. Probably geometry effects and abundance changes along the line of sight are responsible for the wide spread of the data.

The models are reproducing moreover the observed column density of the electrons  $n_c(e^-)$ ,

taken at  $|z| = 2$  kpc, as determined by Savage et al. (1990). The column density match within the errors,  $\log n_{c,obs}(e^-) = 19.95 \pm 0.09$  and  $\log n_{c,mod}(e^-) = 20.04$  respectively. This basic quantity is thus also reproduced by the models.

# Chapter 5

## Results and discussion

### 5.1 Accuracy of the models

#### 5.1.1 Geometry

The CLOUDY models are one dimensional, all physical quantities are spatially only dependent on one linear coordinate. The structure of the DIG is though a three dimensional one which is observed in a two dimensional projection. This fact causes different problems, one is the line of sight integration. This effect is taken into account in dealing with the Perseus Arm data, the principle is displayed in Figure 3.5. In order to mimic the observational measurements one has to integrate over the whole intersection of the line of sight. One line of sight therefore has contributions from different volume emission coefficients from various  $|z|$  heights which depend on the local density and temperature. The line of sight through edge-on galaxies in contrast has perhaps significant contributions from different phases of the ISM. The position of the observer is therefore a relevant feature that has to be included into the discussion. This fact and the consequences will be treated in more detail in section 5.4.

#### 5.1.2 Radiative transfer

The radiative transfer used by the code has also to be examined. CLOUDY works with four different continua, the incident continuum that strikes the illuminated face of the cloud. The transmitted continuum which is the attenuated and diluted incident continuum exciting the cloud. The stellar radiation field is thereby reduced by geometrical dilution and absorption. The reflected continuum which is radiated in the direction of the ionizing source, and the diffuse continuum which is produced in the cloud. The continuum which is finally observed is therefore a superposition of the transmitted and diffuse continuum. The challenging problem is to determine the exact diffuse radiation field. CLOUDY uses the OWO (OutWard Only) approximation, which means that the diffuse emission is only considered for the outward direction. The estimation of the error being made by this approximation is an important task.

The incident continuum at the illuminated face of the cloud is the starting point for the calculation. The diffuse outward continuum which is calculated using OWO builds up gradually with depth into the cloud. However with increasing depth also the error gets bigger because only half of the diffuse continuum (the one going in the outward direction) is being considered.

Figure 5.1 shows the incident, transmitted, and diffuse outward continuum of the standard model. The ionization edges of H (911.6 Å), He<sup>0</sup> (504.5 Å), and He<sup>+</sup> (227.9 Å) are clearly visible in the transmitted continuum, the diffuse outward continuum shows a lot of structure in the form of emission lines. This continuum has an even higher photon flux than the transmitted one at the mentioned ionization edges. In order to get an upper limit of the error of the OWO approximation two models were run: one with the standard model and a second where the incident WMbasic supergiant spectrum was combined with the diffuse outward continuum of the first calculation. The part of the diffuse continuum which was neglected due to the OWO approximation in the first model is therefore taken into account in the second one. The effect of this additional continuum can be considered to be maximal as the intensity of it is maximal. The deviation between six different line ratios of the standard model and the combined one is shown in Figure 5.2. The considered ions are covering a large energy interval stressing the effect of the additional continuum at very different wavelength regimes. The deviations get larger with increasing depth, this is expected as the OWO neglects more and more flux with increasing depth. [OI]/H $\alpha$  and [SII]/H $\alpha$  are stronger in the standard model whereas [OIII]/H $\alpha$  and HeI/H $\alpha$  are stronger in the combined model. This is also clear because the spectrum of the combined model is harder hence higher ionization stages will be favored and vice versa. Both [NII]/H $\alpha$  and [OII]/H $\alpha$  do not show a unique trend, the corresponding ions have ionization potentials between the ones responsible for [OI] and [SII] on the one hand and [OIII] on the other. The discontinuity of some deviations at different radial positions is a rounding effect, if the line ratios get too small rounding starts to influence the calculation (the accuracy is three decimal places). As the absolute deviation is smaller than 5% for all line ratios considered, it is appropriate to state that the OWO approximation makes no major contribution in affecting the results of the model calculations. The diffuse continuum is thus weak enough to make only a second order effect.

### 5.1.3 Atomic database

All atomic data used in CLOUDY have uncertainties of the order of 10%, the data adopted by CLOUDY are discussed in Ferland (1997) and Ferland et al. (1984). In particular the photoionization cross-sections (using fits to the Opacity Project results by Verner et al. 1996) and radiative recombination rates (see references in Ferland et al. 1984) are relatively secure.

Whereas the dielectronic recombination coefficients of C, N, and O (Ali et al. 1991, Nussbaumer and Storey 1983) are well known, the dielectric recombination coefficients for 'low-lying autoionizing stages' (Ferland et al. 1998) of elements of the third row and higher of the periodic table of the elements are not known. This mainly affects the important

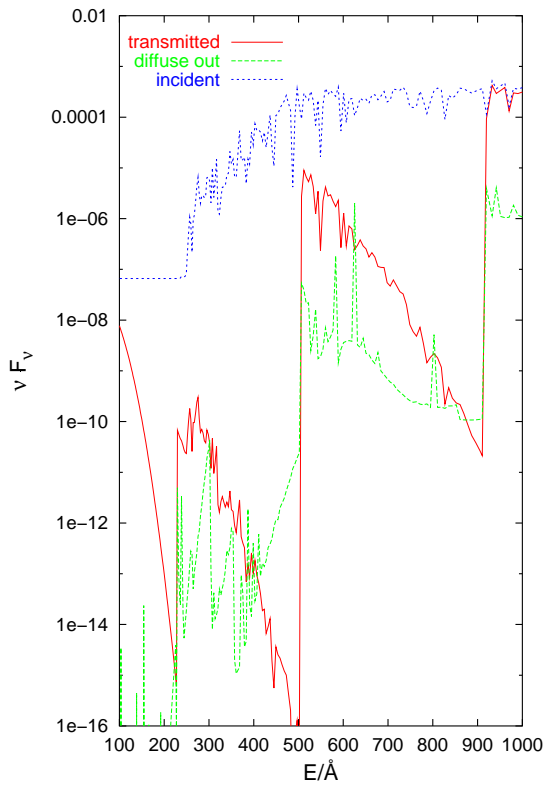


Figure 5.1: Transmitted, diffuse outward, and incident continuum

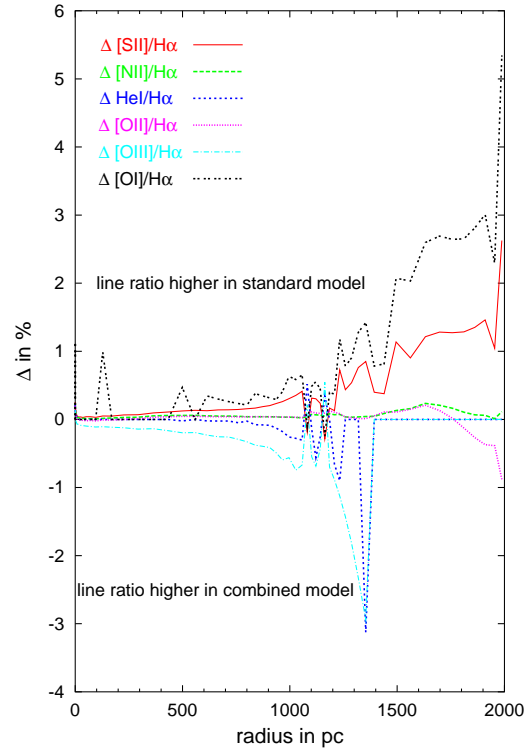


Figure 5.2: Deviation between the standard model and the one with an added diffuse outward continuum

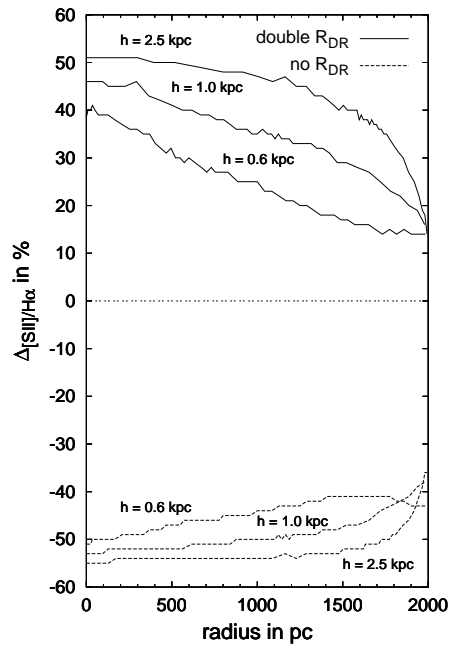


Figure 5.3: Effect of different dielectronic recombination coefficients on  $[SII]/H\alpha$

diagnostic line [SII]. CLOUDY uses the mean of the rate coefficients for C, N, and O in place for the unknown coefficient for sulphur. The two-step resonant process of dielectric recombination occurs if a radiationless capture is followed by a radiative transition (see section 3.3). As the temperature is about  $10^4$  K and the density is low, the probability that the doubly excited sulphur ion decays into a singly excited ion and therefore de-populating the doubly ionized sulphur atoms is very high. In order to see the quantitative effect of this process the results for the [SII]/H $\alpha$  ratio for models are presented in Figure 5.3 where the dielectronic rate coefficient  $R_{DR}$  is doubled and set to zero in regard to the standard model. All scale height regimes are examined in this way. The resonant nature of this process justifies this change, it could even be higher. If the rate coefficient is set to zero, the [SII]/H $\alpha$  line ratio is minimal, because dielectronic recombination rises the amount of singly ionized sulphur atoms and therefore the reservoir for collisional excitation and de-excitation via the forbidden emission line. The difference between the model with zero rate coefficient and the original one amounts to -55% in the [SII]/H $\alpha$  ratio. The deviation is larger for smaller  $|z|$  heights, because there is more doubly ionized sulphur at the beginning of the gas layer. The effect is also strongest for the model with a scale height of 2.5 kpc. This is also reasonable as this model has the highest ionization parameter  $U_{r_0}$  in regard to the scale height (see Table 4.1). If the rate coefficient is multiplied by a factor of two the differences are up to +50%, now the standard model has smaller [SII]/H $\alpha$  ratios. The model with a scale height of 2.5 kpc shows the biggest effect on the considered emission lines. The differences to the standard model are again decreasing with increasing  $|z|$  height. The forbidden [SII] emission line has altogether the largest uncertainties and the model calculations have to be handled with care in regard to it, especially for smaller  $|z|$  heights where the deviations are largest (see Figure 5.3).

## 5.2 Previous models

Previous photoionization models of the DIG (Mathis 2000, Bland-Hawthorn et al. 1997, Domgörgen & Mathis 1994, Sokolowski 1993a and 1993b) had special problems in modeling the considered line ratios. They examined the line ratios only in respect to upper and lower limits, so that the models are not spatially resolved although this is a crucial property in understanding the DIG. They also used a uniform density which is not observed according to the measured H $\alpha$  scale heights. The effect of density variations alters considerably the results of the CLOUDY models presented in this thesis. The other authors used less emission lines for comparing with the observations than this work. In order to make general predictions it is though very important to look at as much emission lines as possible. It is thereby preferable that the involved ions cover a broad range in ionization potentials.

The effect of a constant density is displayed in Figure 5.4 where three models are presented: the standard model and two models with a constant density. The first model has the same column density as the standard model resulting in a density of  $n = n_c = 0.0179 \text{ cm}^{-3} = \text{constant}$ . The second uses the midplane density of the standard model ( $n = n_0 = 0.2 \text{ cm}^{-3}$ ). All models have the same stop condition that the amount of neutral



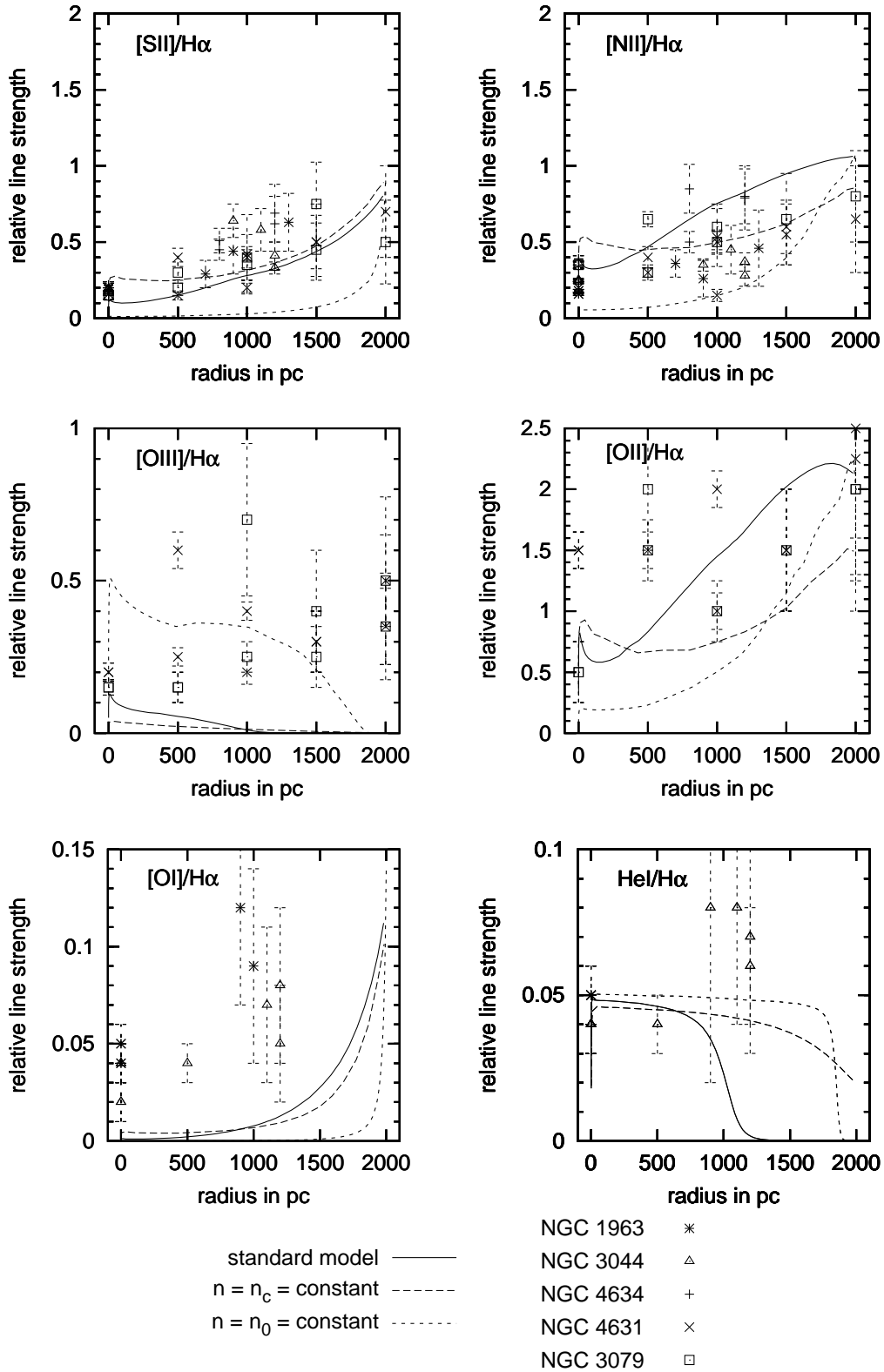


Figure 5.4: Comparison of the effect of different density functions; the standard one, two with constant densities: one with the same column density as the standard model ( $n_c$ ) and one with its midplane density ( $n_0$ )

hydrogen at a radius of 2 kpc should be 20%. The model with  $n = n_0$  reproduces the observed line ratios worst. It can only produce enough HeI emission but fails with the rest. The other model with  $n = n_c$  shows  $[\text{OIII}]/\text{H}\alpha$ ,  $[\text{OI}]/\text{H}\alpha$ , and  $[\text{NII}]/\text{H}\alpha$  which are too low compared with the standard model. The main cooling line  $[\text{OII}]$  is also underestimated, which is a serious problem as the ratio  $[\text{OII}]/\text{H}\alpha$  is a crucial property the models should reproduce, if photoionization is indeed the main source for powering the DIG. It is therefore apparent that the model with the exponential density law has the highest quality in reproducing the variation of the line ratios. Besides, only the used exponential density law produces the observed  $\text{H}\alpha$  scale height which stresses again the importance of the applied density run.

Sokolowski (1993a, 1993b) and Bland–Hawthorn et al. (1997) also used CLOUDY (version from 1991). Bland–Hawthorn et al. (1997) only quote part of the results of Sokolowski (1993a) so that in the following discussion only Sokolowski and his models are mentioned. The CLOUDY models of this thesis will be called 'thesis models' in the following.

Sokolowski showed with one example the variation of the line ratios in a region with a radius smaller than 0.1 kpc (not to be confused with a resolution) and drew all his conclusions from 'integrated' line ratios. The line of sight used in the Sokolowski models thus resembled the face-on view of a galaxy (for the according sight line see Figure 3.2) however he discussed the edge-on galaxy NGC 891 and the Milky Way which is therefore inconsistent. The total column density he considered is  $\leq 3.6 \times 10^{19} \text{ cm}^{-2}$ , whereas the thesis model has a total column density for the middle subgroup an order of magnitude higher ( $1.1 \times 10^{20} \text{ cm}^{-2}$ ). Sokolowski used a homogeneous density of  $n = 1 \text{ cm}^{-3}$  with different filling factors (between 0.05 and 0.1) and total column densities. These parameters result in spatial dimensions of  $\leq 0.1$  kpc whereas the thesis models with the exponential density profile reach the observed thickness of 2 kpc. It is questionable if the result for such a low spatial extension can be applied without problems to the dimension of 2 kpc. As the investigation of Sokolowski could only produce upper and lower bounds of the line ratios there are significant deviations from the observed ones. Sokolowski varied the ionization parameter freely, whereas the ionization parameter of the thesis models varies only in a small interval (about one order of magnitude, see Table 4.1) as the portion of neutral hydrogen at a thickness of 2 kpc is to be fixed by 20% (see section 4.2). Sokolowski varied  $U$  over three orders of magnitude (from  $10^{-2}$  to  $10^{-5}$ ) but he argued at the same time that observations show that  $U$  for the Milky Way lies in the range  $10^{-4} < U < 10^{-3}$ . This range is though fully complied with the thesis models (see Table 4.1). The models of Sokolowski include the whole Strömgren Sphere due to the integration of the sight line. It is however not clear why the ionization parameter should vary over more than three orders of magnitude concerning the global picture as promoted by his investigation. Sokolowski examined also in more detail the influence of other UV-photon sources and the depletion of refractory elements (interstellar opacity and metal depletion) and the consequential harder ionizing spectrum. However the dust/grain model used in CLOUDY is limited and therefore the variation of an uncertain parameter will only introduce more uncertainties. Moreover as section 4.6 shows the effect of the UV-flux of stellar remnant sources can be neglected.

Domgörgen & Mathis (1994) used their own code. They also considered line ratios that are the integral over the whole modeled cloud and therefore are difficult to link to spatially located observations. The models resembled thus more the face-on view, although they applied their models to the Milky Way where the ionizing sources of the DIG are not in the line of sight. These models are also only able to give upper and lower limits to the line ratios and are not able to explain their spatial variations. The authors changed the ionization parameter  $q$  related to the one used in equation (3.9) through

$$q = 10^{-50} \left( \frac{36\pi c^3}{\alpha_B^2} \right) \cdot U^3 \quad (5.1)$$

in a broad range. Through the combination of different models with different amounts of neutral hydrogen at the edge, different boundary effects are treated in an effective way. The total column density of neutral hydrogen is about  $7 \times 10^{17}$  H atoms  $\text{cm}^{-2}$  a factor of four smaller than the thesis models ( $n_c(\text{HI}) = 3 \times 10^{18} \text{ cm}^{-2}$  for  $h = 1$  kpc). Their models were able to produce values of  $[\text{NII}]/\text{H}\alpha$  of 0.34 and  $[\text{SII}]/\text{H}\alpha$  of 0.38 which is too low. The ratio  $[\text{OI}]/\text{H}\alpha$  is also too low for all  $|z|$  heights.  $[\text{OIII}]/\text{H}\alpha$  reached only values of maximal 0.2 though this was intended as (very few!) observations of  $[\text{OIII}]$  in the Milky Way at very low latitudes showed this value as an upper limit (Reynolds 1989 and 1985). The authors used observations of  $[\text{OIII}]/\text{H}\alpha$  and  $\text{HeI}/\text{H}\alpha$  although there are only two measured sight lines at very low Galactic latitudes published up to now. It is very dangerous to assume, as they do, that at high Galactic latitudes the line ratios have the same values. Edge-on galaxies clearly show that this is not the case. Moreover for lower  $|z|$  heights the definition of a pure DIG-spectrum becomes tedious, absorption features and the radiation of the other ISM phases, and above all HII regions are contaminating the spectrum.

Mathis (2000) is only an expansion of Domgörgen & Mathis (1994). Mathis combined in this paper various model runs, just by adding them up, with different  $q$  values and temperatures of the ionizing source in order to explain the line ratios. Two  $|z|$  heights above the plane of NGC 891 (1 kpc and 2 kpc), the Local Arm ( $b = 0^\circ$  and  $-35^\circ$ ), and the Perseus Arm (0.5 kpc and 1.2 kpc) of the Milky Way are treated in this way, but not consistently linked with the same parameters. Therefore only various combinations but no unique model is discussed in contrast to the thesis models. The Mathis models thus treat the DIG not as one phase, the spatial variation of the line ratios with  $|z|$  have no connection with each other which is a very extreme point of view. Mathis had to introduce an extra heating source in order to explain with this kind of mixing the observed line ratios at higher  $|z|$  heights successfully. Whereas the measurements are reproduced for the midplane without an extra heating source. However, Mathis did not present a conclusive and consistent model. Only individual parts of the DIG, which are though connected, can independently be explained by his models.

Figure 5.5 shows the predictions of the different models for the Perseus Arm of the Milky Way as this is the object where the other models were applied. Unfortunately up to now  $[\text{SII}]/\text{H}\alpha$  and  $[\text{NII}]/\text{H}\alpha$  are the only observed emission lines for the Perseus Arm. Models

with ionization parameter  $U = 10^{-3}$  and  $U = 10^{-4}$  for the Sokolowski model and  $q = 10^{-3} \Rightarrow U \sim 1.3 \cdot 10^{-4}$  for the Domgörgen & Mathis models are chosen. The standard model gives  $U_{r_0} = 9.14 \cdot 10^{-4}$ . Domgörgen & Mathis gave no results for higher  $U$  because they restricted the ratio  $[\text{OIII}]/\text{H}\alpha$  to values smaller than 0.2. The models of Mathis (2000) are not plotted because the different  $|z|$  heights are independent of each other in his models. The significance of such models for a constructive and coherent picture of the DIG therefore has to be questioned.

It is obvious that both the models of Sokolowski and Domgörgen & Mathis are giving boundaries for the line ratios (see Figure 5.5). However, the high values at  $|z| > 1.5$  kpc of  $[\text{SII}]/\text{H}\alpha$  as well as  $[\text{NII}]/\text{H}\alpha$  cannot be explained by these models. Only the standard model produces enough  $[\text{SII}]$  in comparison to  $\text{H}\alpha$ .

In Figure 5.6 the discussed photoionization models are shown with the values of the subgroup with  $h = 1$  kpc. In this diagram the importance of the knowledge of more emission line ratios than just  $[\text{SII}]/\text{H}\alpha$  and  $[\text{NII}]/\text{H}\alpha$  is clearly demonstrated. It is obvious that the Domgörgen & Mathis models predict nearly all line ratios far too low, whereas the Sokolowski models with the ionization parameter  $U$  between  $10^{-3}$  and  $10^{-4}$  act as effective envelopes for the line ratios.  $\text{HeI}/\text{H}\alpha$  is unfortunately not given by Sokolowski.

Figure 5.5 and Figure 5.6 demonstrate very clearly the **improved treatment of the line ratios with the thesis models** in contrast to the other photoionization models which could not produce the line ratio trends which are however essential for understanding the DIG.

## 5.3 Conclusions

### 5.3.1 Summary

This thesis discusses various aspects regarding the physical state of the DIG. The arguments of the power requirement for the DIG (see section 2.2) indicate that the UV-photon flux of young, hot stars is the most probable candidate for the dominating role in sustaining this phase of the ISM. The life times of O stars exceed the recombination time of hydrogen of the DIG, thus O stars can indeed form a continuous source of UV-photons. Observationally this was checked and the proof was given that the existence of the DIG is coupled to the star formation rate of the host galaxy (Rossa & Dettmar 2003a and 2000). The electrons in the DIG have velocities  $\langle v_e \rangle$ <sup>1</sup> due to the typical gas temperature (8000 K) of about  $6 \times 10^5 \text{ m s}^{-1}$  which means that they travel 2 kpc in  $\sim 3 \times 10^6$  a. The protons with a velocity  $\langle v_p \rangle$  of about  $1.5 \times 10^4 \text{ m s}^{-1}$  need approximately  $\sim 10^8$  a. However as the gas is quasi-neutral the electrons are bound to the protons so that for dynamical effects only the protons have to be considered. The velocities of supershells and superbubbles are in the range  $0.5 - 6 \times 10^4 \text{ m s}^{-1}$  (see e.g. Uyaniker & Kothes 2002, Dunne et al. 2001, Oey 1996) and therefore in the order of the thermal velocities of the protons. These shock processes

---

<sup>1</sup> $\langle v_e \rangle = \sqrt{\frac{3kT}{m_e}}$ ,  $\langle v_p \rangle = \sqrt{\frac{m_e}{m_p}}$

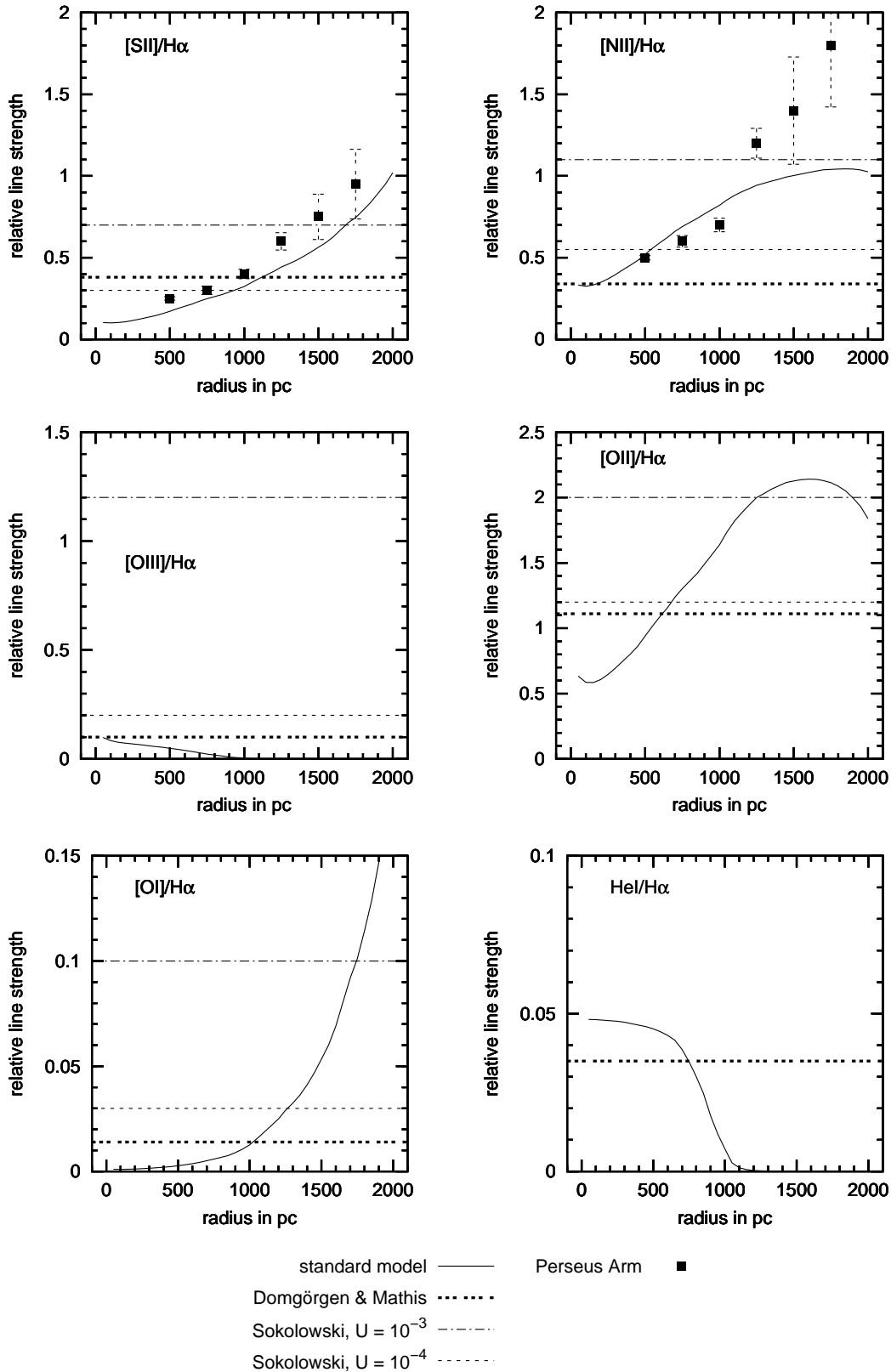


Figure 5.5: Comparison of the different photoionization models for the Perseus Arm

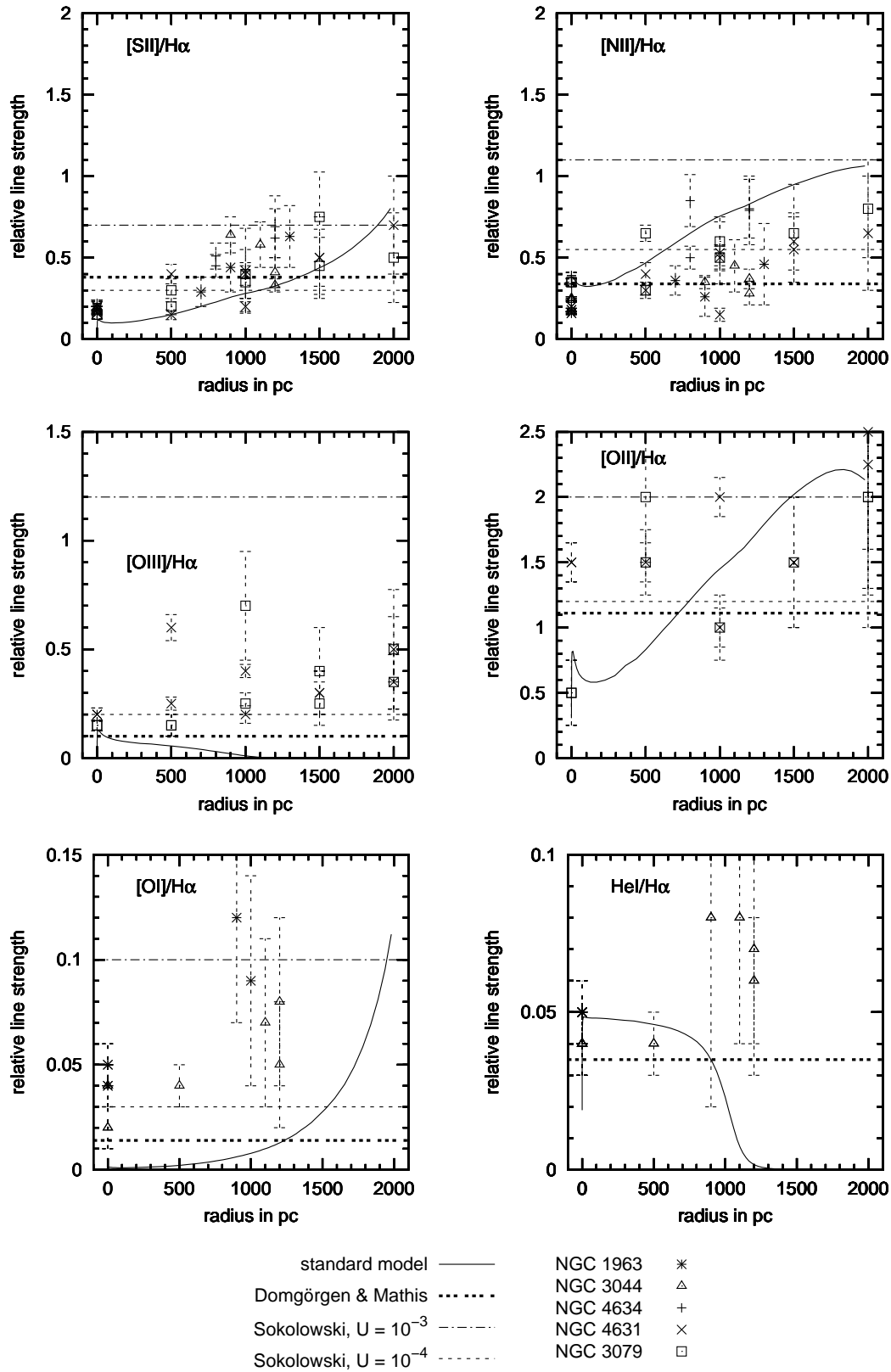


Figure 5.6: Comparison of the different photoionization models for the subgroup with  $h = 1$  kpc

should thus be of no dynamical significance on the global DIG scale. The finally resulting timescale of  $\sim 10^8$  a is considerably longer than the recombination time of hydrogen ( $\tau_{\text{rec}} \sim 10^6$  a) so that dynamical effects should play no crucial role. It is very probable that shock ionization is responsible for an important part of the emission line radiation in very outstanding filamentary regions but not for (the global) quiescent DIG. This view is supported by the photoionization models which are successfully modeling the quiescent DIG but have problems with turbulent one. Another possibility for special cases are very energetic superwinds (Heckman et al. 1990). The hot gas that breaks out of the according supershells can have velocities of  $\sim 10^5$   $\text{ms}^{-1}$ , so that it reaches 2 kpc after around  $10^7$  a. On the one hand this is one order of magnitude bigger than the  $\tau_{\text{rec}}$ , on the other hand it is not clear if the gas has cooled down in this time to form the DIG or if it is still too hot and not dense enough. Therefore all dynamical effects should not be severe enough to displace photoionization as the main driving source for the DIG.

Different CLOUDY photoionization models are tested by comparing predicted with observed optical line ratios in particular in respect to their behavior with increasing distance to the midplane (see chapter 4). The models examined in detail the radial variations of prominent line ratios in the first 2 kpc above the disk. It is evident that the CLOUDY photoionization models are successfully explaining the observed line ratios with regard to quiescent DIG. The thesis models need no general extra heating source. The elevation of  $[\text{OI}]/\text{H}\alpha$  and  $[\text{OIII}]/\text{H}\alpha$  can well be accounted for by geometric effects as will be shown in section 5.4. However the line ratios  $[\text{NII}]/\text{H}\alpha$  and  $[\text{SII}]/\text{H}\alpha$  especially  $[\text{NII}]/\text{H}\alpha$  larger than 1 need most probably a harder incident spectrum through a higher effective stellar temperature or the CoStar model (see Figure 4.16 and Figure 4.17). The standard model together with an additional heating source is successfully reproducing the Perseus Arm data. However it is shown in section 4.7 that the extra heating so far discussed is not able to enhance the line ratio sufficiently for the subgroup with  $h = 2.5$  kpc (turbulent DIG). Another important constraint is the main cooling line  $[\text{OII}]$  and its ratio to  $\text{H}\alpha$  which must not be overproduced through an extra heating source as is clearly demonstrated in Figure 4.11.

The ionization structure of the DIG is further investigated via the column densities of Al III, S III, and  $e^-$  (see section 4.9). The comparison between modeled and observed column densities results in the conclusion that the ions  $\text{Al}^{++}$  and  $\text{S}^{++}$  are indeed predominantly produced in the DIG. Moreover the models clarify that with the help of the specific line ratios  $[\text{SII}]/\text{H}\alpha$  and  $[\text{NII}]/\text{H}\alpha$  the evolution of a galaxy (star formation history) can be traced through the slope in the  $[\text{SII}]/\text{H}\alpha$ - $[\text{NII}]/\text{H}\alpha$ -diagram (see section 4.8). The individual gradients could be a hint for the age of the DIG-layer. It is further determined that the proposed dependency of this slope on the global metallicity is ruled out by the models. In relation to previous photoionization models (see section 5.2) an advanced treatment is presented by the thesis models. **For the first time the actual spatial dependency of the line ratios and therefore of the physical conditions is examined in a consistent way.** The incorporation of more optical spectral emission lines as the previous models takes note of the progress made in the observations. The additional information gained through the enlarged data base is very important to understand the general characteristic

features of the DIG.

In the following the results are presented in more detail, starting with the basic ionizing photon flux and the questions concerning the heating–cooling balance of the DIG. The CLOUDY models give new predictions for very probable important cooling lines. The observed and modeled emission lines and conclusions for the SED of the ionizing source are presented in section 5.3.4. The results from the column densities are then discussed in section 5.3.5. The CLOUDY photoionization models exhibit a high quality, but they can be improved as stated in section 5.3.6.

### 5.3.2 Ionizing photon flux

Reynolds (1990) determined a lower limit for the hydrogen ionizing photon flux of the Milky Way of

$$\Phi_{\text{DIG,obs}}(\text{MW}) \geq 5 \times 10^6 \text{ hydrogen ionizing photons cm}^{-2} \text{ s}^{-1} \quad (5.2)$$

This number was deduced from the observed intensity of the hydrogen recombination line  $\text{H}\alpha$  at high Galactic latitudes considering the cooling a primary function of the hydrogen recombination losses and collisional excitation cooling. In a first estimation, where only the hydrogen recombination losses are taken into account, the flux must be larger than the product of the effective hydrogen recombination coefficient  $\alpha_B$  ( $\sim 2.6 \times 10^{-13} \text{ cm}^{-2} \text{ s}^{-1}$ ) times the filling factor  $f$  and the integral over the square of the density

$$\Phi_{\text{DIG}} \geq f \times \alpha_B \times \int_z^\infty dz n_e^2(z) = f \times \alpha_B \times n_0^2 \times \int_z^\infty dz e^{-\frac{2z}{h}} \quad (5.3)$$

This equation gives for  $z = 0 \text{ pc}$ ,  $f = 0.2$ ,  $n_0 = 0.2 \text{ cm}^{-3}$  and  $h = 1 \text{ kpc}$  the result:  $\Phi_{\text{DIG}} \geq 3 \times 10^6 \text{ hydrogen ionizing photons cm}^{-2} \text{ s}^{-1}$ . This shows that the collisional excitation cooling 'consumes' almost half of the total ionizing photon flux.

The flux of the thesis models for the Perseus Arm is

$$\Phi_{\text{DIG,model}}(\text{MW}) \approx 5.8 \times 10^6 \text{ hydrogen ionizing photons cm}^{-2} \text{ s}^{-1} \quad (5.4)$$

which is therefore in excellent agreement with the observations. This result for the ionizing photon flux is valid for all models regardless of the input spectrum. The significance of the models with their stop condition is hereby stressed as they use the appropriate flux in order to get the real observed dimension of the DIG–layer.  $\Phi_{\text{DIG}}$  is determined by adding up all hydrogen ionizing photons neglecting their spectral energy distribution.

The estimation for NGC 891 gives after equation (5.3) an enhanced flux (factor 2.5) due to the larger scale height. Sokolowski (1993a) quoted that the flux in NGC 891 is approximately twice as much as the flux in the Milky Way. This is also predicted by the thesis models which show overall a factor of 2.2. The models are hence in excellent agreement with the observations and estimations for this basic quantity.



### 5.3.3 Heating–cooling balance

In all models the heating of the gas has various contributions. On average 90 % of the heating is due to hydrogen photoionization, 5 % comes from total helium photoionization, and 5 % from grain heating. The result of the power estimation, that photoionization is the main DIG heating source (see section 2.2), is thus accounted for by the models.

The main individual contributions to the cooling are coming from the collisionally excited lines [OII] and [SIII] with  $\sim 15\%$ , [NII] with  $\sim 8\%$ , [CII] with  $\sim 7\%$ , free–bound cooling with  $\sim 9\%$ , and free–free processes with  $\sim 5\%$ . More than half of the cooling is therefore due to only this handful lines and processes. The main optical cooling line is thus [OII], which really is a doublet as stated in section 2.3. The line ratio [OII]/ $H\alpha$  is very well reproduced by the models for all scale height groups. This is therefore very a strong evidence that photoionization by young, hot stars is indeed the dominant part in powering the DIG. The second important optical cooling line is [NII] which is well reproduced by the models, only for the subgroup with  $h = 2.5$  kpc the line ratio [NII]/ $H\alpha$  is systematically underestimated. Only the CoStar models with a harder input spectrum are able to produce [NII]/ $H\alpha$  ratios larger than one, assuming an effective temperature of the input spectrum of 40,000 K. This temperature is well constrained by the HeI/ $H\alpha$  ratio.

The models provide furthermore predictions for the up to now not observed fine–structure lines in the NIR and FIR<sup>2</sup>. These lines ([SIII] and [CII]) play an important role in the heating–cooling balance as they contribute  $\sim 20\%$  to the total cooling. The doublet of [SIII] (as stated in section 3.3) is a very good example having about the same part of the total cooling as the [OII] line, moreover the column density of SIII is already reproduced (see section 4.9). The [SIII] line ratios for all scale heights are displayed in Figure 5.7. All models lie in a very narrow band, [SIII] $\lambda 18.7\mu\text{m}$  ranges between 0.4 – 0.2 and [SIII] $\lambda 33.4\mu\text{m}$  between 0.7 – 0.3. The relative constancy is a direct consequence of the ionization structure (see Figure 4.1). The ratio  $S^{++}/S$  is larger than 0.5 (starting at 0.9) until  $\sim 1.9$  kpc with only a shallow slope. Therefore this line ratios can only poorly distinguish between different input spectra for the models, but they can be used as a test for the significance of photoionization in general. It is however very likely that the modeled line ratios are too high, as the column density of SIII is at the ‘high end’ of the errors. Nevertheless the importance of this [SIII] emission lines for the heating–cooling balance of the DIG is up to now not realized in the literature and thus **the thesis models reveal their significance for the first time**. The predicted fine–structure cooling line [CII] is contributing about 7 % to the total cooling. The ratio [CII]/ $H\alpha$  is displayed in Figure 5.8, the values are located between 0.2 and 0.9. The intensity of the [CII] line is thus at high distances from the midplane nearly as high as  $H\alpha$ . Heiles (1994) argued indeed that the [CII] emission line should be produced mainly in the DIG, followed by the CNM. This is clearly indicated by the models by predicting such high [CII]/ $H\alpha$  line ratios and the amount [CII] contributes to the total cooling. As carbon is produced by helium burning in red giants and high mass stars and ejected into the ISM through PN and SN, this element should thus only show a weak depletion due to the star formation history. However this element forms graphite

<sup>2</sup>NIR = Near IR, FIR = Far IR, the limit between these bands is at  $\sim 30 \mu\text{m}$

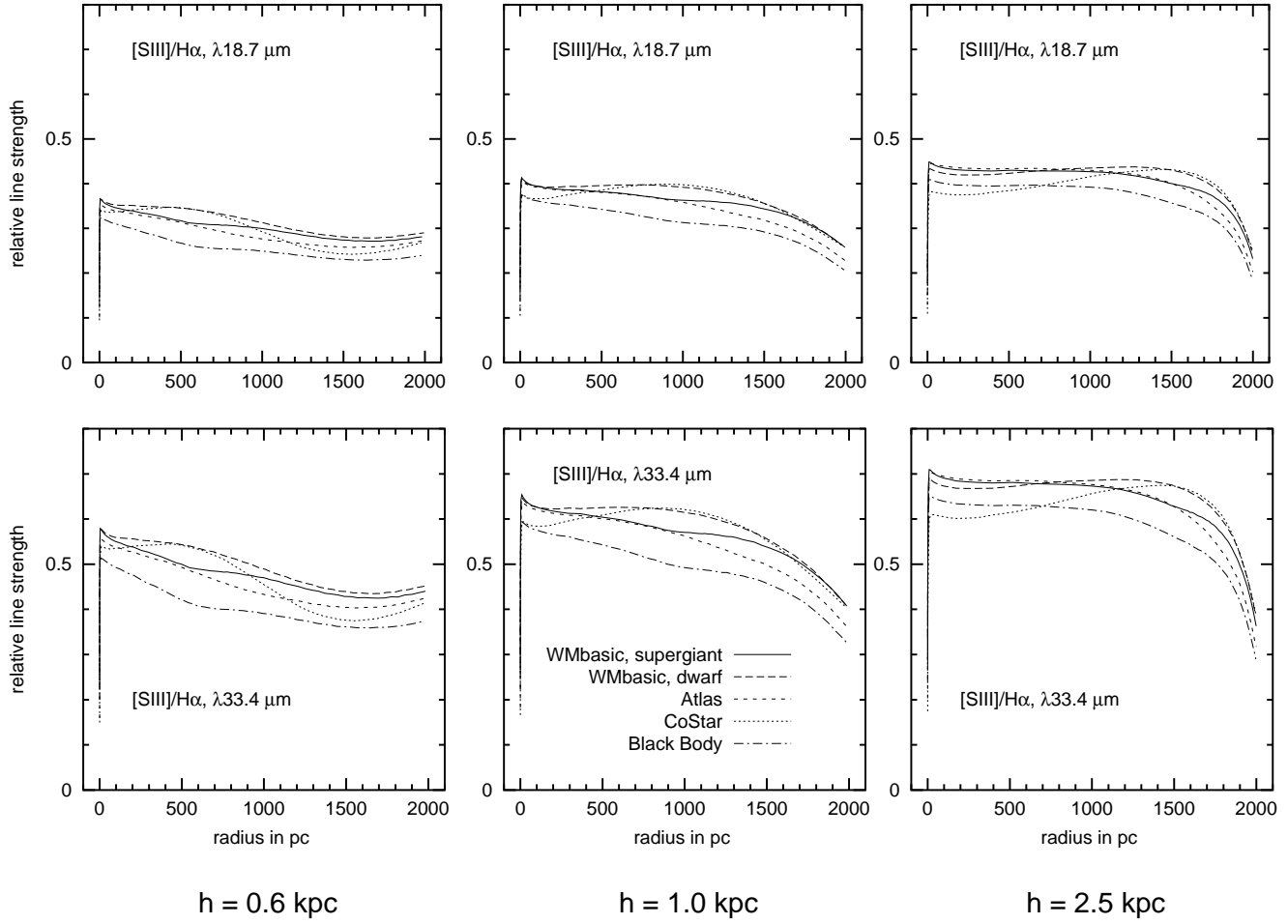


Figure 5.7: Line ratio of the IR fine-structure lines of  $[SIII]$  to  $H\alpha$  for all scale heights

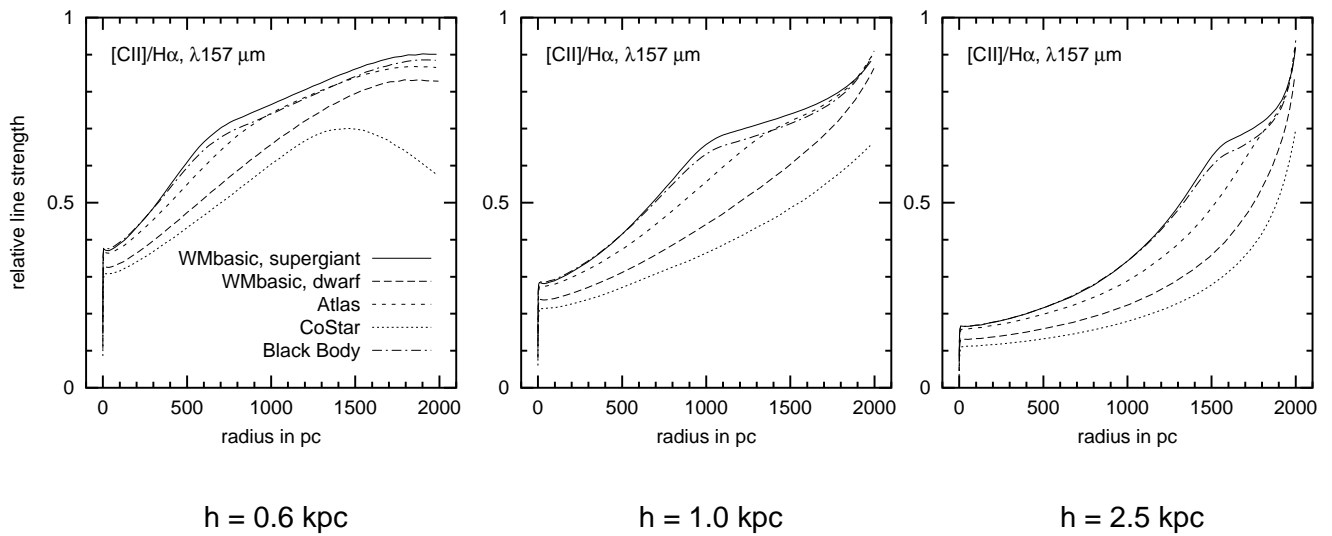


Figure 5.8: Line ratio of the IR fine-structure line  $[CII]$  to  $H\alpha$  for all scale heights

dust particles and different chemical bonds of it can be frozen on various dust particles (e.g. methane:  $\text{CH}_4$ , carbon monoxide:  $\text{CO}$ ). If carbon is more depleted from the gas than the models assume (factor 0.4, see also Savage & Sembach 1996) then the importance of grains will be enhanced and the ratio  $[\text{CII}]/\text{H}\alpha$  overestimated.

### 5.3.4 Emission lines and SED

The enhanced values of  $[\text{SII}]/\text{H}\alpha$  and  $[\text{NII}]/\text{H}\alpha$  as well as  $[\text{OII}]/\text{H}\alpha$  and  $\text{HeI}/\text{H}\alpha$  are satisfactorily reproducible with the models, considering different parameters for the subgroups (see section 4.4). The main cooling line  $[\text{OII}]$  is very well reproduced by the models for all subgroups showing that the dominant cooling mechanism is photoionization with a diluted radiation field. The spatial run of the first observed diagnostic line ratios  $[\text{SII}]/\text{H}\alpha$  and  $[\text{NII}]/\text{H}\alpha$  are also in good agreement with the models, only the subgroup with a scale height of  $h = 2.5$  kpc underestimates them. The  $\text{HeI}/\text{H}\alpha$  line ratio suggests an ionizing spectrum with an effective temperature of 40,000 K. All models show nearly the same behavior up to a  $|z|$  height of  $\sim 500$  pc. They have, however, some shortcomings concerning  $[\text{OI}]/\text{H}\alpha$  and  $[\text{OIII}]/\text{H}\alpha$ . They are not able to produce enough  $[\text{OI}]$  at lower  $|z|$  heights as suggested by the observations.  $[\text{OIII}]/\text{H}\alpha$  only has an opposite trend between the measurements and the models. All modeled  $[\text{OIII}]/\text{H}\alpha$  ratios decline with increasing distance, whereas the observations have a clear rising trend.

The spectral hardness of the input spectra can be traced with the emission lines originating from the ions with the highest ionization potential. The  $\text{O}^{++}$  ions fulfill this requirement ( $\chi_{(\text{O}^{++})} = 4.038$  Ryd) of the considered species. The maximal value of the ratio  $[\text{OIII}]/\text{H}\alpha$  is therefore a clear indicator of the spectral hardness of the ionizing DIG-spectrum. The line ratio  $[\text{OIII}]/\text{H}\alpha$  shows the strongest dependence on the scale height  $h$ . The ratio gets increased with higher  $h$ , this is a consequence of the higher ionization parameter (see Table 4.1) which directly follows from the restriction that 20% of the hydrogen must be neutral at a thickness of 2 kpc.

Not the whole energy range of the hydrogen ionizing photons seems to be important for the detailed behavior of the line ratios. There is e.g. a large variation in the modeled line ratios of  $[\text{OIII}]/\text{H}\alpha$  and  $\text{HeI}/\text{H}\alpha$  (after  $|z| \sim 500$  pc) between the different models. The doubly ionized oxygen ions have higher ionization potentials than the other ions considered and are thus much more sensitive to the hardness of the incident radiation field. The  $\text{HeI}$  line is the only recombination line considered and is therefore not as sensitive to temperature changes as the collisionally excited lines. In the case of  $\text{HeI}/\text{H}\alpha$  the predictions of the models with the supergiant spectrum of WMbasic and the Black Body match almost perfectly. This may be astonishing as the Black Body spectrum has up to one order of magnitude more flux between 228 Å (the ionization energy of singly ionized helium) and 260 Å, but more or less the same between 260 Å and 504 Å (ionization edge of neutral helium). However, the flux  $\Phi(506 - 228 \text{ \AA})$  of the two input spectra is nearly the same (see Table 3.2). Therefore the flux  $\Phi(260 - 228 \text{ \AA})$  has almost no effect in exciting  $\text{HeI}$ . This can also be understood through the general behavior of the photoionization cross section which shows a sharp decline with energy ( $\propto \nu^{-3}$ ). There are moreover differences between

these two models and the one with the dwarf spectrum of the WMbasic model, which has the same amount of flux in this energy range than the supergiant spectrum but shows HeI emission at larger radii than the other two.  $\Phi(506 - 228 \text{ \AA})$  is a factor of 1.36 larger than of the other two input spectra. The critical energy range of the input spectrum for all but doubly ionized oxygen hence seems to lie between the ionization potential of singly ionized sulphur ( $1.72 \text{ Ryd} \approx 530 \text{ \AA}$ ) and doubly ionized nitrogen ( $3.49 \text{ Ryd} \approx 260 \text{ \AA}$ ).

As the excitation of these lines is strongly dependent on the temperature (see equation 3.4) the increase in temperature with  $|z|$  thus enhances this lines (see Figure 4.2). The CoStar and WMbasic dwarf model show higher gas temperatures after 1.3 kpc than the other models and correspondingly [OIII] can more easily be excited at larger radii. Temperature is thus also a sensible measure for the UV-photon fluxes of the models. Moreover it is obvious that the gas temperature rises for all models with increasing distance from the midplane (see Figure 4.2) as seen in the observations (Reynolds et al. 1999). The CoStar model has the biggest change in temperature of  $\Delta T \approx 4000 \text{ K}$ , all other models have only  $\Delta T \approx 2000 \text{ K}$ . The maximal temperature reached by the CoStar model is 10,000 K, the other models lie between 8,300 K and 8,700 K. This can explain why the CoStar model has the highest values of [SII]/H $\alpha$  and [NII]/H $\alpha$  after  $\sim 1.5 \text{ kpc}$  and values of [NII]/H $\alpha$  larger than one. The increase in temperature is therefore also a characteristic feature of the models without an extra heating source. The implementation of such a heating rate (see section 4.7) enhances the temperature gradient even more, but the line ratios of the subgroup with  $h = 2.5 \text{ kpc}$  are still not explainable with these models.

### 5.3.5 Column densities

The column density gets bigger with increasing scale height due to the stop condition (20 % neutral hydrogen at  $|z| = 2 \text{ kpc}$ ). This leads to an enhanced photon flux and therefore higher ionization parameter  $U_{r_0}$  which varies over one order of magnitude for the standard model (see Table 4.1). This effect consequently reduces the amount of neutral and singly ionized species therefore diminishing the ratio [SII]/H $\alpha$ , [NII]/H $\alpha$ , [OII]/H $\alpha$ , [OI]/H $\alpha$ , and enhancing [OIII]/H $\alpha$ . The ratio HeI/H $\alpha$  is then reaching higher  $|z|$  heights (from 1 kpc with  $h = 0.6 \text{ kpc}$  to 1.7 kpc with  $h = 2.5 \text{ kpc}$  for the standard model). As shown in section 4.9 the observed column densities (normalized to  $|z| = 2 \text{ kpc}$ ) of S III match the model predictions, Al III is a factor of  $\sim 2.5$  less than observed. Given the possible strong variations in abundances the simulations are in accordance with the picture that the main part of the above mentioned ions are generated in the DIG. The column density of the electrons as given in Savage et al. (1990) of  $\log n_{c,obs}(e^-) = 19.95 \pm 0.09$  matches within the errors with the modeled one of  $\log n_{c,mod}(e^-) = 20.04$ , showing that the model is able to reproduce also this basic physical quantity.  $S^{++}$  is the main ionization stage in the DIG according to the models as is  $N^+$  and  $O^+$ . The very good reproduction of [NII]/H $\alpha$  and [OII]/H $\alpha$  is a further indicator for the quality of the models considering the ionization structure. As  $S^+$  is not the main ionization stage the collisional excitation of this ion is very effective, elevating [SII]/H $\alpha$ . This is also due to the rising temperature as indicated by the models (see Figure 4.2).

### 5.3.6 Quality of the models

The models are one dimensional while the observations are two dimensional projections of a three dimensional structure, geometric effects are thus likely to be significant.

The models have also to deal with some inaccuracies as is discussed in section 5.1. The treatment of the radiative transfer with OWO makes only a minor contribution, smaller than 5%. Uncertainties in the atomic data could result in variations of up to 10% of the line ratios. The error due to the dielectronic rate coefficient for the [SII]/H $\alpha$  ratio is difficult to fix, it could be as large as 50%.

Grain heating has been taken into account within this CLOUDY version and the models, although the treatment of grains is limited. They have only one size and the opacities for merely a handful of grain species are incorporated. As it is proven that most grain properties depend strongly on their size, the behavior for grain photoelectric heating have to be handled with care (van Hoof et al. 2001). However, improvements (such as varying grain sizes) in the next version of the code will be made and help to make the statement of the models even more reliable.

The approximations, inaccuracies, and limited incorporated dust model discussed are thus not severe enough to alter the statements of the models in general.

## 5.4 Outlook

### 5.4.1 General statements

The CLOUDY photoionization models can successfully explain most of the observed line ratios in the DIG if it is quiescent i.e. has a smooth varying brightness (subgroup with  $h = 0.6$  kpc). Only [OI]/H $\alpha$  and [OIII]/H $\alpha$  show less agreement with the thesis models. As filaments and shells begin to play an important role in combination with larger scale heights, the simulations show increasing deviations from the observations. Except for [OIII]/H $\alpha$  the modeled line ratios have the same trend as the measurements. This is a strong hint that perhaps an additional heating source is needed in order to elevate and invert the trend of this line ratio. Section 4.7 shows clearly that both the type and the power of the extra heating source so far incorporated is insufficient for the subgroup with  $h = 2.5$  kpc.

Geometry effects are very likely to be of significance. On the one hand [OI] could be produced mainly in neutral envelopes of denser, cooler clouds embedded in the DIG. The probability that a line of sight intersects with some clouds is very high as in the case of edge-on galaxies the line of sight integrates over the whole disk at a certain vertical distance  $|z|$  to the midplane. The cloud has then the effect of elevating the [OI]/H $\alpha$  ratio. On the other hand [OIII] could be produced in a much hotter medium, with a smaller density and higher temperature. The oxygen is then mostly doubly ionized and the [OIII] line can more easily be excited. It is therefore important to distinguish if certain emission lines originate in different phases of the ISM. Is the observed spectrum a pure DIG-spectrum? What can photoionization models consequently achieve in modeling the spectrum and where are

their shortcomings? As (nearly) all emission line ratios seem to rise toward higher  $|z|$  including emissions from neutral, singly, and doubly ionized atoms it is evident that the simple geometry assumed for HII regions has to be handled with care. There seems to be no clear distinction in specific ionization spheres as in classical HII regions, neutral and ionized atoms coexist on the line of sight, most probable sustained by geometric effects. From the observational point of view one has to take into account the influence of projection effects. If a galaxy is not perfectly seen edge-on the observed spectrum is partly 'contaminated' with emission from the plane of the galaxy. In order to estimate this effect one can look at a 'standard' spiral galaxy with a radius of 15 kpc, if the inclination is  $85^\circ$  the (stellar, gas, and dust) disk will be tilted so that at the center the disk will stick out 1.31 kpc in both  $|z|$  directions, at a radius of 7.5 kpc this will be diminished to 0.65 kpc (see Figure 5.9). This values are only lower boundaries as for the calculation the thickness of the disk component is assumed to be negligible. The exact positions of the slits in relation to the galaxy radius is therefore important to estimate this projection effect. However the additional light from the disk will mainly enhance the observed stellar continuum which is not taken into account. The influence on the emission line ratio will be smaller as there is also absorption in the disk, the effect will be that the DIG-spectrum transforms into a classical HII region spectrum if the contribution of the disk is dominating. This is also observed and is the explanation for certain individual features and the situation that sometimes the minimum of the line ratios are not at the midplane (position  $|z| = 0$  kpc), e.g. NGC 3044 (Tüllmann & Dettmar 2000a) or NGC 4631 (Otte et al. 2001). Prominent dust lanes in the midplane of the galaxies have the effect of severely alter the observed spectrum at low vertical heights. All considered external edge-on galaxies have inclinations larger than  $80^\circ$ , but as Table 5.1 shows it is difficult to determine the exact inclination angle as the references differ by more than  $5^\circ$ . The exact impact of the inclination effect on the line ratios is therefore difficult to estimate and until now not considered. It should be mentioned that Table 5.1 gives not a complete list of references.

Furthermore the slit position is important for another reason, if a prominent filament is chosen to lie in the slit, other processes are likely to dominate than photoionization if the filament is not just a projection effect. The observations of Tüllmann et al (2000b) of NGC 5775 are a very nice example where the slit was positioned on a strong filament. Another example is the effect of strong HII regions on the observed line ratios, biasing toward more classical HII region spectra near the midplane of galaxies. Individual features can be very prominent in the spectrum, e.g. the very strong spike in  $[\text{OII}]/\text{H}\alpha$  (value: 10) at  $z = -600$  pc in NGC 4631 (Otte et al. 2001), or the spikes around  $z = \pm 0$  pc in  $[\text{OII}]/\text{H}\alpha$  and  $[\text{OIII}]/\text{H}\alpha$  (Otte et al. 2001) in NGC 891, reaching 4 and 1.1 respectively. These features are either intrinsic, caused by an observational bias or due to the difficulty in applying a correct de-reddening procedure as the authors stated. In order to minimize effects caused by projection, slit position, or individual feature of a galaxy various galaxies at different slit positions are compared in this thesis. As it is shown the measurements populate a relatively confined region in the considered diagrams and thus give a fair guess of typical line ratios of the DIG. It would however be better to enlarge the sample of used galaxies to minimize these effects further.

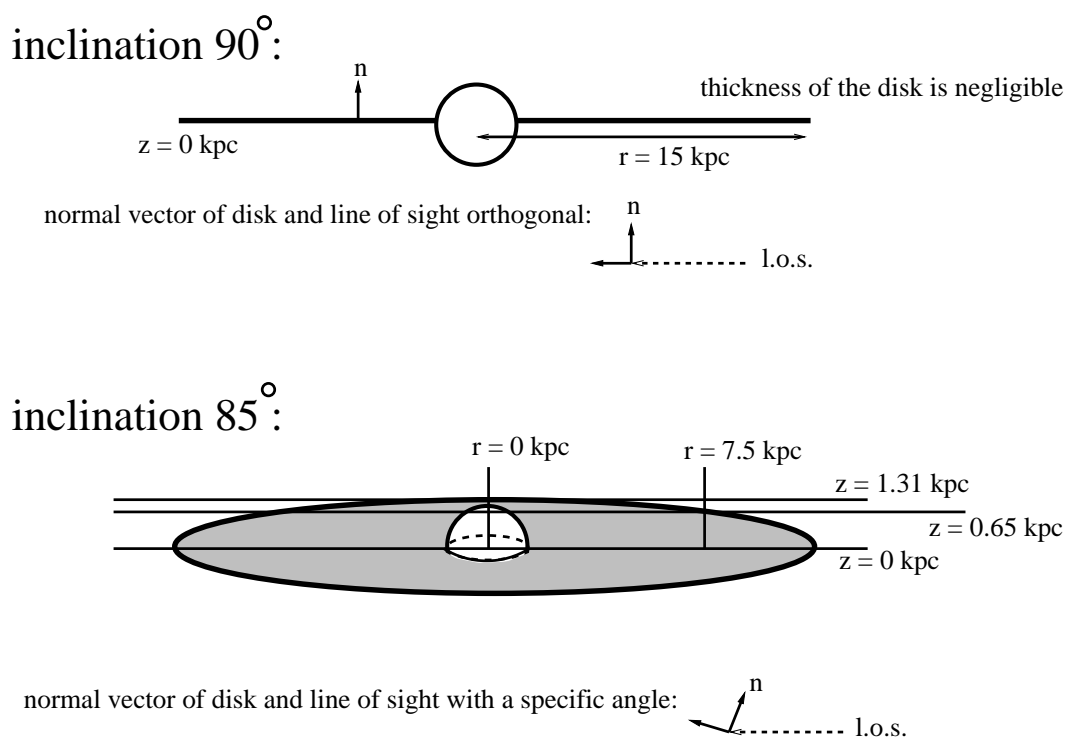


Figure 5.9: *Effect of the inclination of a galaxy in contaminating the DIG spectra, l.o.s. = line of sight*

Table 5.1: *Inclination angles of the edge-on galaxies*

galaxy	inclination in degrees	references
NGC 4302	88	Tüllmann & Dettmar (2000a)
NGC 4302	90	Alton et al. (2000)
NGC 4302	90	LEDA
UGC 10288	87	Alton et al. (2000)
UGC 10288	90	LEDA
NGC 1963	85	Tüllmann & Dettmar (2000a)
NGC 1963	90	LEDA
NGC 3044	84	Tüllmann & Dettmar (2000a)
NGC 3044	90	LEDA
NGC 4634	83	Tüllmann & Dettmar (2000a)
NGC 4634	80.6	LEDA
NGC 4631	85	LEDA
NGC 3079	82.5	LEDA
NGC 891	88	Rossa & Dettmar (2003b)
NGC 891	89.8	Alton et al. (2000)
NGC 891	88	LEDA

*LEDA = Lyons Extragalactic Data Archive*

Table 5.2: *Parameters of the different phases for the combined model*

Phase	filling factor	density in $\text{cm}^{-3}$	scale height in kpc	diameter in pc
DIG	0.2	0.2	1	—
HIM like	0.7	0.01	5	—
cloud	0.1	0.45	—	200



### 5.4.2 Considering the multiphase nature of the ISM

In order to address the geometry effects Figure 5.10 shows the first calculations which take into account different phases simulating more realistic sight lines through the halo. There is no interaction between the different phases. The specific sight line is a superposition of the standard DIG model with a HIM like phase together with one cloud (as part of the WNM) chosen to begin at a height of  $|z| = 200$  pc and to end at  $|z| = 400$  pc sitting 'on top' of the usual DIG density run (see Table 5.2). As input spectrum for the cloud part the WMbasic supergiant spectrum with an effective temperature of 40,000 K is chosen. The thin phase is illuminated by a combination of two spectra as introduced in section 4.6: on the one hand the standard WMbasic supergiant spectrum and on the other hand a Black Body spectrum with an effective temperature of 70,000 K to take the effects of stellar remnants into account. The hydrogen ionizing photon flux of this second spectrum is set to be 1/100 of that of the WMbasic supergiant spectrum.

Figure 5.10 shows the result regarding the emission line ratios, for a better comparison the standard DIG model is also plotted. The effect of the cloud is clearly seen in line ratios with neutral and singly ionized elements, most clearly in  $[\text{OI}]/\text{H}\alpha$ . The line ratios  $[\text{SII}]/\text{H}\alpha$ ,  $[\text{NII}]/\text{H}\alpha$ ,  $[\text{OII}]/\text{H}\alpha$ , and  $[\text{OI}]/\text{H}\alpha$  increase between  $|z| = 200$  pc and 600 pc, whereas  $[\text{OIII}]/\text{H}\alpha$  and  $\text{HeI}/\text{H}\alpha$  show a corresponding depression. This makes clear that the small scale variations in the data can indeed be explained by clouds that are in the line of sight in addition to other reasons such as a variation in the ionizing photon flux or changes of the local abundances.

The different phases dominate in general the run of the line ratios at special  $|z|$  heights, the cloud for  $|z| < 0.6$  kpc, the hot phase for  $|z| > 1.1$  kpc and the standard DIG phase in between. The thin HIM like phase has furthermore its strongest influence on the  $[\text{OIII}]/\text{H}\alpha$  and  $\text{HeI}/\text{H}\alpha$  ratio which show in this case a rise after  $|z| = 1$  kpc. This is the first model where the trend in the observed  $[\text{OIII}]/\text{H}\alpha$  line ratio is the same as in the models although the observed value is still not reached. **In this case all trends of observed and modeled line ratios are for the first time (concerning photoionization models) the same in one consistent model !**

The ratio  $[\text{OIII}]/\text{H}\alpha$  has still some shortcomings so that it is very likely that an additional heating source is needed to elevate the modeled line ratio enough to match with the observations. The gas temperature of the models seems thus still too low for higher  $|z|$  heights. It will be favorable to incorporate also other types of extra heating rates that are e.g. dependent on density.

This model shows definitely that geometry effects together with the multiphase nature of the ISM can result in more realistic models that describe better the observed emission line ratios. The next step should be to implement a certain distribution of cloud sizes into the models, account for more and different lines of sight and therefore get to a more realistic description of the observations.

**In essence the presented CLOUDY-models reveal that photoionization is indeed the main source in sustaining the DIG** (see mainly sections 5.3 and 5.4.2). The observed line ratios can be understood by properly applying photoionization models.

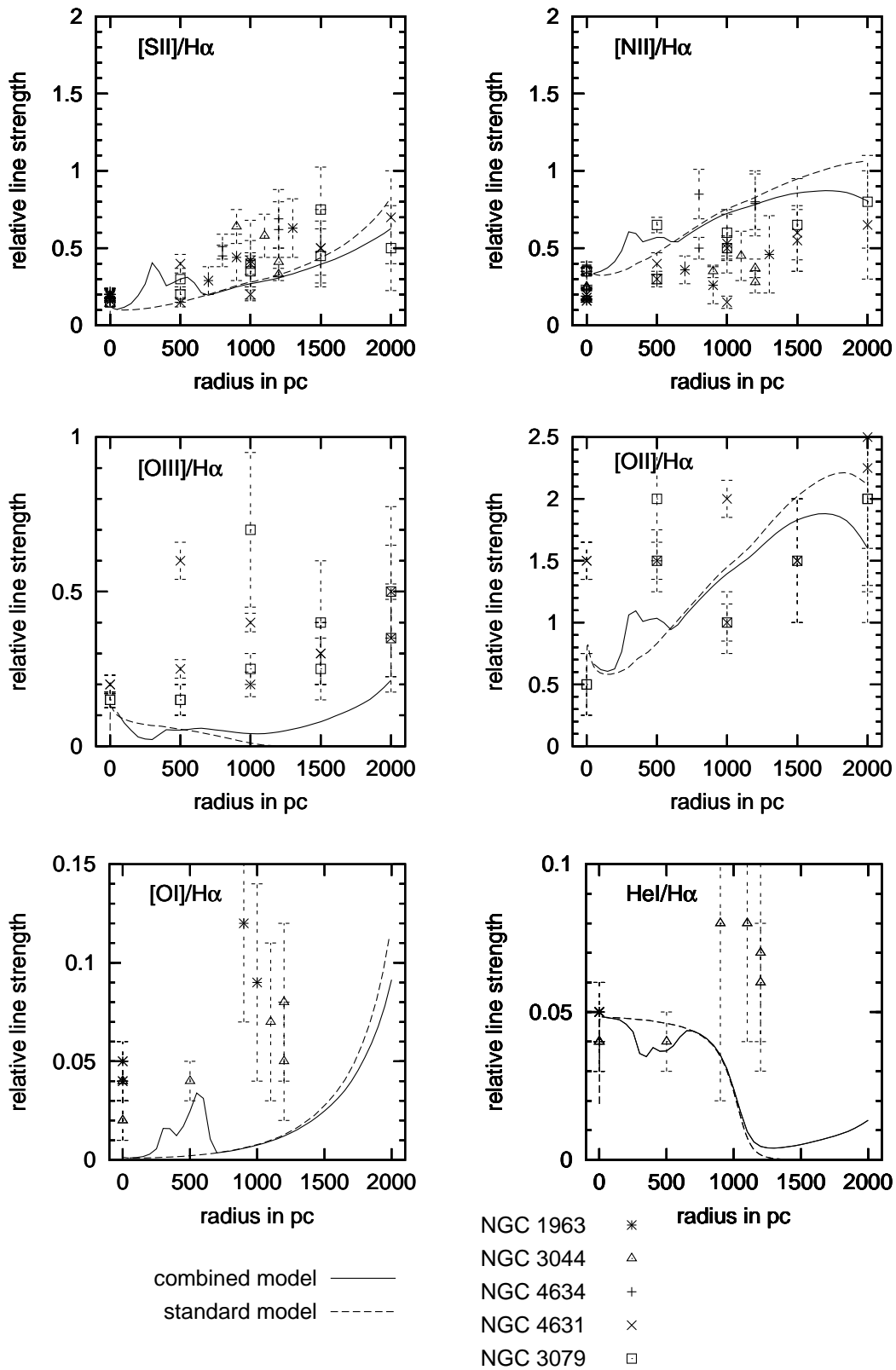


Figure 5.10: Model with a composition of three different phases in comparison to the standard model

# Bibliography

Abbott, D.C. 1982, ApJ 263, 723

Ali, B., Blum, R.D., Bumgardner, T.E., Cranmer, S.R., Ferland, G.J., Haefner, R.I., Tiede, G.P. 1991, PASP 103, 1182

Alton, P.B., Rand, R.J., Xilouris, E.M., Bevan, S., Ferguson, A.M., Davies, J.I., Bianchi, S. 2000, A&AS 145, 83

Avillez, de M.A. 2000, MNRAS 315, 479

Baldwin, J., Ferland, G.J., Martin, P.G., Corbin, M., Cota, S., Peterson, B.M., Slettebak, A. 1991, ApJ 374, 580

Beck, R. Shoutenkov, V., Ehle, M., Harnett, J.I., Haynes, R.F., Shukurov, A., Sokoloff, D.D., Thierbach, M. 2002, A&A 391, 83

Birk, G.T., Lesch, H., Neukirch, T. 1998, MNRAS 296, 165

Bland–Hawthorn, J., Freeman, K.C., Quinn, P.J. 1997, ApJ 490, 143

Bregman, J.N., Harrington, J.P. 1986, ApJ 309, 833

Collins, J.A., Rand, R.J. 2001, ApJ 551, 57

Cowie, L.L., Songaila, A. 1986, ARA&A 24, 499

Cox, D.P., Smith, B.W. 1974, ApJ 189, L105

Dahlem, M. 1997, PASP 109, 1298

Dahlem, M., Lazendic, J.S., Haynes, R.F., Ehle, M., Lisenfeld, U. 2001, A&A 374, 42

Dettmar, R.–J. 1992, Fund. Cosmic Phys. 15, 143

Dishoeck, van E.F., Black, J.N. 1986, ApJS 62, 109

Domgörgen, H., Mathis, J.S. 1994, ApJ 428, 647

Donahue, M., Aldering, G., Stocke, J.T. 1995, ApJ 450, L45

- Dopita, M.A., Sutherland, R.S. 2003, "Astrophysics of the Diffuse Universe" (Springer Verlag: A&A Library)
- Dove, J.B., Shull, J.M., Ferrara, A. 2000, ApJ 531, 846
- Draine, B.T. 1978, ApJS 36, 595
- Dunne, B.C., Points, S.D., Chu, Y.-H. 2001, ApJS 136, 119
- Edgar, R.J., Savage, B.D. 1989, ApJ 340, 762
- Ferguson, A.M.N., Wyse, R.F.G., Gallagher, J.S. III, Hunter, D.A. 1996, AJ 111, 2265
- Ferland, G.J. 2000, ASP Conference Proc., Vol. 216
- Ferland, G.J. 1997, HAZY, "A Brief Introduction to CLOUDY 90"
- Ferland, G.J., Savin, D.W. 2001, editors of "Spectroscopic Challenges of Photoionized Plasmas", ASP Conf. Series, Vol. 247
- Ferland, G.J., Korista, K.T., Verner, D.A., Ferguson, J.W., Kingdon J.B., Verner, E.M. 1998, PASP 110, 761
- Ferland, G.J., Mushotzky, R.F. 1984, ApJ 286, 42
- Field, G.B., Goldsmith, H.J., Habing, H.J. 1969, ApJ 155, L149
- Fitzpatrick, E.L., Spitzer, L. Jr. 1997, ApJ 475, 623
- Ginzburg, V.L., Syrovatskii, S.I. 1964, "The Origin of Cosmic Rays" (Pergamon Press Ltd.)
- Haffner, L.M., Reynolds, R.J., Madsen, G.J., Tufte, S.L., Jaehning, K.P., Percival, J.P., Hausen, N.R. 2001, AAS, 199, # 58.01
- Haffner, L.M., Reynolds, R.J., Tufte, S.L. 1999, ApJ 523, 223
- Harwit, M. 1998, "Astrophysical Concepts" (Springer Verlag: A&A Library)
- Heckman, T.M., Armus, L., Miley, G.K. 1990, ApJS 74, 833
- Heiles, C. 2001, in "Tetons 4: Galactic Structure, Stars, and the Interstellar Medium", ASP Conf. Series Vol. 231, eds. C.E. Woodward, M.D. Bica, J.M. Shull
- Heiles, C. 1994, ApJ 436, 720
- Heiles, C. 1984, ApJS 55, 585

- Hoof, van P.A.M., Weingartner, J.C., Martin, P.G., Volk, K., Ferland, G.J. 2001, in “Spectroscopic Challenges of Photoionized Plasmas”, ASP Conf. Series, Vol. 247, 363, ed. G. Ferland & D.W. Savin
- Hoopes C.G., Walterbos R.A.M., Greenawalt B.E. 1996, AJ 112, 1429
- Howk, J.C., Sembach, K.R., Savage, B.D. 2003, ApJ 586, 249
- Ikeuchi, S. 1988, Fund. Cosmic Phys. 12, 255
- Koo, B.-C., Heiles, C., Reach, W.T. 1992, ApJ 390, 108
- Kulkarni, S., Heiles, C. 1987, in “Interstellar Processes”, ed. D.J. Hollenbach & H.A. Thronson, Jr. (Dordrecht: Reidel), 87
- Kurucz, R.L. 1991, in Proc. “Workshop on Precision Photometry: Astrophysics of the Galaxy”, ed. A.C. Davis Philip, A.R. Upgren, & K.A. James (Davis, Schenectady), 27
- Landau, L.D., Lifschitz, E.M. 1974, “Hydrodynamik” (Akademie-Verlag, Berlin)
- Lehnert, M.D., Heckman T.M. 1995, ApJS 97, 89
- Lerche, I., Schlickeiser, R. 2001, A&A 366, 1008
- Lockman, F.J. 1984, ApJ 283, 90
- Lockman, F.J., Gehman, C.S. 1991, ApJ 382, 182
- Lockman, F.J., Hobbs, L.M., Shull, J.M. 1986, ApJ 301, 380
- Mac Low, M.-M., Ferrara, A. 1999, ApJ 513, 142
- Mac Low, M.-M., McCray, R. 1988, ApJ 324, 776
- Martin, C., Kern, B. 2001, ApJ 555, 258
- Mathis, J.S. 2000, ApJ 544, 347
- Miller, W.W. III, Cox, D.P. 1993, ApJ 417, 579
- Minter, A.H., Spangler, S.R. 1997, ApJ 485, 182
- Mitra, D., Mueller, P., Berkhuijsen, E. 2003, talk at the conference “How does the Galaxy work?”, 23.–27. June 2003, Granada, Spain
- Norman, C.A., Ikeuchi, S. 1989, ApJ 345, 372
- McCammon, D., Burrows, D.N., Sanders, W.T., Kraushaar, W.L. 1983, ApJ 269, 107
- McKee, C.F., Ostriker, J.P. 1977, ApJ 218, 148

- Nussbaumer, H., Storey, P.J. 1983, *A&A* 126, 75
- Oey, M.S. 1996, *ApJ* 467, 666
- Osterbrock, D.E. 1989, “Astrophysics of Gaseous Nebulae and Active Galactic Nuclei” (Mill Valley: University Press)
- Otte, B., Reynolds, R.J., Gallagher III J.S., Ferguson, A.M.N. 2001, *ApJ* 560, 207
- Panagia, N., Terzian, Y. 1984, *ApJ* 287, 315
- Pauldrach, A.W.A. 2002, private communication
- Pauldrach, A.W.A., Hoffmann, T.L., Lennon, M. 2001, *A&A* 375, 161
- Rand, R.J. 1998, *ApJ* 501, 137
- Reynolds, R.J. 1993, in *AIP Conf. Proc.* 278, *Back to the Galaxy*, ed. S.S. Holt & F. Verter (New York: AIP), 156
- Reynolds, R.J. 1992, *ApJ* 392, L35
- Reynolds, R.J. 1990, *ApJ* 349, L17
- Reynolds, R.J. 1989, *ApJ* 345, 811
- Reynolds, R.J. 1985, *ApJ* 294, 256
- Reynolds, R.J., Haffner, L.M., Tufte S.L. 1999, *ApJ* 525, L21
- Reynolds, R.J., Cox, D.P. 1992, *ApJ* 400, L33
- Rossa, J., Dettmar, R.-J. 2003a, *A&A* 406, 493
- Rossa, J., Dettmar, R.-J. 2003b, *A&A* 406, 505
- Rossa, J. 2001, “A Quantitative Investigation of Diffuse Ionized Gas and Dust in Halos of Edge-on Spiral Galaxies”, PhD thesis, Ruhr-Universität Bochum
- Rossa, J., Dettmar, R.-J. 2000, *A&A* 359, 433
- Rubin, V.C., Ford, W. K. Jr., Whitmore, B.C. 1984, *ApJ* 281, L21
- Sakamoto, T., Chiba, M., Beers, T.C. 2003, *A&A* 397, 899
- Savage, B.D., Meade, M.R., Sembach, K.R. 2001, *ApJS* 136, 631
- Savage, B.D., Sembach, K.R. 1996, *ARA&A* 34, 279
- Savage, B.D., Edgar, R.J., Diplas, A. 1990, *ApJ* 361, 107

- Schaerer, D., de Koter, A., Schmutz, W., Maeder, A. 1996, *A&A* 310, 837
- Sembach, K.R., Howk, J.C., Savage, B.D., Shull, J.M., Oegerle, W.R. 2001, *ApJ* 561, 573
- Sembach, K.R., Savage, B.D. 1992, *ApJS* 83, 147
- Shapiro, P.R., Field, G.B. 1976, *ApJ* 205, 762
- Slavin, J.D., McKee, C.F., Hollenbach, D.J. 2000, *ApJ* 541, 218
- Sokolowski, J. 1993a, preprint
- Sokolowski, J. 1993b, *ASP Conf. Series*, Vol. 35
- Spitzer, L. Jr. 1978, "Physical Processes in the Interstellar Medium" (New York: Wiley)
- Spitzer, L. Jr., Fitzpatrick, E.L. 1993, *ApJ* 409, 299
- Tayler, R.J. 1993, "Galaxies: structure and evolution" (Cambridge University Press)
- Tenorio-Tagle, G., Munoz-Tunon, C. 1998, *MNRAS* 293, 299
- Tielens, A.G.G.M., Hollenbach, D. 1985, *ApJ* 291, 722
- Tüllmann, R., Rosa, M.R., Elwert, T., Bomans, D.J., Ferguson, A.M.N., Dettmar, R.-J. 2003, accepted by *A&A*
- Tüllmann, R., Dettmar, R.-J. 2000a, *A&A* 362, 119
- Tüllmann, R., Dettmar, R.-J., Soida, M., Urbanik, M., Rossa, J. 2000b, *A&A* 364, L36
- Uyaniker, B., Kothes, R. 2002, *ApJ* 574, 805
- Verner, D.A., Ferland, G.J., Korista, K.T., Yakovlev, D.G. 1996, *ApJ* 465, 487
- Vogel, S., Weymann, R., Rauch, M., Hamilton, T. 1995, *ApJ* 441, 162
- Weingartner, J.C., Draine, B.T. 2001, *ApJS* 134, 263
- Welsh, B.Y., Sfeir, D.M., Sirk, M.M., Lallement, R. 1999, *A&A* 352, 308
- Whittet, D.C.B. 1984, *MNRAS* 210, 479





# List of Figures

1.1	<i>ISM constituents</i> . . . . .	2
1.2	<i>Star–gas–cycle, the abbreviations are explained in the text (subsection 1.1.2)</i> . . . . .	2
1.3	<i>Sketch of the edge–on view of a spiral galaxy, the halo is indicated</i> . . . . .	3
1.4	<i>Picture of the ISM as proposed by the MO model (McKee &amp; Ostriker 1977), the right sketch shows the impact of a SN generated shock wave coming from the upper right corner on the small ISM clouds: they evaporate and only their cores survive</i> . . . . .	7
1.5	<i>Picture of ISM as proposed by the chimney model (Norman &amp; Ikeuchi 1989)</i> . . . . .	8
2.1	<i>Morphology of the DIG in the Milky Way, WHAM collaboration (e.g. Haffner et al. 2001, Haffner et al. 1999)</i> . . . . .	11
2.2	<i>Morphology of the DIG in the central part of NGC 55, Tüllmann et al. (2003)</i> . . . . .	12
2.3	<i>Morphology of the DIG in NGC 3044, Rossa (2001)</i> . . . . .	12
2.4	<i>Data of scale height group <math>h = 0.6</math> kpc</i> . . . . .	17
2.5	<i>Data of scale height group <math>h = 1</math> kpc</i> . . . . .	19
2.6	<i>Data of scale height group <math>h = 2.5</math> kpc</i> . . . . .	21
3.1	<i>Number of Fortran lines making CLOUDY from 1978 until 1996 (HAZY, Ferland 1997)</i> . . . . .	24
3.2	<i>Geometry of the CLOUDY models</i> . . . . .	26
3.3	<i>Energy level diagram for dielectronic recombination in a low density plasma</i> . . . . .	28
3.4	<i>Sight lines according to observations of edge–on galaxies</i> . . . . .	31
3.5	<i>Observations of the Perseus Arm</i> . . . . .	31
3.6	<i>Input spectra for the photoionization models regarding the UV photon flux</i> . . . . .	33
4.1	<i>Ionization fraction for different ions, scale height <math>h = 2.5</math> kpc and different input spectra</i> . . . . .	38
4.2	<i>Gas temperatures for the subgroup with <math>h = 2.5</math> kpc and different input spectra</i> . . . . .	39
4.3	<i>Effect of different stellar atmosphere models on the subgroup with <math>h = 0.6</math> kpc, effective stellar temperature 40,000 K</i> . . . . .	41
4.4	<i>Effect of different stellar atmosphere models on the subgroup with <math>h = 1</math> kpc, effective stellar temperature 40,000 K</i> . . . . .	43

4.5	<i>Effect of different stellar atmosphere models on the model for the Perseus Arm, effective stellar temperature 40,000 K</i>	44
4.6	<i>Effect of different stellar atmosphere models on the subgroup with <math>h = 2.5</math> kpc, effective stellar temperature 40,000 K</i>	46
4.7	<i>Effect of different stellar effective temperatures, on the subgroup with <math>h = 1</math> kpc, stellar model: WMbasic, supergiant</i>	47
4.8	<i>Difference between the models with WMbasic supergiant, <math>T_{eff} = 50,000</math> K and CoStar with <math>T_{eff} = 40,000</math> K</i>	48
4.9	<i>Effect of a second ionizing source with a harder input spectrum and two different fluxes</i>	50
4.10	<i>Effect of a constant volume extra heating rate for the model predictions for the Perseus Arm</i>	52
4.11	<i>Effect of a constant volume extra heating rate for the model predictions for the subgroup with <math>h = 2.5</math> kpc</i>	53
4.12	<i>Data of the galaxies NGC 3044 and NGC 4634</i>	55
4.13	<i>Slope in the [SII]–[NII] diagram for models with different metallicities</i>	56
4.14	<i>Absolute values of [SII]/H<math>\alpha</math> and [NII]/H<math>\alpha</math> for different metallicities</i>	56
4.15	<i>Absolute values of [SII]/H<math>\alpha</math> and [NII]/H<math>\alpha</math> for different scale heights</i>	57
4.16	<i>Absolute values of [SII]/H<math>\alpha</math> and [NII]/H<math>\alpha</math> for different input spectra</i>	57
4.17	<i>Absolute values of [SII]/H<math>\alpha</math> and [NII]/H<math>\alpha</math> for different effective temperatures <math>T_{eff}</math></i>	57
4.18	<i>Absolute values of [SII]/H<math>\alpha</math> and [NII]/H<math>\alpha</math> for specific depletion factors of sulphur and nitrogen</i>	57
4.19	<i>Modeling the data of NGC 3044 and NGC 4634</i>	58
5.1	<i>Transmitted, diffuse outward, and incident continuum</i>	65
5.2	<i>Deviation between the standard model and the one with an added diffuse outward continuum</i>	65
5.3	<i>Effect of different dielectronic recombination coefficients on [SII]/H<math>\alpha</math></i>	65
5.4	<i>Comparison of the effect of different density functions; the standard one, two with constant densities: one with the same column density as the standard model (<math>n_c</math>) and one with its midplane density (<math>n_0</math>)</i>	67
5.5	<i>Comparison of the different photoionization models for the Perseus Arm</i>	71
5.6	<i>Comparison of the different photoionization models for the subgroup with <math>h = 1</math> kpc</i>	72
5.7	<i>Line ratio of the IR fine–structure lines of [SIII] to H<math>\alpha</math> for all scale heights</i>	76
5.8	<i>Line ratio of the IR fine–structure line [CII] to H<math>\alpha</math> for all scale heights</i>	76
5.9	<i>Effect of the inclination of a galaxy in contaminating the DIG spectra, l.o.s. = line of sight</i>	81
5.10	<i>Model with a composition of three different phases in comparison to the standard model</i>	84

# List of Tables

1.1	<i>ISM phases and their properties</i>	4
1.2	<i>ISM models emphasizing the disk–halo interaction</i>	8
2.1	<i>Optical emission line ratios of the model HII regions and observed in the DIG</i>	15
2.2	<i>Overview of galaxies and used observed emission lines</i>	22
3.1	<i>Transition probabilities of observed emission lines</i>	27
3.2	<i>SED of the different input spectra normalized to the Black Body spectrum</i>	33
4.1	<i>Ionization parameters of the models</i>	59
4.2	<i>Column densities in the DIG</i>	61
5.1	<i>Inclination angles of the edge–on galaxies</i>	82
5.2	<i>Parameters of the different phases for the combined model</i>	82



# Acknowledgments

**I want to thank everybody who supported me in creating this thesis!**

Many thanks to Prof. Dr. R.-J. Dettmar who provided me with this exciting topic, who was available for many discussions, and let me visit several conferences and Madison.

Cordial thanks to HD Dr. Susanne Hüttemeister for acting as the second thesis referee.

Many thanks to Ron Reynolds who made my stay in Madison an exciting experience and a success.

Special thanks to Adi Pauldrach for new insights regarding stellar atmosphere models.

Many thanks to all members of the AIRUB.

This work would not have been possible without the constant encouragement and support from Giuseppe, Elli, Inken, and Arno. I thank my parents for giving me the opportunity to fulfill my studies.

# Technical Acknowledgments

The text has been created with  $\text{T}_{\text{E}}\text{X}$  (version 3.14159, Web2C 7.3.1) and  $\text{L}^{\text{A}}\text{T}_{\text{E}}\text{X}$  2 $\epsilon$  respectively with the editor Xemacs (version 21.1, patch 10). The printed postscript version has been formatted using dvips (version 5.86, Radical Eye Software).

Figures have been created with Xfig (version 3.2.3a) or Gnuplot (version 3.7.1).

I acknowledge the use of the code CLOUDY, version 94.00, written by Gary Ferland. The ASCII files of CLOUDY have been further processed with Perl (version perl 5.005, patch 03).

The research has made use of NASA's Astrophysics Data System Abstract Service (ADS) and the NASA/IPAC Extragalactic Database (NED), which is operated by the Jet Propulsion Laboratory, California Institute of Technology, under contract with the National Aeronautics and Space Administration.

I acknowledge the use of the Lyon–Meudon extragalactic database (LEDA), through the CISM of the Lyon Claude–Bernard University (<http://leda.univ-lyon1.fr>), the astro-ph preprint archive and the SIMBAD database, operated at CDS, Strasbourg, France.

# Curriculum vitae

Name: Torsten August Wilhelm Heinrich Elwert  
Date of birth: 15.04.1975  
Native town: Koblenz

Education: since 2000 PhD student for astronomy  
at the Ruhr-Universität Bochum,  
topic: “*Photoionization Models of the Diffuse Ionized Gas in Galactic Halos*”  
09.06.2000 “Diplom”, topic: “*Beitrag der Charm-Quarks zum Protonspin in der Heavy-Quark-Mass-Expansion*”,  
theoretical particle physics  
13.09.1996 “Vordiplom”  
WS 1996/97 study abroad at the Universität Zürich (Switzerland)  
1994–2000 study of physics at the Ruhr-Universität Bochum  
1985–1994 Gymnasium: Hilda-Gymnasium Koblenz,  
Examination: Abitur  
1981– 1985 Elementary school: Neukarthause Koblenz

Practical courses: 03.10.1999– Summer school “Matter under extreme conditions –  
16.10.1999 quantum statistics in Plasma and Astrophysics” of the  
WE Heraeus-Stiftung in Rostock (Germany)  
14.07.1997– Summer student at the PSI (Paul Scherrer Institut) in  
28.09.1997 Villigen (Switzerland),  
Project work at the HESSI-satellite  
01.08.1995– Working student at the nuclear power station of RWE  
31.08.1995 Energie AG in Mülheim-Kärlich (Germany)

Employment: since 02.10.2000 scientific assistant, Ruhr-Universität Bochum  
15.10.1999– student assistant, Ruhr-Universität Bochum  
29.02.2000

Versicherung gemäß §7 Abs. 2 Nr. 5 PromO 1987

Hiermit versichere ich, daß ich meine Dissertation selbständig angefertigt und verfaßt und keine anderen als die angegebenen Hilfsmittel und Hilfen benutzt habe. Meine Dissertation habe ich in dieser oder ähnlicher Form noch bei keiner anderen Fakultät der Ruhr-Universität Bochum oder bei einer anderen Hochschule eingereicht.

Bochum, den 30.09.2003

Torsten Elwert